Microcellular low-density nanocomposite foams nucleated by carbon-based nanofillers – processing, properties and foaming behaviour

Von der Fakultät für Ingenieurwissenschaften
der Universität Bayreuth
zur Erlangung der Würde eines
Doktor-Ingenieurs (Dr.-Ing.)
genehmigte Dissertation

von

M.Sc. Chimezie Okolieocha

aus

Lagos, Nigeria

Erstgutachter: *Prof. Dr.-Ing. Volker Altstädt*
Zweitgutachter: *Prof. Dr. Hans-Werner Schmidt*
Mündliche Prüfung: *29.01.2019*

Lehrstuhl für Polymere Werkstoffe
Universität Bayreuth
2019

Acknowledgements

As the saying goes, a journey is easier when you travel together. Therefore, I am grateful to the many people that have accompanied me on my journey and encouraged me along the way. I would also like to reflect on specific people that have supported and helped me during this time.

To begin, I would like to express my profound gratitude to Prof. Dr.-Ing. Volker Altstädt for all the support and motivation he has given me through thought-provoking discussions during my research work at his chair “Lehrstuhl für Polymere Werkstoffe”, University of Bayreuth. I am also deeply grateful for his laudable contributions and personal guidance which have provided a good basis for this research work.

Special thanks to Prof. Dr. Rolf Mülhaupt, Freiburg Material Research Centre, Institute of Macromolecular Chemistry, University of Freiburg for providing functional graphene (TRGO) materials which served as one of the fillers for my research work. His inspiration and enthusiasm for research made a strong impression on me. I wish to also acknowledge Fabian Beckert, Folke Tölle, Daniel Hofmann, Stefanie Schopp, Karen-Alesa Wartig and Bela Olah from Freiburg Material Research Centre, University of Freiburg, for their experimental support in the synthesis and characterization of TRGO.

I would like to thank Dr.-Ing. Martin Kothmann for his constructive criticism and proofreading of the manuscript, as well as for his valuable insights and steadfast encouragement. It was a pleasure to work with him as a member of his nanocomposite group at the Department of Polymer Engineering, University of Bayreuth.

I must place on record my gratitude to Anne Lang, Ute Kuhn, Sebastian Gröschel, Melanie Förtsch, Dr. Marina Krekova, Lena Geiling, Markus Schirmer and Andreas Mainz, for the technical and experimental support they provided in accomplishing this study. A big thank you to Bianca Fischer for her intellectual discussions and support.

To the foam group team members past and present (Dr.-Ing Thomas Köppl, Dr.-Ing Kalaivani Selveraj, Tobias Standau, Daniel Raps, Sabrina Kerling), I say thank you for the team work. Many thanks to Sebastian Elwein, Philipp Beutler, Stefanie Hartlieb, Nicole Sommer and Judith Schöbel for the assistance in experiment and characterization measurements.

I also wish to acknowledge other members of the Department of Polymer Engineering, University of Bayreuth, for the excellent working environment they provided and the jokes we shared especially during coffee breaks.

The financial support from German Federal Ministry of Education and Research BMBF under the “FUNgraphen” research project (03X0111A-D) is immensely acknowledged.

To Laura Scherer, for showing me what true friendship means.

I lack words to express my gratitude to my wonderful siblings for their love and support. They proved that family is one’s best friend and I wouldn’t have asked for anything better.

I owe my deepest gratitude to my parents who have given me the opportunity to acquire the best of education. They bore me, raised me, supported me, taught me and loved me.

Away from work, I would like to thank my wife Kristina Marianne immensely for her endless love, understanding and patience.

Finally, I take responsibility for names not specifically mentioned, you have all been amazing.

In memory of my siblings Sylvia and Kenneth

You will always live in my heart

&

To Hannes

Graphical abstract

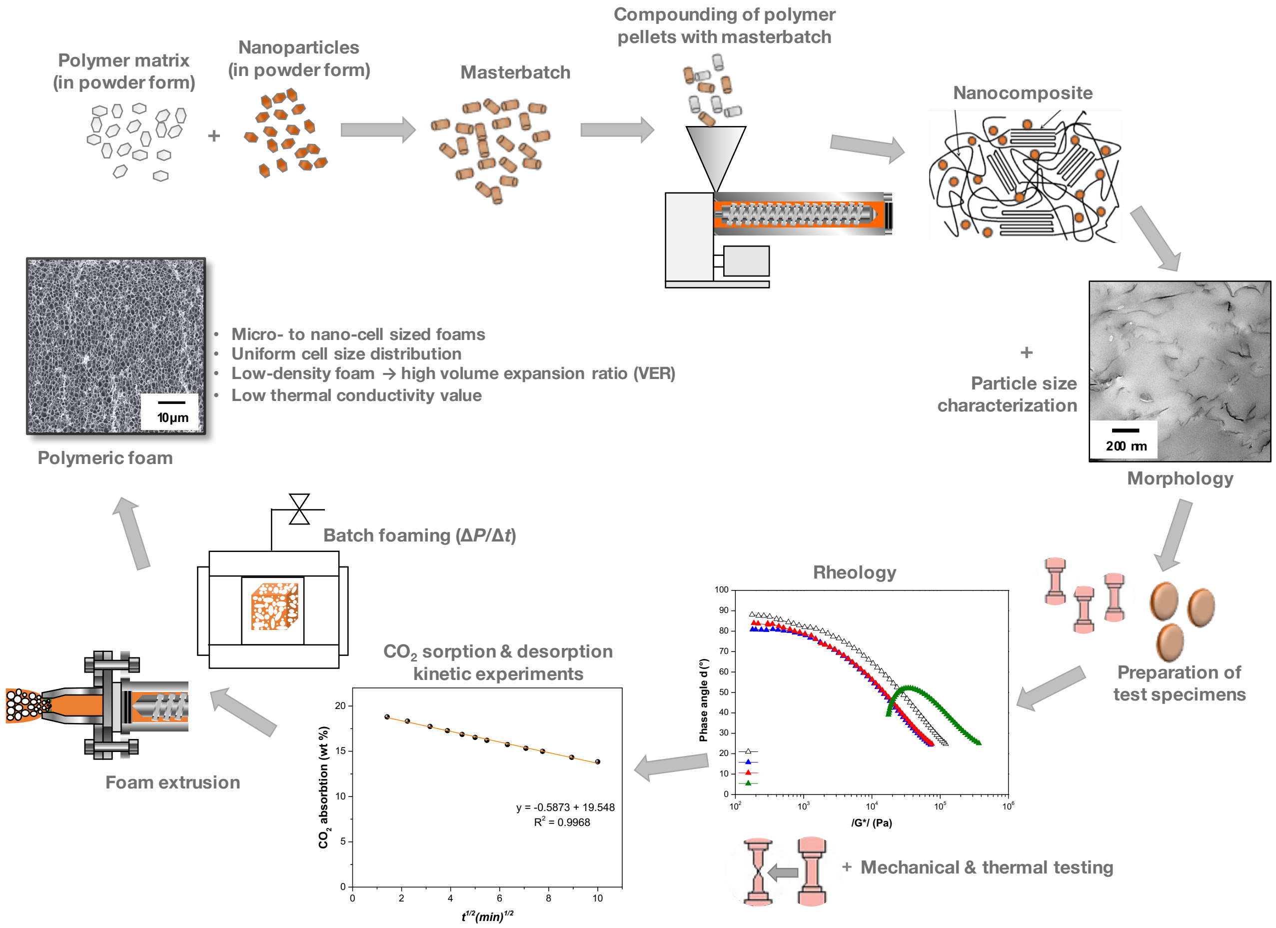

Abstract

The demand for energy-efficient houses has led to greater demand by the building and construction industry for polymeric foam materials with superior thermal insulation properties. The prerequisite for this is the preparation of microcellular or, better still, nanocellular low-density foams. Attaining the aforesaid goal comes of course with several challenges concerning the selection of the right foam base material, nucleating agents, processing conditions and processing techniques.

This work outlines a systematic approach to realize low-density foams based on polystyrene (PS), poly(methyl methacrylate) (PMMA) and blends of polystyrene/poly(methyl methacrylate) (PS/PMMA) by incorporating carbon-based fillers such as carbon black, thermally-reduced graphite oxide and talc (inorganic filler) as cell-nucleating agents. The foaming experiments were performed via batch-process and foam extrusion methods.

The results of this work showed that the quality of the filler dispersion in the matrices depends on the surface functionality of the fillers and the configuration of the screw used to prepare the nanocomposites. Slightly decreased mechanical strength and elongation at break of the non-foamed nanocomposites showed that the fillers are not reinforcing in nature. Different viscoelastic behaviours of the nanocomposites were observed as the filler contents were raised from low to high concentrations. With TRGO, the compact nanocomposites displayed a more elastic character compared to carbon black and talc.

Furthermore, low-density foams with high volume expansion ratios were realized, especially via blending of PS with PMMA. The CO_2-philic (the high affinity of PMMA to carbon dioxide due to the presence of carbonyl oxygen) property of PMMA was exploited to realize the cell densities and nucleation densities of 10^{10} cells/cm^3. Microcellular-extruded PMMA foams that have mean cell sizes of approximately 7 µm at a target density of 190 kg/m^3 were achieved with TRGO filler. Also, the extruded low-density foams realized respectively with polystyrene and PMMA revealed homogeneous cell microstructures and the cell size distributions followed a Gaussian distribution. The thermal conductivity value of extruded PS/TRGO nanocomposite foams were found to be superior to neat polystyrene foams (reference material) and Styrodur® C (a commercially-available extruded polystyrene foam from BASF) by 8 % and 3 %, respectively.

Kurzfassung

Die Nachfrage an energieeffizienten Häusern führt zu einer erhöhten Nachfrage der Bau- und Konstruktionsindustrie an polymeren Schaumstoffen mit hervorragenden Wärmedämmeigenschaften. Voraussetzung hierfür ist die Herstellung von mikrozellulären oder, im besten Fall, nanozellulären Schäumen mit niedriger Dichte. Das Erreichen des oben genannten Ziels bringt natürlich einige Herausforderungen mit sich, wie die richtige Auswahl des Schaumbasismaterials, der Nukleierungsmittel, der Verarbeitungsbedingungen sowie der Verarbeitungstechniken.

Diese Arbeit skizziert einen systematischen Ansatz zur Realisierung von Schäumen mit niedriger Dichte auf Basis von Polystyrol (PS), Polymethylmethacrylat (PMMA) und einem Blend beider Materialien durch Zugabe von kohlenstoffbasierten Füllstoffen wie Ruß (CB), thermisch-reduzierten Graphitoxid (TRGO) und Talk (anorganischer Füllstoff) als Zell-Nukleierungsmittel. Die Schäumexperimente wurden im Batch-Schäumprozess und im Schaumextrusionsverfahren durchgeführt.

Die Ergebnisse dieser Arbeit zeigen, dass die Dispergiergüte der Zell-Nukleierungsmittel in den Matrices zum einen von der Oberflächenfunktionalität des Füllstoffs, zum anderen von der Schneckenkonfiguration des zur Nanokompositherstellung verwendeten Extruders abhängt. Geringfügig niedrigere Festigkeiten und Bruchdehnungen der kompakten Nanokomposite zeigten, dass die Füllstoffe keine verstärkende Wirkung ausüben. Es wurden Unterschiede im viskoelastischen Verhalten der Nanokomposite festgestellt, wenn die Füllstoffbeladung erhöht wurde. Im Vergleich zu Ruß und Talk zeigten die mit TRGO-gefüllten kompakten Nanokomposite einen elastischeren Charakter.

Darüber hinaus wurden Schäume niedriger Dichte mit hohen Volumenexpansionsverhältnisssen realisiert, insbesondere durch das Blenden von PS mit PMMA. Die CO_2-phile Eigenschaft (die hohe Affinität von PMMA zu Kohlenstoffdioxid aufgrund des Carbonyl-Sauerstoffs) von PMMA wurde ausgenutzt, um Zell- und Nukleierungsdichten von 10^{10} Zellen/cm^3 zu realisieren. Mikrozellular-extrudierte PMMA-Schäume mit mittleren Zellgrößen von ca. 7 µm bei einer Dichte von 190 kg/m^3 konnten mit TRGO erzielt werden. Außerdem wiesen die extrudierten Schaumstoffe mit geringer Dichte, die mit PS sowie PMMA realisiert wurden, homogene Zellmikrostrukturen auf und die Zellgrößenverteilungen folgten einer Gauß-Verteilung. Der Wert der Wärmeleitfähigkeit von extrudierten PS/TRGO Nanokompositschäumen war gegenüber des reinen Polystyrolschaumstoffs (Referenzmaterial) und Styrodur® C (ein im Handel erhältlicher extrudierter Polystyrolschaumstoff von der BASF) um 8 % bzw. 3 % überlegen.

Contents

Recurring notations and symbols

Notations

BA	Blowing agent
CB	Carbon black
CBA	Chemical blowing agents
CFCs	Chlorofluorocarbons
CNT	Classical nucleation theory
CO_2	Carbon dioxide
CS	Corn starch
EMA	Ethyl methacrylate
EPDM	Ethylene–propylene-diene terpolymer
EPS	Expandable polystyrene
EtOH	Ethanol
GO	Graphite oxide
HDPE	High-density polyethylene
HMS-PP	High melt strength polypropylene
LDPE	Low-density polyethylene
LS-C	Medium-shear screw configuration
MAM	Poly(methyl methacrylate)-*b*-poly(butylacrylate)-*b*-poly(methyl methacrylate)
MMA	Poly(methyl methacrylate-co-ethyl acrylate)
MMA-co-EMA	Poly(methyl methacrylate-co-ethyl acrylate)
MS-C	Medium-shear screw configuration
MWCNT	Multi-wall carbon nanotubes
NA	Heterogeneous cell nucleating agents
ODP	Ozone depleting potential
PBA	Physical blowing agents
PC	Polycarbonate
PEI	Polyetherimide
PEOc	Poly(ethylene-co-octene)
PF	Phenolic foams
PHBV	Poly(hydroxybutyrate-co-hydroxyvalerate)
PIR	Polyisocyanurate
PLA	Polylactic acid
PMMA	Poly(methyl methacrylate)
PMMA-co-EMA	poly(methyl methacrylate)-(ethyl methacrylate) copolymer
PMMA-MAM	Poly(methyl methacrylate)-co-poly(methyl methacrylate) copolymer
PPE	Poly(2,6-dimethyl-1,4-phenylene ether)
PPE/SAN	Poly(2,6-dimethyl-1,4-phenylene ether)/poly(styrene-co-acrylonitrile) blend
PS	Polystyrene
PS-b-PFDA	Polystyrene-*b*-poly(tetrahydroperfluorodecyl acrylate)
PS/PMMA	Polystyrene/poly(methyl methacrylate) blend
PTFE	Poly(tetrafluoroethylene)
PUR	Polyurethane

SAN	Poly(styrene-co-acrylonitrile)
SAN/MMA-EA	Poly((styrene acrylonitrile)/methyl methacrylate-co-ethyl acrylate) copolymer
SCF	Supercritical fluids
SEM	Scanning electron microscopic image
TEM	Transmission electron microscopic image
TPU	Thermoplastic polyurethane
TRGO	Thermally reduced graphite oxide
VIP	Vacuum insulation panels
XPS	Extruded polystyrene foam
XPMMA	Extruded poly(methyl methacrylate)
XPS/XPMMA	Extruded polystyrene/poly(methyl methacrylate) blend foam copolymer

Symbols

λ_{total}	(mW/mK)	Thermal conductivity of foam
λ_{solid}	(mW/mK)	Thermal conductivity via solid material
λ_{gas}	(mW/mK)	Thermal conductivity via gas molecules
$\lambda_{\text{radiation}}$	(mW/mK)	Thermal conductivity due to radiation
k_{solid}^{0}	(mW/mK)	Bulk solid conductivity
ε	(-)	Emissivity of the inner cell walls
T_i	(K)	Interior temperature
T_e	(K)	Exterior temperature
T_g	(°C)	Glass transition temperature
K_B	($\text{Wm}^{-2}\ \text{K}^{-4}$)	Stefan-Boltzmann's constant
n	(-)	Effective index of refraction
T	(K)	Absolute temperature
$K_{e,R}$	(1/m)	Rosseland extinction coefficient
l	(nm)	Mean free path
K_n	(-)	Knudsen number
d_c	(nm)	Distance between two cell walls
ΔG	(J)	Change in Gibb's free energy
ΔG_{Hom}^{*}	(J)	Gibb's free energy barrier for homogeneous cell nucleation
ΔG_{Het}^{*}	(J)	Gibb's free energy barrier for Heterogeneous cell nucleation
N_{Hom}	($\text{m}^{-3}\ \text{s}^{-1}$)	Rate of homogeneous nucleation
f_0	(1/s)	Frequency factor of the gas molecules to join the nucleus
f	(-)	Energy nucleation factor
m	(m)	Surface curvature of filler particle
C_0	(molecules/cm^3)	Concentration of gas molecules
θ_c	(°)	Wetting or contact angle
β	(°)	Angle of conical cavity of a nucleating agent

ΔG_m	(J)	Gibbs free energy of mixing
ΔH_m	(J/mol)	Enthalpy of mixing
ΔS_m	(J/mol K)	Entropy of mixing
r^*	(m)	Bubble critical radius
ΔP	(Pa)	Pressure drop
$\Delta P/\Delta t$	(Pa/s)	Pressure drop rate
ΔV	(m^3/kg)	Free volume due to the presence of heterogeneous particles
$\emptyset_i$	(-)	Volume fraction of one component in a binary blend mixture
T	(K)	Absolute temperature
S	(-)	Factor describing the energy reduction for heterogeneous nucleation
Ca	(-)	Capillary number
η^*	(Pas)	Complex shear viscosity
η_B	(Pas)	Biaxial viscosity
η_d	(Pas)	Viscosity of the droplet phase
η_m	(Pas)	Viscosity of the continuous phase
η_P	(Pas)	Planer viscosity
η_r	(-)	Viscosity ratio
η_s	(Pas)	Shear viscosity
η_{uE}	(Pas)	Elongational uniaxial viscosity
G'	(Pa)	Storage modulus
G''	(Pa)	Loss modulus
$/G^*/$	(Pa)	Absolute complex modulus
$tan\ \delta$	(°)	Phase angle
ω	(rad^{-1})	Angular frequency
$\dot{\gamma}$	(1/s)	Shear rate
$\gamma_{\alpha\beta}$	(N/m)	Interfacial energy of the nucleant-gas (bubble interface)
R_d	(m)	Radius of the droplet
α	(N/m)	Interfacial tension
T_c	(°C)	Critical temperature
P_c	(MPa)	Critical pressure
T_g	(°C)	Glass transition temperature
$M_{gas\ t}$	(wt%)	Gas concentration at time t
W_t	(g)	Mass of the specimen after time t
W_i	(g)	Initial mass of the sample
D_d	(cm^2/s)	Diffusion coefficient
M_0	(wt%)	Equilibrium gas concentration
M_t	(wt%)	Amount of CO_2 absorbed by the polymer at time t
F	(-)	Foamability factor for closed cell foams

ϕ_m	(µm)	Mean cell size
ρ_{foam}	(kg/m^3)	Foam density
ρ_{rel}	(kg/m^3)	Relative foam density
ρ_{cell}	(cm^{-3})	Cell density
$\rho_{polymer}$	(kg/m^3)	Density of the unfoamed or solid polymer
ρ_p	(kg/m^3)	Density of the nucleating particle
ρ_{nucl}	(m^{-3})	Nucleation density
N_{Nul}	(m^{-3})	Nucleation efficiency of the nucleants
ϕ_m	(µm)	Mean cell size
VER	(-)	Volumetric foam expansion ratio
RER	(-)	Radial expansion ratio
V_f	(-)	Void fraction of foam
fs	(m^3)	Strut volume
M	(-)	Magnification factor of the micrograph
V_p	(m^3)	Volume of individual nucleating particle
w_p	(-)	Weight fraction of a nucleating particle in a polymer composite
M_w	(g/mol)	Weight average molecular weight
MFR	(g/10 min)	Melt flow rate
A_{sp}	(m^2/g)	Brunauer-Emmett-Teller specific surface area
P/P_o	(Pa)	Gas relative pressure
E	(Pa)	Tensile modulus
δ_m	(Pa)	Tensile strength
ε_b	(Pa)	Elongation at break
T_m	(°C)	Melt temperature
N_p	(m^{-2})	Number of particle per area
l_{mp}	(m)	Mean particle lateral length
A_R	(-)	Aspect ratio of filler
l_{ave}	(m)	Average lateral length of filler particle
t_{ave}	(m)	Average thickness of the filler particle
ρ_{mn}	(m^{-2})	Droplet number average density
D_m	(m)	Mean droplet diameter
$T_{saturation}$	(°C)	Batch foam gas saturation temperature
$T_{foaming}$	(°C)	Batch foam Foaming temperature in batch foaming
$P_{saturation}$	(°C)	Foam saturation temperature in batch foaming
t_{cw}	(m)	Cell wall thickness
$t_{s.eq}$	(m)	Equivalent strut thickness
T_{im}	(°C)	Inlet melt temperature in the extruder barrel just before the die
T_{die}	(°C)	Die temperature

1 Introduction

Thermoplastic polymer foams are cellular materials consisting of gaseous voids packed by a denser polymer matrix. Their diverse properties such as light weight, high relative strength, high surface-volume ratio and resilience makes them versatile materials for packaging, acoustic, prosthetic, cushioning and thermal insulation applications [1,2]. The application of polymeric foams depends greatly on their cellularity[1], wall stiffness[2], cell size and weight. The cell size and foam density are the two most important foam characteristics because careful control of both features dictates the product's overall performance and cost.

The development of polymeric closed-cell foams started in the early 1930s and, in 1931, the first patented extruded closed-cell foam made out of polystyrene (PS) was granted to Munters C. G. et al. [1]. These foams were macrocellular; i.e. they had an average cell size larger than 100 µm.
Further development in this direction continued until, in 1981, Martini J. E. et al. [3] at Massachusetts Institute of Technology (MIT) invented microcellular foams[3]. These foams were processed via a solid-state batch foaming technique using supercritical CO_2 as a blowing agent. The motive behind their invention was to reduce material weight and save costs.

The advancements made in polymer foam processing technologies from the late 1980s to late 1990s brought about the classification of foams into the following categories:

- Fine-celled foams. They are foams with a mean cell size (ϕ_m) between 10 µm and 100 µm.
- Microcellular foams. Foams with a mean cell size of less than or equal to 10 µm and cell densities larger than 10^9 cells/cm^3.

These classifications, however, failed to specify the corresponding foam density ranges or volume expansion ratios (*VER*) to be fulfilled.

It is a known fact supported by several studies in the literature [4–9] that microcellular foams possess superior properties in comparison to conventional foams. Consequently, it was expected that foams with smaller mean cell sizes (nanocellular foams)[4] would offer even far superior properties, especially in areas of thermal insulation where the so-called “Knudsen effect”[5] could be exploited to decrease the thermal conductivity of polymeric foams.

From early 2000 to date, the foam industry began a paradigm shift towards nanocellular foams (Figure 1.1). But in spite of the extensive research studies [10–13] that have focused on achieving this target, the realization of even microcellular low-density foams, i.e. foams with *VER* larger than 10, remains a hurdle. Several attempts have also been made where the use of tailor-made fillers, as well as the use of different combinations of blowing agents and fine-tuned processing parameters did not yield

---

[1] Open-cell or closed cell or a mixture of both.

[2] Flexible or rigid cell walls.

[3] Foams with an average cell size of less than or equal to 10 µm with cell densities exceeding 10^9 cells/cm^3.

[4] Foams having an average cell size < 1 µm with cell densities > 10^{15} cells/cm^3.

[5] Thermal conduction of gas molecules in restricted spaces such as in cell walls of polymer foams.

satisfactory results [14–16].

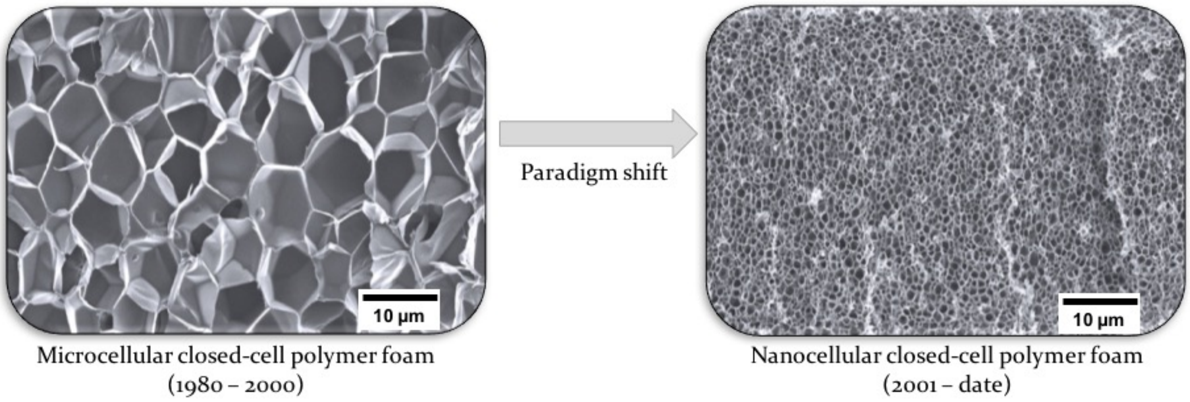

Figure 1.1: Paradigm shift from microcellular to nanocellular closed-cell foams.

Polystyrene (PS), due to its cellular structure, light weight and cost effectiveness, has become the most widely-used thermoplastic polymeric foam for thermal insulation applications, especially in commercial and domestic buildings [17]. PS foams (XPS[6] and EPS[7]) account for roughly 32 % of the European thermal insulation market as of 2017 [17]. In spite of the advantages PS foams offer, they have an inherently high burning rate and high smoke emissions that emanate from the benzene rings of the material [18].
Additionally, without the use of fillers, PS in itself performs poorly as a weak infrared-wave absorbing material [19], thus offering low insulation performance during service life, especially when thermal radiation is increased.

The outstanding weatherability, lower burning rate, and lower smoke emissions due to the absence of the phenyl group in poly(methyl methacrylate) (PMMA) [18] make it a potential candidate for thermal insulation applications and also an alternative to or possible substitute for PS. The aforesaid inherent properties would minimize, to a large extent, the need for incorporation of high amounts of flame-retardants as is usually done with PS, hence reducing the overall cost.
Unlike PS, PMMA can absorb infrared radiation at wavelengths of between 2.8 µm and 25 µm [19], meaning that foams made out of PMMA would block infrared radiations more effectively.
PMMA is also well known to be CO_2-philic because of the Lewis acid-base interaction that takes place between its carbonyl oxygen and CO_2 [20]. This high absorption behaviour of PMMA can be exploited to reduce the foam densities. In addition, it points to PMMA as a potential candidate for the fabrication of microcellular and nanocellular nanocomposite foams.

The motivation of this thesis is to prepare low-density nanocomposite closed-cell foams based on PS, PMMA and PS/PMMA immiscible blends. These targets are realized by the use of carbon-based fillers, coupled with fine-tuning of the foam blend ratios and processing parameters.
Carbon-based fillers already known to absorb and/or reflect infrared radiation [21,22] are used as cell

---

[6] XPS: extruded polystyrene foam.
[7] EPS: expandable polystyrene bead foam.

nucleating agents. The influence of the individual filler geometries and filler content on the cell size, cell size distribution and thermal conductivity of the nanocomposite foams are investigated.

Via blending, the high CO_2 absorption of PMMA is exploited to improve foam processability by decrease of the glass transition temperature (T_g). Blending also aims at increasing the absorption and retention of the blowing agent which, in turn, leads to: (i) increase of the foam cell densities above 10^9 cells/cm^3, (ii) decrease of the foam mean cell size below 10 µm, and (ii) increase of the volume expansion ratio to values higher than 10.

Batch-foaming and foam extrusion techniques are used in this work to fabricate the nanocomposite foams.

2 Theoretical background and literature review

2.1 Thermal conductivity in polymeric closed-cell foams

In foams, thermal conductivity (λ) is the total amount of heat that flows through a material of defined thickness under a temperature difference. Heat flow across such foams as shown in Figure 2.1 occurs via the following transport mechanisms:

- Conduction through the movement of free electrons or lattice vibrations[8] of the molecules in the solid and gas phases.
- Convection via atom or molecule exchange of the fluids. This can be ignored if the cell size is less than 4 mm [23].
- Radiation via photons of the cell wall and cell struts.

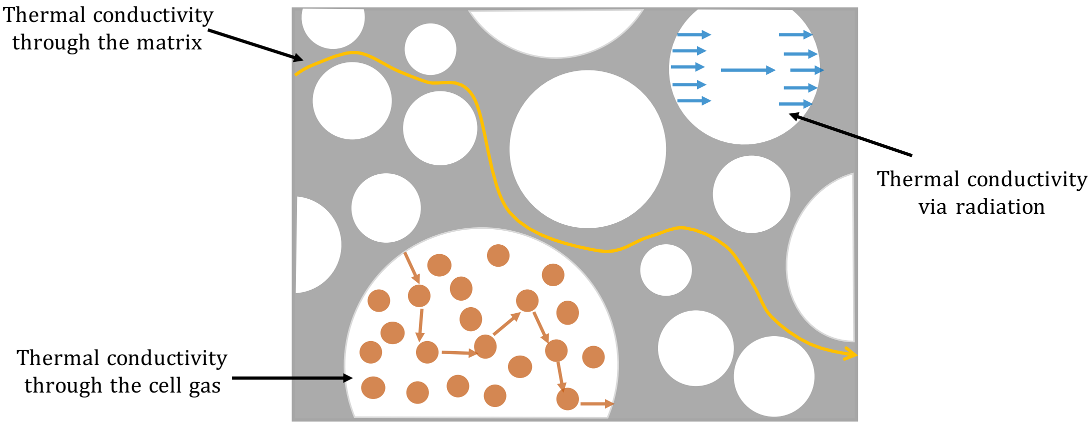

Figure 2.1: Thermal conductivity through a polymeric foam.

Thus, the total thermal conductivity of a polymer foam (λ_{total}) can be estimated by using the expression in equation 2.1 [23].

$$\lambda_{total} = \lambda_{solid} + \lambda_{gas} + \lambda_{radiation} \tag{2.1}$$

where λ_{solid} is the solid conductivity, λ_{gas} is the conductivity via the gas molecules and $\lambda_{radiation}$ accounts for the radiative contribution. The mathematical expressions for λ_{solid}, λ_{gas} and $\lambda_{radiation}$ are given in equations 2.2 to 2.4 [24].

$$\lambda_{solid} = (1 - V_f)(\tfrac{2-fs}{3})k_{solid}^{0} \tag{2.2}$$

---

[8] Thermal conductivity through phonons.

$$\lambda_{gas} = \frac{\sigma}{(\frac{2}{\varepsilon}-1)} \frac{(T_i-T_e)^4}{(T_i-T_e)} \tag{2.3}$$

$$\lambda_{radiation} = \frac{16\mathrm{n}^2 K_B T^3}{3K_{e,R}} \tag{2.4}$$

V_f represents the void fraction of the foam, fs denotes the strut volume and $\mathrm{k}^0_{\mathrm{solid}}$ is the bulk solid conductivity. In equation 2.3, ε is the emissivity of the inner cell walls[9], T_i is the interior (indoor) temperature (K) and T_e stands for the exterior (outdoor) temperature (K). In equation 2.4, K_B is the Stefan-Boltzmann's constant, n signifies the effective index of refraction, T stands for the absolute temperature (K) and $K_{e,R}$ is the Rosseland extinction coefficient[10] [24]. Additionally, of all three modes of heat transport, the λ_{gas} is presumed to have the highest contribution ($\lambda_{gas} \geq 50$ %) [25][26].

The classical Stefan's Boltzmann law given in equation 2.3 describes the relationship between the radiative thermal conductivity and operating temperatures and, according to Figure 2.2, the amount of solar radiation that reaches the surface of an exterior wall of a building is linked to heat build-up that is equal to or above 70 °C. Therefore, it is reasonable to expect that, at higher temperatures, the influence of $\lambda_{radiation}$ will increase relative to λ_{solid} and λ_{gas}. Similarly, it is expected carbon-based fillers such as graphene will absorb more infrared radiation at such high temperatures.

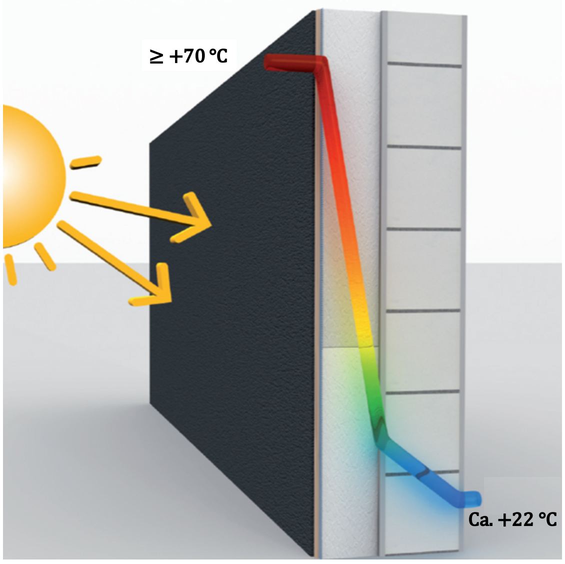

Figure 2.2: Typical surface temperature of exterior wall of buildings (*adapted from www.brillux.com*).

---

[9] ε is assumed to be identical for all cells.

[10] Absorption plus scattering coefficient.

The strategies to lower the λ_{total} to the lowest value possible are:

- To decrease the foam bulk density. In other words, decreasing the solid fraction of the cell wall and struts will reduce λ_{solid}.
- Having nano-sized foam cells. This will lower λ_{gas} via the so called "Knudsen effect".
- Inclusion of infrared absorbing and reflecting fillers such as carbon black, expanded graphite, functionalized graphenes etc. in order to decrease $\lambda_{radiation}$ [21,22,27].

2.1.1 Knudsen effect in polymeric foams

"Knudsen effect" describes the contribution of gas molecules in restricted spaces to the thermal conductivity. It occurs when the cell sizes of the foams are less than the mean free path[11] (75 nm) [28] of air molecules at ambient temperature and pressure. This effect comes into play as collision among the confined gas molecules becomes insufficient, thereby upsetting the energy transfer[12] between the gas molecules and the cell walls.

Fundamentally, it is based collectively on the kinetic theory of gas, thermal conduction through cellular structures and Rosseland diffusion approximation of thermal radiation [27]. The relationship between the cell size and the mean free path (l) is defined by the Knudsen number (K_n) in equation 2.5 [29].

$$K_n = {}^{l}/_{d_c} \tag{2.5}$$

where l is the mean free path of the gas molecules and d_c is the distance between two cell walls. The effect of the mean cell sizes on λ_{gas} is graphically presented in Figure 2.3 [30]. It is clear that λ_{gas} is reduced by almost 50 % when the mean cell size is approximately 200 nm. A tremendous reduction is further observed as the cell size approaches 100 nm.

Furthermore, Gong P. et al. [24] investigated the influence of PS foams nucleated with MWCNT on λ_{gas}. They observed that the λ_{gas} increased from 23.6 mW/mK to 24.8 mW/mK for foams of the same *VER* when the ϕ_m changed from 5 µm to 100 µm. By this, they clearly demonstrated the contribution of the Knudsen effect as a function of cell size.

Also, it has been experimentally proven in a few published articles [31,32] that nanocellular foams at low density exhibit remarkable thermal insulation properties compared to microcellular foams due to the Knudsen effect.

---

[11] The mean free path is the average distance gas molecules travel between successive collision

[12] This energy transfer is due to vibration

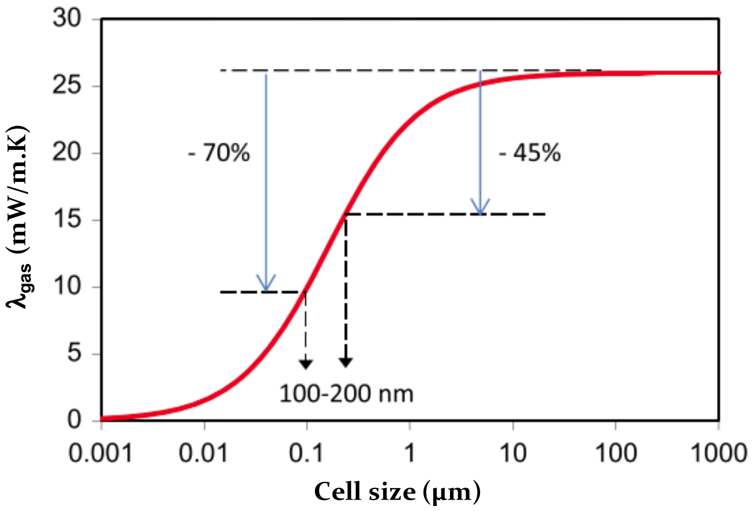

Figure 2.3: Theoretical predicted reduction of the thermal conductivity (λ_{gas}) component via the Knudsen effect with decreasing cell size [30].

2.1.2 Traditional versus state-of-the-art thermal insulation materials

Generally, materials used for thermal insulation purposes have attracted much attention, especially from industrial and governmental agencies. This is because of the need to improve the energy efficiency of buildings and to reduce rising greenhouse gas emissions. Based on the survey report [17] on the European Thermal Insulation Market, commercial and domestic buildings consume the bulk (87 %) of insulation materials while the rest (13 %) is used by the construction (process plant, pipe lagging, transport, domestic appliances etc.) industry.

The λ values of traditional and state-of-the-art insulation materials are presented in Figure 2.4. To date, vacuum insulation panels (VIP), which are a state-of-the-art material, offer the lowest λ values (5 ± 2 mW/mK) but they are much more expensive to purchase than traditional ones. The thermal conductivity values of some of these commercially available insulation materials are summarized and compared in Table 2.1

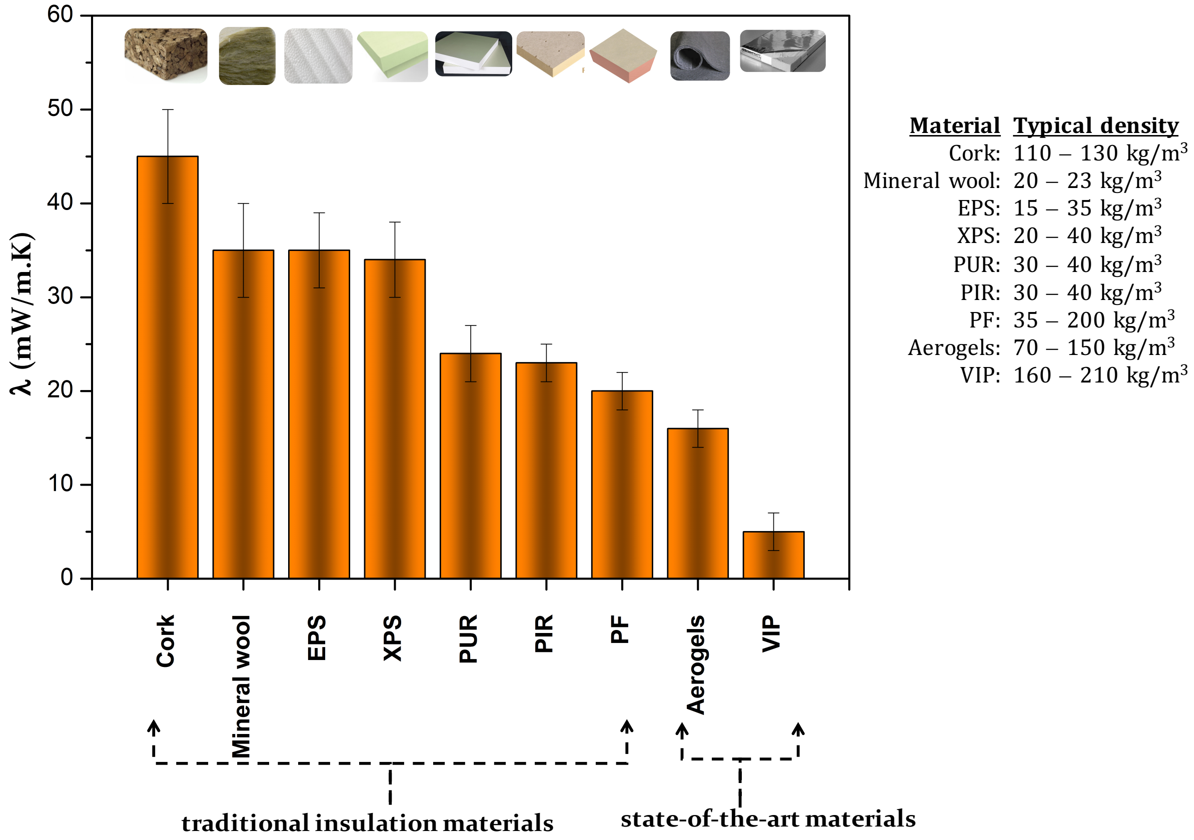

Material	**Typical density**
Cork:	110 – 130 kg/m^3
Mineral wool:	20 – 23 kg/m^3
EPS:	15 – 35 kg/m^3
XPS:	20 – 40 kg/m^3
PUR:	30 – 40 kg/m^3
PIR:	30 – 40 kg/m^3
PF:	35 – 200 kg/m^3
Aerogels:	70 – 150 kg/m^3
VIP:	160 – 210 kg/m^3

Figure 2.4: Typical thermal conductivities and densities values [33–35] of various insulation materials at normal operating conditions. *EPS: expandable polystyrene, XPS: extruded polystyrene, PUR: polyurethane, PIR: polyisocyanurate, PF: phenolic foams, VIP: vacuum insulation panels.*

Table 2.1: Thermal insulation performance of traditional and state-of-the-art materials [36–43].

Material type	Brand name	Company	λ values (mW/mK)
VIP	va-Q-pro	Va-Q-Tec	4
	OPTIM-R	Kingspan	7
Aerogel	Calostat	Evonik	19
	Slentite	BASF	17
	Spaceloft	Aspen aerogels	14
PF	Xtratherm (SR/CW)	Kingspan	20
PIR	Xtratherm (Thin-R XT/CW)	Kingspan	22
XPS	Styrodur® 3000 CS	BASF	33
EPS	Styropur®	BASF	31 - 38

Note: Lower λ values are preferred for thermal insulation application purposes.

2.2 Microcellular to nanocellular polymer foams: A review

In order to realise the full benefit of polymeric foams as efficient thermal insulation materials, they must possess two important properties, which are:

- Small mean size cells, i.e. cells less than 1 µm.
- Very high VER > 10. In other words, the foam density must be less than 64 kg/m^3 [44].

Since the goal of this thesis is to prepare low-density nanocomposite foams based on PS, PMMA and blends of PS/PMMA using carbon-based fillers, it is pertinent to consider other studies with similar goals but where different polymer matrices were used. Therefore, a compendium of polymeric foams taken from the literature over the last decade that generated the smallest mean cell sizes coupled with $VER \leq 10$ is presented graphically based on the most frequently used foam processing technologies, which are: the batch and foam extrusion process.

2.2.1 Microcellular and nanocellular foams manufactured via batch foaming process

The batch foaming process can either be temperature-induced or pressure-induced (section 2.7.2). A survey of the literature revealed that the pressure-induced batch foam method was the most frequently used technique of the two. Figure 2.5 summarizes a collection of microcellular and nanocellular foams [2,30,31,45–74]. These foams have been classified into high density, medium-density and low-density based on their volume expansion ratios. It can be clearly seen that the base polymer matrices cut across the entire range of thermoplastics (commodity, engineering, high-performance). Below are some of the studies producing foams that came closest to achieving the aforesaid ultimate goal.

Costeux S. et al. [30] processed, via a pressure-induced method, PMMA-co-EMA[13] foams with silica as a heterogeneous nucleating agent. They applied in their experiments a pressure of 30 MPa and temperature of 40 °C. With a 30 wt% CO_2 uptake by the matrix, medium-density nanocellular foams having a ϕ_m of 95 nm, cell density (ρ_{cell}) of 8.6 x 10^{15} cells/cm^3 and a VER of 4.88 (absolute density of 242 kg/m^3) were realized. In a similar study, Costeux S. et al. [75] prepared PMMA-co-EMA[14] foams. No nucleating agents were used and the foaming temperature was 5 °C lower than in their previous study. The CO_2 uptake by the copolymer was up to 40 wt% presumable caused by the additional 1 wt% EMA in the copolymer. The ϕ_m was decreased from 90 nm to 80 nm, while the cell density and VER increased to about 15 x 10^{15} cells/cm^3 and 5, respectively. The cell size achieved was only 10 nm larger than the theoretical cell size of 70 nm for the “Knudsen effect” but, nonetheless, they were far from being classified as low-density foams.

---

[13] A random copolymer with of poly(methyl methacrylate) with 50 wt% ethyl methacrylate.

[14] EMA content in the copolymer is 51 wt%.

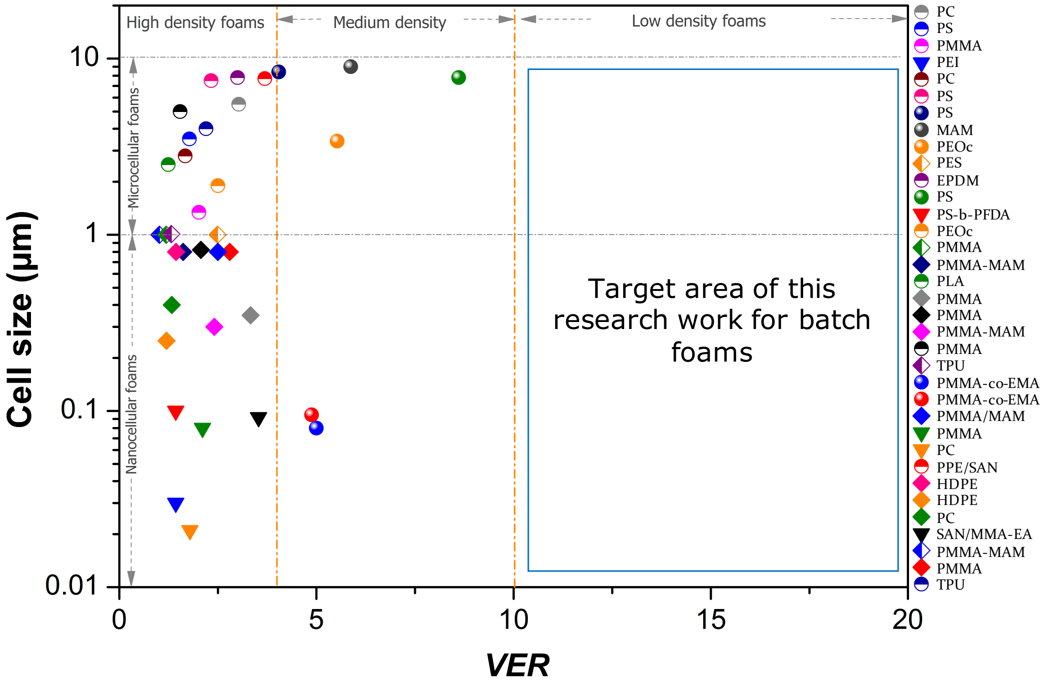

Figure 2.5 illustrates a plot of mean cell sizes as a function of volume expansion ratios of various thermoplastic closed-cell foams prepared via batch foaming [2,30,31,45–74].

Furthermore, a 50/50 wt% miscible blend of SAN/MMA-EA[15] blend foams was prepared via a pressure-quench batch process by Costeux S. et al. [63]. The SAN contains 28 wt% acrylonitrile while MMA-EA[16] contains 9 wt% of EA. The high affinity to CO_2 by the MMA-EA component in the blend enabled the dissolution of 36.5 wt% of CO_2 compared to SAN (21.9 wt%). Their study produced foams that were characterized by a ϕ_m of 92 nm, ρ_{cell} of 4.7 x 10^{15} cells/cm^3 and *VER* of 3.5. By definition and classification, the foams produced from their study of SAN/MMA-EA were nonetheless high-density nanocellular foams.

Guo H. et al. [61] processed polycarbonate (PC) without nucleating agents into foams via a temperature-induced method by saturating the samples at -30 °C for 72 h. The samples absorbed about 20.4 wt% of CO_2 and foaming was carried out at 70 °C in a hot silicon oil bath. Their experiment resulted in high-density (670 kg/m^3) nanocellular foams having ϕ_m of 21 nm, ρ_{cell} of 4 x 10^{14} cells/cm^3 and *VER* of 0.56.

Miller D. et al. [73], by means of a temperature-induced batch foam process, saturated PEI[17] sheets (1.5 mm in thickness) at 21 °C with a pressure of 5 MPa for 280 h. The samples absorbed 40 wt% of CO_2 and were foamed in a hot silicon oil bath to obtain high-density nanocellular foams with the following characteristics: ϕ_m of 30 nm and *VER* of 1.4.

---

[15] Poly((styrene acrylonitrile)/methyl methacrylate-co-ethyl acrylate).

[16] Methyl methacrylate-co-ethyl acrylate.

[17] Poly(ethylenimine).

Yang J. et al. [50], via a pressure-induced batch process, saturated PS nanocomposites filled with 5 wt% of spherical-ordered mesoporous silica (OMS). They showed that the CO_2 absorption capacity of unfilled PS and PS/5 wt% OMS was similar. They absorbed between 10.33 wt% and 10.53 wt%, respectively. The PS-OMS samples were processed at 120 °C for 18h under high pressure, which was released under 0.5 seconds. The samples were cooled afterwards with ice water to fix the morphology. The foams were characterized by a $\phi_m$of 7.8 µm, ρ_{cell} of 3.55×10^9 cells/cm^3 and a *VER* of 8.6. These foams were still medium-density but displayed the highest *VER* of all batch foams presented in the plot in Figure 2.5.

2.2.1.1 Conclusion on micro-and nanocellular batch foams

A one-to-one comparison between the mean cell sizes and *VER* of foams prepared with same polymer by different authors cannot be made due to slight differences in the amount of physical blowing agent dissolved, filler type/filler content and variations in processing parameters. However, the following points could be deduced from the survey:

- The saturation temperatures as well the foaming temperatures account for the major differences observed in ϕ_m and *VER*. In addition to that, foams fabricated at pressures higher than 13 MPa and at temperatures (*T*) above 100 °C or at $T > T_g$ of the base polymer resulted in medium-density foams (*VER* ≥ 4 - 10) with larger $\phi_m > 6$ µm. The effect of a high foaming temperature on the polymer density was more pronounced compared to the effect of s higher pressure [76,77].
- Foams which were seen to have $\phi_m \leq 1$ µm were mostly prepared either at relatively low temperatures or at temperatures well below their normal T_g and at relatively high pressures of up to 35 MPa.
- Foams which generated ϕ_m as low as 150 nm were fabricated with CO_2-philic homopolymers, copolymers or blends. These polymers were shown to absorb at least 20 wt % of CO_2 [61,63].
- From all indications, high pressure drop rates and relatively low temperatures are necessary to obtain nanocellular foams but processing at such low temperatures could produce foams with densities closer to the density of the non-foamed material. e.g. with PMMA-MAM[18] copolymer [69].
- Moderate use of nucleating agents (0.01 wt% to 5 wt%) that possessed high specific surface areas decreased the $\phi_m$of foams significantly.

---

[18] MAM: poly(methyl methacrylate)-block-poly(butylacrylate)-block-poly(methyl methacrylate).

2.2.2 Microcellular and nanocellular manufactured via foam extrusion

It is easier to prepare low-density foams with very high volume expansion ratios (*VER* ≥ 10) via extrusion than by a batch foaming process. This is because the loss of blowing agent through the foam skin can be minimized by adjustment of the processing temperatures, especially the die temperature [1,78]. Lower processing temperatures have generally led to microcellular foams with higher *VER* [16,79].

Figure 2.6 shows a graphical representation of extruded foams reported in the literature [5,13,44,80–98]. A first look at the plot shows that commodity plastics were predominantly used as base materials. Therefore, the scope of this section will be to discuss only foam studies irrespective of their polymer matrix, which gave foams with the smallest mean cell sizes coupled with high *VER*.

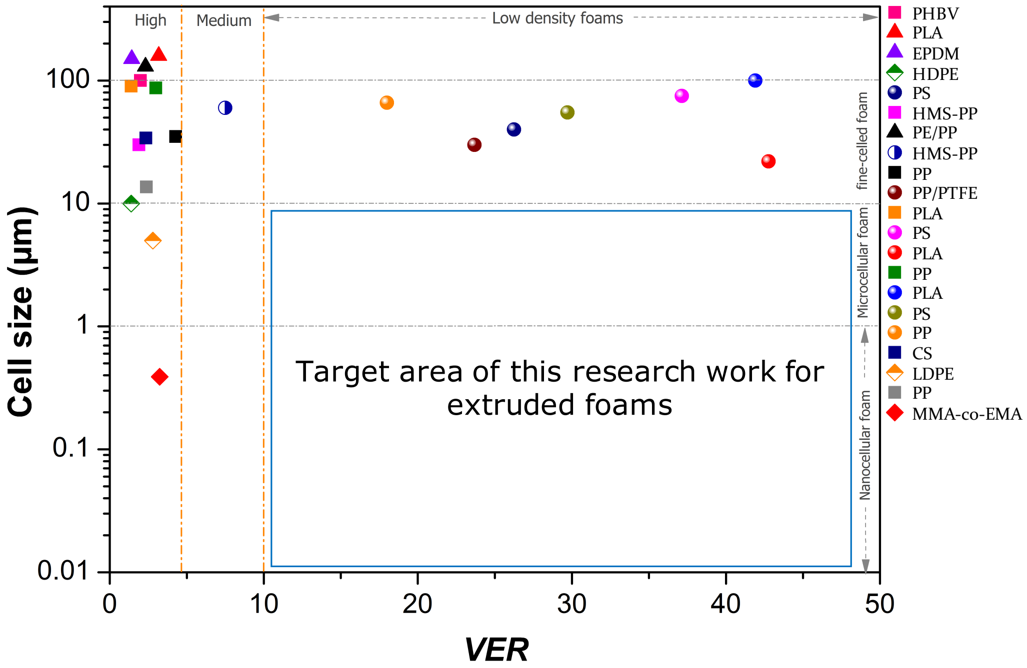

Figure 2.6: Plot of mean cell sizes as a function of volume expansion ratio of various thermoplastic closed-cell foams prepared via foam extrusion [2,30,31,45–74].

Homopolymers

Zhang C. et al. [82] prepared extruded polystyrene foams by using CO_2 and water as a co-blowing agent. For their experiment, a throughput of 4 kg/h, a slit die of 0.4 mm and a die temperature of 120 °C were used. The authors were able to generate fine-celled (75 µm) low-density foams (*VER*: 37.14) nucleated with 0.5 wt% of graphite (GR).

Larson A. et al. [84] processed PLA into foams using a single-line extruder using 2 % epoxy-functionalized chain extenders in the form of a masterbatch. By metering 8 wt% of CO_2 at a fixed die temperature of 125 °C, they obtained low-density fine-celled (22 µm) foams demonstrating a very high *VER* of 42.76.

In another similar study, Mihai M. et al. [86] incorporated 0.5 wt% of chain extenders (epoxy-styrene-acrylic oligomer) into PLA. They metered in to PLA 9 wt% of CO_2 at a fixed die temperature of 120

°C. Low-density fine-celled (100 µm) foams having a very high *VER* of 41.9 were generated.
One peculiarity found in both studies is the use of specially-designed co-rotating screws to process PLA foams. Emphases were placed on the screw configuration and the specific number of zones in the barrel in order to ensure adequate mixing, control and maintenance of pressure build-up
Xu Z. et al. [97] studied the foaming behaviour of HMS-PP with SiO_2 as a cell nucleating agent. They performed their studies on a single-screw-single-line extruder by fixing the die temperature at 160 °C. The use of a combination of CBAs: Azodicarbonamide[19] and EPTcor 882[20] resulted in fine-celled-medium-density fine-celled foams characterized by a low *VER* of 7.5 and a mean cell size of 60 µm.
Chaudhary A. K. et al. [85], incorporated 3 wt% of organoclay into PP and an unstated amount of maleic-anhydride-grafted-polypropylene (PP-g-MA) as a compatibilizer. Using a single-screw extruder with a fixed die temperature of 145 °C, the authors generated high-density fine-cellular (87 µm) foams characterized by a very low *VER* of 3.
Both investigations reveal one interesting point, which is that the temperature of the die is always set some few degrees higher than the T_m of PP.

Lee Y. H. et al. [5] prepared extruded LDPE nanocomposites foams with as little as 0.05 wt% layered silicate in addition to 15 wt% of LLDPE-g-maleic anhydride, which served as a coupling agent. By metering 8 wt% of CO_2 and setting the die temperature to 95 °C[21], they were able to generate high-density-microcellular foams having ϕ_m of 5 µm at a very low *VER* of 3.6.

Copolymers

Costeux S. et al. [90] used a single-line extruder equipped with a long residence time cooling device which was fixed before the die element, to produce the only extruded nanocellular foam (XMMA-EA) available to date in the literature. With a CO_2 content of 20 wt% along with 0.25 wt% of silica particles as nucleating agents, they successfully produced nanocellular foams having a ϕ_m of 389 nm. The *VER* (3.24) of these foams were found to be very low meaning that they are of high densities.

2.2.2.1 Conclusion on extruded foams

It is obvious from Figure 2.6 that there are neither microcellular nor nanocellular low-density foams. In view of this, the target of this research work will be the areas marked in blue boxes in the above figures. Another important observation is that some of the frequently used polymers in batch foaming studies are currently not being investigated in many foam extrusion studies. For instance, there are virtually no articles on extruded PMMA (XPMMA) despite the fact that its high CO_2 retention capacity could be exploited to make low-density foams. A reason for this may lie in the price of PMMA which, based on market surveys (2016), was found to cost: (2.60 - 3.2) € per kg in comparison to PS (1.20 -1.40) € per kg.

---

[19] An exothermic chemical blowing agent.
[20] An endothermic chemical blowing agent.
[21] A relatively low temperature for foam extrusion.

2.2.3 Conclusion on micro-and nanocellular batch and extruded foams

Although huge advancements have been made in the production of microcellular and nanocellular foams, the bulk of these investigations has focused on cell size reduction at the expense of high foam density, which beyond question is one of the most important properties of polymeric foams.
Furthermore, in order to further advance the foam processing research community, the following should be stated in any article published in the future:

- The bulk density of the pure polymer material or unfoamed polymer.
- The mean cell sizes along with either one of the following: foam densities or volume expansion ratios or the relative densities.
- The amount of blowing agent absorbed by the samples, the processing temperatures and the pressure drop rates observed in foaming.

And based on the findings of this survey, the following conclusions are made:

- To date, there has been no success at fabricating low-density-nanocellular foams by any of the foam processing techniques that have been considered in this survey. The closest results achieved are: (i) medium-density-nanocellular foams based on PMMA-co-EMA [30,75] and (ii) high-density-nanocellular foams based on MMA-EA [90]. Both foams were respectively prepared via batch and foam extrusion methods.
- The realization of low-density nanocellular foams can be made possible when copolymers and blends with very high affinity for CO_2 (> 20 wt%) are employed.
- CO_2 appears to be the chief blowing agent for processing of foams via batch process and foam extrusion.
- It took over 20 years (1980-2000) for the foam community to shift completely from macrocellular to microcellular foams and a period of over 15 years to move to making nanocellular foams.
- Polymers with $T_g > 130$ °C usually produced foams with smaller mean cell sizes while polymers with T_g below 130 °C are able to yield foams with low densities.
- The possibility to produce closed-cell nanocellular low-density foams ($VER \geq 50$) using the aforementioned technologies could be conceivable in the near future with the development of new novel materials which include: nucleating agents, copolymers, blends, combination of blowing agents. More Advanced processing techniques will also help to achieve this target.

2.3 Foaming principle and process

2.3.1 Cell nucleation in polymeric foams

Nucleation is the first step in the fabrication of polymeric foams and it occurs by random formation of distinct thermodynamic nuclei that have the ability to irreversibly grow into larger sized nuclei within the body of a metastable parent phase[22]. The resultant nuclei as shown in Figure 2.7 have free energies lower than the parent phase. The difference in free energy between the two systems is the driving force behind the transformation. In relation to the foaming process, the resultant nuclei and parent phases are referred to as the bubble[23] and polymer melt, respectively.

2.3.1.1 Classical nucleation theory

The classical nucleation theory (CNT) is an empirical theory most frequently used to describe the mechanisms of cell nucleation and growth in polymeric foams. The postulations and approximations of CNT are highlighted below [99–101].

- All nuclei are spherical droplets with distinct sharp boundaries.
- The nuclei possess the same physical properties as the bulk.
- The effect of pressure drop[24] (ΔP) on cell nucleation is taken into account but with disregard for pressure drop rates ($\Delta P/\Delta t$).
- An instantaneous pressure drop is followed by instantaneous nucleation. This scenario is improbable in reality because pressure drop occurs over a period of time.
- Cell interfaces are infinite flat planner surfaces.

Due to these assumptions and approximations adopted by CNT, a couple of published works [99,102] have demonstrated some remarkable deviations from this theory and these have called to question the accuracy and validity of the CNT. Nonetheless, and in spite of these shortcomings, the CNT provides a dominant conceptual understanding of the cell nucleation process in polymeric foams. Henceforth, it shall be adopted to further explain the mechanism of bubble nucleation and growth with respect to polymeric foams.

The CNT classifies cell nucleation into two categories, namely: homogenous and heterogeneous cell nucleation and these are schematically presented in Figure 2.8 for visualization purposes.

Classical homogeneous cell nucleation

Homogenous cell nucleation involves the spontaneous formation of cells without the presence of any heterogeneous particle or pre-existing cavities present in the development stage. This usually occurs in response to random fluctuations or changes in temperature or pressure. The free energy barrier (ΔG) reaches a high-energy maximum when R (Figure 2.7) equals the critical radius (r^*). The critical

---

[22] The metastable parent phase is the polymer melt.

[23] Foam cell.

[24] The difference between the internal cell pressure and the pressure surrounding the cell.

radius represents the minimum size a nucleus must attain before it can grow to become a stable bubble or cell.

There are two scenarios as shown in Figure 2.7 that could occur depending on the apparent size of the nucleus:

i. When $R < r^*$, the nucleus collapses back into the polymer melt.
ii. When $R > r^*$, a stable nucleus is formed and will continue to grow until it stabilizes.

Also, the stability of the cells depends on the competition between the pressure drop (ΔP) and the interfacial energy[25] ($\gamma_{\alpha\beta}$). By taking these factors into account, an expression for the Gibb's free energy of cell nucleation is obtained as shown in equation 2.6 [59].

$$\Delta G(R) = -\frac{4}{3}\,\pi R^3 \Delta P + \pi R^3 \gamma_{\alpha\beta} - \Delta V_{free\ vol} \tag{2.6}$$

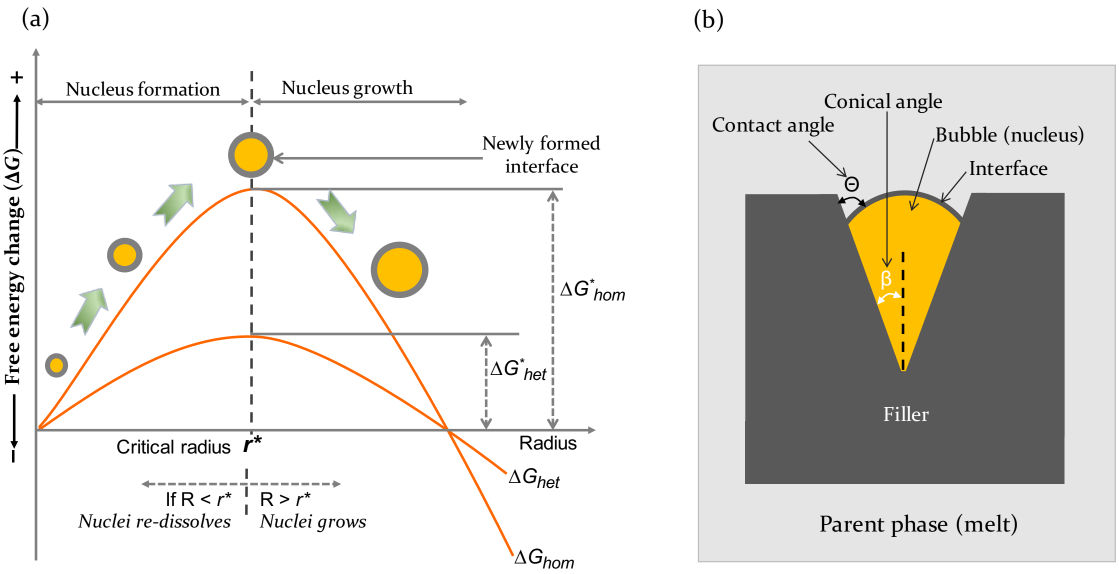

Figure 2.7: Modified schematic diagram [100] of (a) bubble nucleation and growth as a function of free energy, (b) contact angle and semi-conical angle for heterogeneous bubble nucleation.

The dependence of r^*on ΔP and the $\gamma_{\alpha\beta}$ is expressed in equation 2.7. Consequently, the Gibb's free energy barrier for homogeneous nucleation (ΔG^*_{Hom}) can be expressed in equation 2.8 as:

$$r^* = \frac{2\gamma_{\alpha\beta}}{\Delta P} \tag{2.7}$$

$$\Delta G^*_{Hom} = \frac{16\,\pi\,\gamma^3_{\alpha\beta}}{3\Delta P^2} \tag{2.8}$$

---

[25] Also referred to as surface energy.

Since homogenous nucleation occurs in the absence of heterogeneous particles, the ΔV term in equation 2.6, which accounts for free volume[26] due to the presence of heterogeneous particles, can be ignored. Hence, the rate of homogenous nucleation (N_{Hom}) can be calculated from the expression derived in equation 2.9.

$$N_{Hom} = f_0 C_0 \exp\left(\frac{-\Delta G^*_{hom}}{K_B T}\right) \tag{2.9}$$

where f_0 is the frequency factor of the gas molecules to join the nucleus[27], C_0 is the concentration of gas molecules, K_B is the Stefan-Boltzmann's constant and T is the temperature.

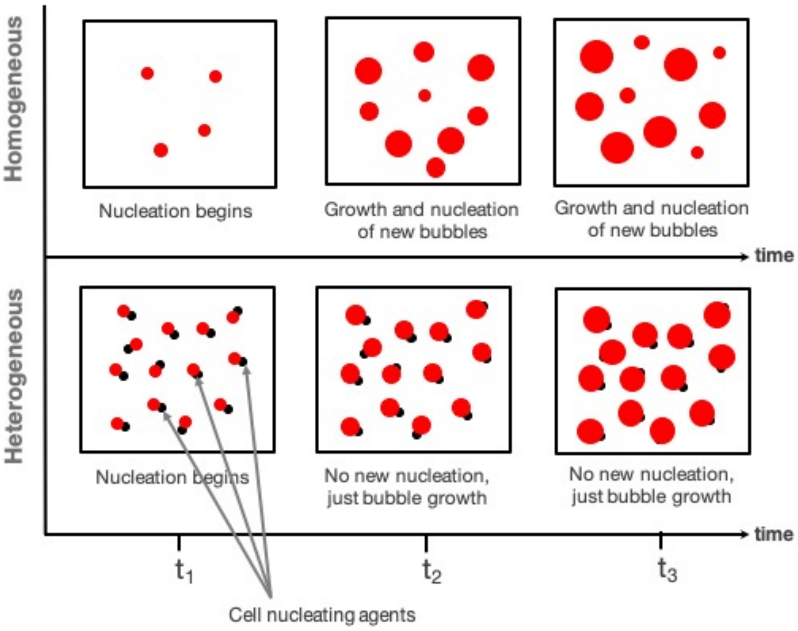

Figure 2.8: Modified schematic diagram [21] of homogenous and heterogeneous cell nucleation in polymer foams.

Classical heterogeneous cell nucleation

Unlike homogenous cell nucleation, heterogeneous nucleation does not occur spontaneously. It is triggered by the presence of heterogeneous particles such as fillers that consequently act as nucleation centres. The introduction of fillers of any kind[28] lowers the Gibb's free energy maximum but it largely depends on the filler type and topography; i.e. shape factor (*S*). Equation 2.10 shows the expressions for heterogeneous cell nucleation (ΔG^*_{Het}).

$$\Delta G^*_{Het} = \frac{16\,\pi\,\gamma^3_{\alpha\beta}}{3\Delta P^2} S(\theta_c) \tag{2.10}$$

---

[26] Is to the ratio of the specific free volume to the specific volume of a polymer.

[27] The frequency factor varies with the surface area of the nucleus.

[28] Assumed by the classical nucleation theory to be plate-like and with planer surface.

$$S(\theta_c) \ = \frac{1}{4}\left(2 + 3\cos(\theta_c) - \cos^3(\theta_c)\right) \tag{2.11}$$

The shape factor in equation 2.11 depends on the wetting or contact angle (θ_c) between the cell having a radius (R) and the surface of the filler. S will decrease as θ_c increases and this will lead to further reduction of ΔG^*_{Het}.

Considering that in reality some standard heterogeneous nucleating agents (NA) such as talc are not plate-like in geometry but particle-like, nucleation is assumed to occur in a conically-shaped pit as shown in Figure 2.7b; i.e. the preferred nucleation site will therefore be defined by the semi-conical angle (β) as shown in equation 2.12 [103]. The size of β will influence the work required to nucleate a cell.

$$S(\theta_c, \beta) \ = \frac{1}{4}\left[-2\sin(\theta_c - \beta) + \frac{\cos\theta_c \cos^2(\theta_c - \beta)}{\operatorname{Sin}\beta}\right] \tag{2.12}$$

2.3.2 Nanofillers as functional nucleation materials

Nanofillers are generally regarded as particles having at least one of its dimensions in nanometre length scale. Based on their dimensions, they are classified [104] into three major categories:

- Three-dimensional nanoparticles (3D). This include particles such as silica, carbon black (CB), titanium dioxide (TiO_2), etc., which have all dimensions in the nanometres as can be seen in Figure 2.9.
- Two-dimensional nanoparticles (2D) include platelet-like particles that have their thickness in nanometre and lateral dimensions between few hundreds of nanometres to a few micrometres. Examples of such particles include: graphite-based particles (functionalized graphene, expanded graphite), layered silicates (nanoclays), etc.
- One-dimensional nanoparticles (1D) comprise of particles such as carbon nanofibers (CNFs), carbon nanotubes (SWCNT, MWCNT), cellulose whiskers, etc. They have at least two of their dimensions in the nanometre range, thus they are all referred to as nanotubes.

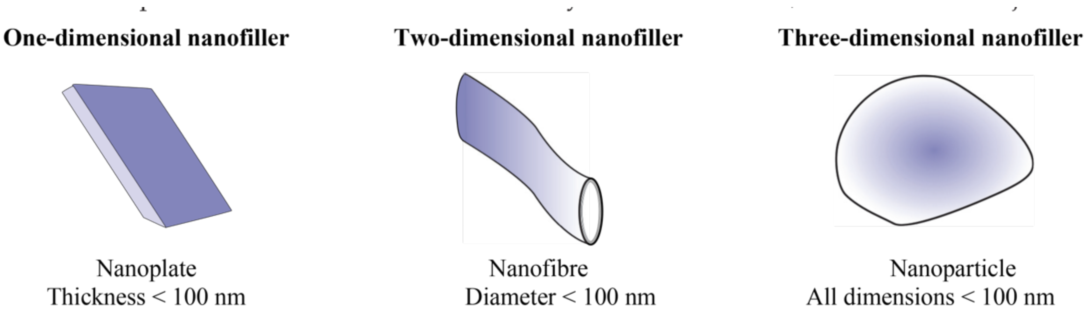

Figure 2.9: Categories of nanoparticles [105].

Basically, nanocomposites can be prepared either through solution casting, melt blending or *in-situ* polymerization techniques [105]. The properties of the nanocomposites depend greatly on the filler concentration and the dispersion quality of the fillers. Figure 2.10 illustrates the types of dispersion for clay-filled nanocomposites [105].

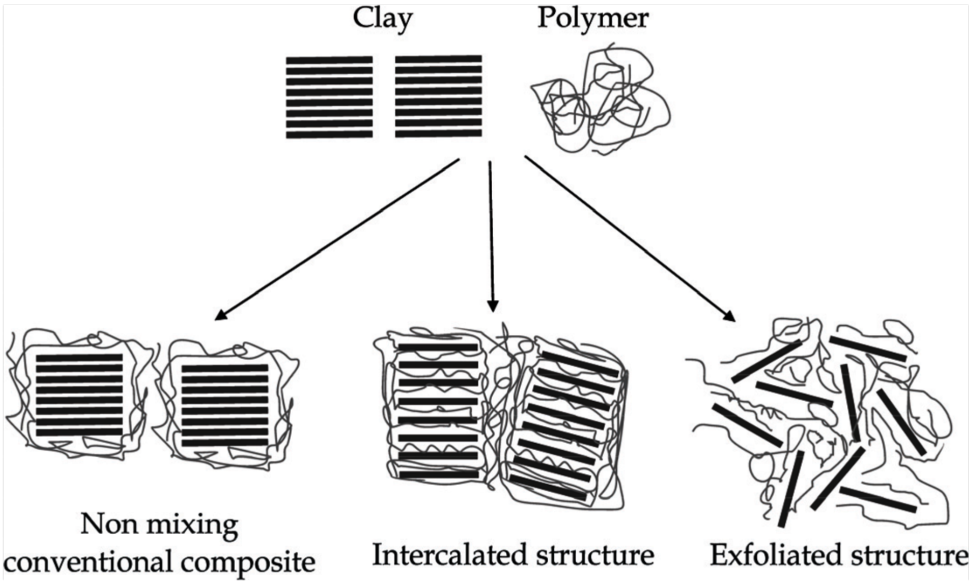

Figure 2.10: Schematic representation of clay platelet dispersion in a polymer matrix [105].

Zeng C. et al. [6] reported outstanding nucleation efficiency in PMMA nanocomposite foams when as little as 1 wt% of MWCNT was added as nucleating agent. In another foam extrusion study of PLA/clay nanocomposite foams, Keshtkar M. et al. [106] reported that a tremendous reduction of the cell size and increase of cell density and melt strength was achieved with good dispersion of 5 wt% of clay.
Also in another study, Zhang C. et al. [14] observed a decrease of the thermal conductivity of extruded PS nanocomposite foams with the addition of activated carbon particles.
Furthermore, it has also been demonstrated that nanoparticles led to significant improvements in mechanical [53], thermal [107] and electrical conducting properties [70,108] of polymeric foams. All these notable improvements show dependence not only on the size of the nanoparticles but on their dispersion quality[29]. In general, well-exfoliated fillers yielded the best results.
A list of assorted multifunctional, heterogeneous particles that have been used for the manufacture of polystyrene nanocomposite foams is given in Table 2.2 [12,13,23,82,109–130].

---

[29] Quality expressed in terms of degree of particle aggregation, agglomeration or exfoliation in the polymer martrix.

2.3.3 Significance of carbon-based nanofillers in polymer foam applications

Currently, specific attention is being given to the use of carbon-based nanofillers such as graphene, expanded graphite, carbon black, carbon nanotubes, carbon nanofibers etc. in various foam applications due to significant improvements in the thermal, electrical as well as flame-retardant properties achieved with the addition of little amount of such fillers [70,131–135].

Apart from thermal insulation applications, there are two other highly researched areas where carbon-based nanocomposite foams are in very high demand:

- in electromagnetic interference shielding (EMI) foam materials
- in halogen-free flame retardants (HFFR) foams

Electromagnetic interference shielding foam materials

For high EMI shielding efficiency (SE), good electrical conductivity of the nanocomposite foams is of paramount importance because the foam material should be able to absorb or reflect electromagnetic radiation. Electrically conductive carbon-based nanoparticles function very well as effective shielding materials because they are able to change the properties of microcellular foams from insulating to a semiconducting one. A target SE value of about 20 dB [136] is required for commercial purposes.

Zhang H. B et al [57]. reported a high electrical conductivity (3.11 S/m) of PMMA foams with very low amount of graphene (1.8 vol%) which is three times higher than the required target value (1 S/m) [137] for good EMI shielding properties. A corresponding EMI shielding efficiency of 13 -19 dB at 8 - 12 GHz was also achieved at same filler content (Figure 2.11).

Thomassin J. M et al [137]. achieved high shielding efficiencies between 60 dB to 80 dB with 0.25 vol % of MWCNT for PCL foams. Their results further show that the SE of the foams were three to four times higher than that of the PLC compact (unfoamed) material. In another similar study [138], an EMI SE of approximately 20 dB was realised with polyvinylidene fluoride (PVDF) nanocomposite foams reinforced with 5 wt% of functionalized graphene.

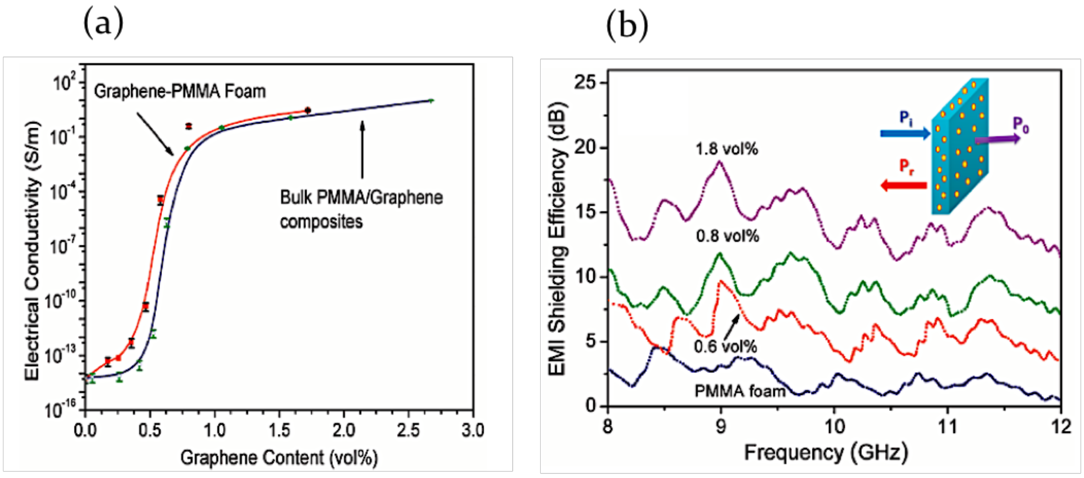

Figure 2.11: (a) Electrical conductivity of PMMA/Graphene nanocomposite versus PMMA/graphene nanocomposite foam (b) Electromagnetic shielding efficiency of microcellular PMMA/Graphene nanocomposite foam [57].

Halogen-free flame-retardant foams

Considerable improvements in the combustion behaviour of polymer foams have been achieved mostly with the use of Phosphorus-halogenated flame-retardants but the dense and toxic smoke caused by these compounds during combustion has led to their limited use especially due to environmental and health concerns [134,139]. Therefore, the development and use of intumescent[30] halogen-free flame retardants (HFFR) have become imperative.

Carbon-based fillers such as expanded graphite[31] (EG) is a perfect example of such intumescent halogen-free flame retardant that has been used and is still currently being used in many of these applications [134,139–141]. The flame-retardant mechanism of EG [142] is such that when heated to above 220 °C, the molecules of EG reacts with sulphuric acid to form gases (carbon dioxide, sulphur dioxide and water). This action causes the graphite layers to expand into a voluminous worm-like structure on the surface of the material that suffocates the flames, and the resulting char layer hinders heat penetration and diffusion of flammable volatile products towards the flame as well as diffusion of oxygen into the underlying material. Figure 2.12 [140] exemplifies the flame-retardant (self-extinguishing) behaviour of EG in semi-rigid polyurethane foam. The burnt layer (top-most layer) which appears almost degraded due to complete expansion and more exposure to the flame could hinder heat flux and oxygen diffusion. The surface layer is only partially degraded because the temperature there is not high enough to severely destroy the foam material. The inside layer remained intact due to complete protection from heat and oxygen.

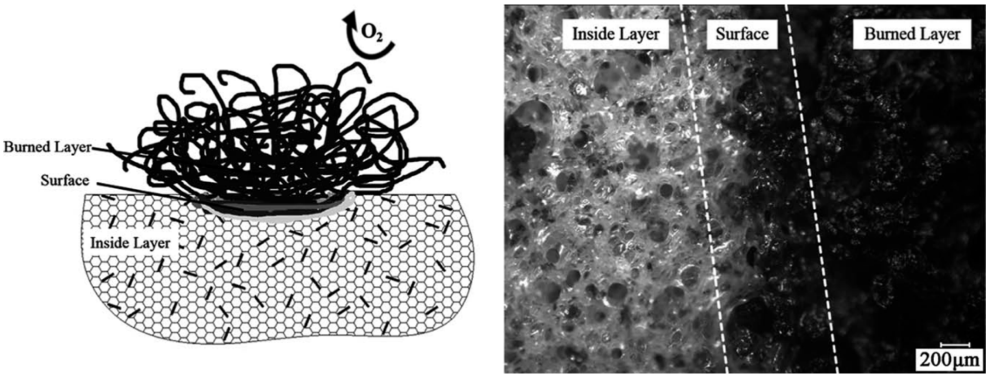

Figure 2.12: Flame-retardant behaviour of expanded graphite in semi-rigid polyurethane foam [140].

Tests such as limiting oxygen index (LOI)[32] and underwriter laboratory flame rating test[33] (UL 94) are generally used to evaluate the flame-retardant performance of polymer foam materials. When the LOI value of a material is less than 21 % it is classified as flammable because it will support an open

---

[30] An intumescent compound is one which during combustion generates in combination with other components, a charred barrier layer on the surface of the material that hinders heat penetration and diffusion of oxygen.

[31] EG is a graphite intercalated compound in which sulphuric acid has been inserted between the carbon layers.

[32] Standard test method for determining the minimum oxygen content required to support candle-like combustion of a plastic.

[33] This test method rates a material´s tendency to either extinguish or spread a flame once it has been ignited.

air burning situation; between 22 % and 25 %, the material self-extinguishes automatically and above 26 %, the material will have burning difficulties.

The vertical burning (UL 94-V) test requires a material to self-extinguish in order to pass the test. A *V-0* rating is regarded as the best, *V-1* rating as good and a *V-2* rating as drips (dripping of flaming material).

Table 2.2: Commonly-used nucleating agents for the production of PS nanocomposite foams [12,13,23,82,109–130].

Heterogeneous nucleating agents	
Acetylene black [a]	Graphite (natural or milled) [a,b]
Activated carbon (AC) [a]	Graphite oxide (GO)
Alkali lignin	Graphite nanoplatelets
Aluminium trihydroxide (ATH)	Magnesium hydroxide ($M_g(OH)_2$)
Azodicarboxylic acid diamide	Magnesium Oxide
Barium sulphate	Mica[a]
Black Iron oxide	Metal flakes
Boron nitride	Modified layered silicates (MMT, OMMT)
Calcium carbonate ($CaCO_3$)	Nanowhiskers (chitin, cellulose)
Carbon black[a,b]	Nanoclays (Cloisites)
Carbon nanotubes (CNT)T [a]	Pine (standard softwood)
Channel black[a]	Poly ethylene glycol (PEG)[c]
Carbon nanofibers (CNF) [a]	Powdered amorphous carbon[a]
Cellulose fibres	Silicates (calcium, sodium, lithium)
Ceramic microspheres	Silk fibroin powder
Chemically reduced graphite oxide (CRGO) [a,b]	Sodium bicarbonate ($NaHCO_3$)
Clay (organic and inorganic)	Sodium hydrogen tartrate (organic)
Crystalline silica (SiO_2)	Sodium and potassium hydrogen succinate (organic)
Diatomaceous earth (inorganic)	Spherical ordered mesoporous silica (s-OMS)
Ethyl lactate	Stearates (barium, calcium, sodium)
Ethylene methyl acrylate (EMA) [§]	Supramolecular compounds
Ethyl vinyl acetate (EVA)[c]	Talc[§]
Expandable thermoplastic microspheres (ETM)	Thermally reduced graphite oxide (TRGO) [a,b]
Expanded graphite (EG)	Titanium dioxide (TiO_2) [a,b]
Furnace black	Waste ground rubber tire powder
Flax fibres	Wood fibres
Glass fibres	Zeolites
Granulated asphalt[a]	

[a]: infrared attenuating agents (IAA), [c]: heat reflectors (HR), [c]: cell enlarging/anti-blocking agents (CE/ANBA). IAA, HR and CE/ANBA are materials that can be very useful in terms of decreasing the thermal conductivities of polymeric foams.

2.3.4 Effect of polymer-filler interaction on cell nucleation

The extent to which fillers bond to the polymer matrices determines their nucleation efficiency. Interestingly, the expectation that fillers with smaller dimensional sizes will lead to higher nucleation densities was found to be valid for particles with certain size limits [143,144].

In addition to particle size, the shape as well as topography of the particle surface also influence cell nucleation. For instance, a study by Fletcher N. H. [145] revealed that particles with flat surfaces offer better nucleation rates compared to tubular particles due to their curved edges. His arguments were, however, countered in another work by Chen L. et al. [146]. Goren K. et al. [56] concluded that there is competition between the number of nucleation sites and nucleation efficiency.

Leung S. N. et al. [147] studied the effect of wetting angle and the angle of conical cavity of a nucleating agent. They found that the difference $(\theta_c - \beta)$ determines the growth rate of a bubble. Both angles were observed to have affected the free energy in such a way that increasing θ led to a decrease of ΔG^*_{Het}, whereas the effect of β was dependent on θ_c. It was also shown that when $\theta_c \approx 90$ °, smaller β improved heterogeneous cell nucleation but when $\theta_c < 90$ °, heterogeneous cell nucleation is not favoured.

Conclusively, ideal nucleating agents for polymer foams should fulfil the following criteria [148]:

- They must not severely adhere to the polymer matrix[34].
- They should be homogeneously dispersible and adequately exfoliated within the polymer matrix.
- They must be present in sufficient quantity to foster the creation of more nucleation centres.
- The nucleants should be characterized by uniform size, shape and surface properties.

2.4 Role of blends in polymeric foams

Blending of polymers has become a beneficial and versatile means to produce novel multi-phase materials that are able to satisfy complex demands for high performance. It involves physical mixing of two or more chemically-distinct homopolymers, copolymers and /or terpolymers. The properties of the resulting polymer blends are a combination of the properties of the individual components. A blend may be miscible[35], partially miscible[36] or immiscible[37] depending on the properties of the components, composition ratio, interfacial characteristics, viscosity ratio, deformation[38] and disintegration phenomena as well as their methods of synthesis [62,149].

---

[34] This is equivalent to large wetting angle.

[35] Blends with single-phase morphological structures.

[36] Blends with either a single phase or two-phase morphological structures.

[37] Blends with multi-phase morphological structures.

[38] The relative displacement within a material measured by shear strain and resisted by elasticity.

2.4.1 Basic thermodynamics of blend miscibility

The miscibility of polymer blends depends on the value of Gibbs free energy of mixing (ΔG_m) as shown in equation 2.13 [150], where ΔH_m is the enthalpy of mixing[39] and ΔS_m is the entropy of mixing.

$$\Delta G_m = \Delta H_m - T\Delta S_m \tag{2.13}$$

Thermodynamically, binary blends will be miscible if the following conditions are fulfilled:

i. $\Delta G_m < 0$.
ii. The second derivative of the free energy with respect to the volume fraction of a component in the blend should be positive as given in equation 2.14.

$$\left(\partial^2 \Delta G_m / \partial \emptyset_i{}^2 \right)_{p,T} > 0 \tag{2.14}$$

where $\emptyset_i$ is the blend composition and it is taken as the volume fraction of one of the components. Figure 2.13 further illustrates the miscibility of binary blends based on the value of the Gibbs free energy of mixing as well as composition.

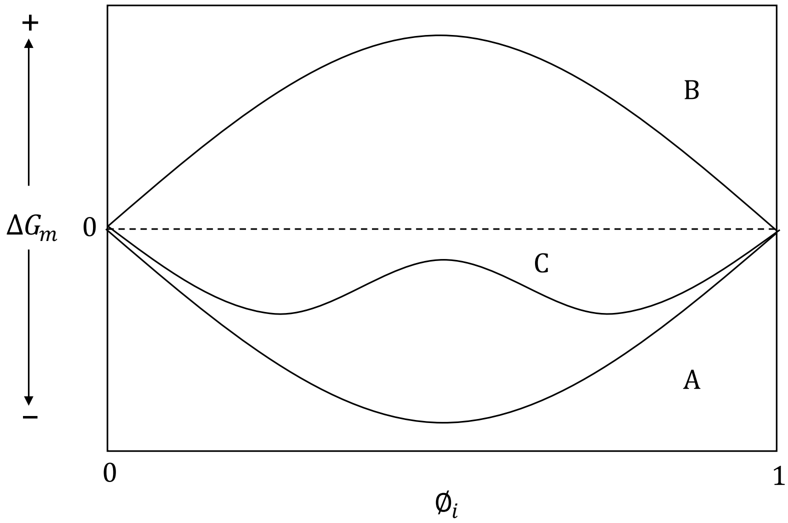

Figure 2.13: Gibbs free energy of mixing for binary blends as a function of their composition. Curve-A – represents total miscibility, curve-B – complete immiscibility, C- partial miscibility.

A blend represented by curve-A satisfies the aforementioned conditions i and ii for miscibility and is therefore miscible. Curve-B on the other hand has $\Delta G_m > 0$ and as such is completely immiscible irrespective of the blend composition. A blend system described by curve-C would be partially miscible because $\Delta G_m > 0$ and the second derivative of the Gibbs free energy of mixing is greater than zero. Miscibility can only be possible on the left and right composition areas of local minima of curve-C.

---

[39] The heat either generated during mixing (exothermic) or consumed (endothermic) during mixing.

2.4.2 Miscible polymer blends

Miscible blends are basically for investigating and refining polymer combinations [151]. The properties of miscible blends are affected by their chemical structure, molecular weight, combinatorial ratio and interfacial interactions of the pure components. However, with respect to foaming processabilities and foam properties, blends of this nature basically show additivity behaviour [152] with no known morphological characteristics.

2.4.3 Immiscible polymer blends

Immiscible blends are multi-phase systems that result in various interesting morphologies at the molecular level. These interesting morphologies illustrated in Figure 2.14. are dependent upon having control over the interfacial interactions. A sea-island morphology is that in which the minor component is the island (dispersed phase) and the major component is the sea (continuous phase). A co-continuous phase morphology results when both components are present at comparable concentrations and, as such, interpenetrate each other to form a network structure. The droplet-in-droplet[40] morphology is generated when the blending polymers are near the phase inversion region or by selective imposition of phase inversion and subsequent control of the time of mixing [153].

The microstructural changes that occur in immiscible binary blends having a sea-island morphology are governed by two dimensionless numbers, namely: the viscosity ratio (η_r) of the blend and capillary number (Ca). η_r is the ratio of the viscosity of the droplet phase (η_d) to the viscosity of the continuous phase (η_m), while Ca is the ratio between the deforming hydrodynamic stresses and the restoring interfacial stresses.

The expressions for these numbers are given in equations 2.15 and 2.16 [154] where $\dot{\gamma}$ is the shear rate[41], R_d is the radius of the droplet and α represents the interfacial tension. Comprehensive details on droplet deformation mechanisms and the thermodynamics of immiscible blends have been covered adequately in the work of Ruckdäschel H. [62] and Gutmann P. [155].

---

[40] Also known as composite droplet morphology or core shell structure or sub-inclusion or particle in particle morphology.

[41] The rate of change of shear strain (γ), i.e. the amount of deformation due to shearing.

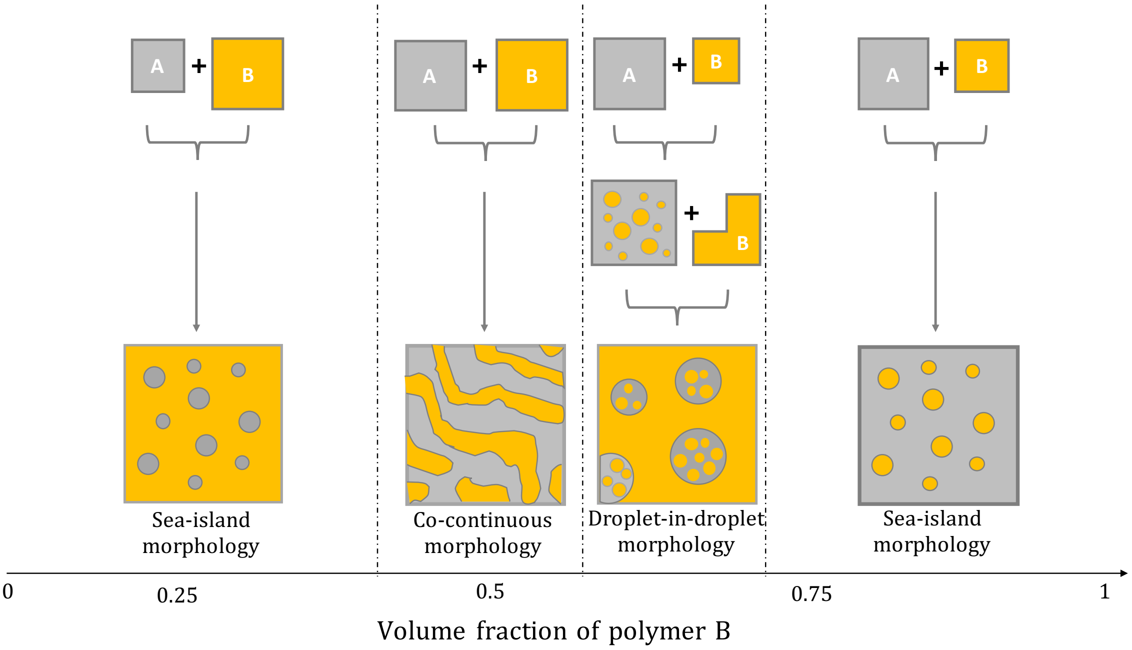

Figure 2.14. Typical phase morphologies of immiscible blends as a function of composition.

$$\eta_r = \eta_d/\eta_m \tag{2.15}$$

$$Ca = \eta_m\,\dot{\gamma}\,R_d/\alpha \tag{2.16}$$

Immiscible polymer blends have been employed in numerous foam studies since they offer several advantages like: increase of cell nucleation [156], enhancement[42] of the foamability of semi-crystalline polymers [157,158], increase of cell densities [157], improvement of melt strength to support cell expansion and growth [159], realization of nano-sized foams [154] and decrease of foam densities by use of CO_2-philic polymers [160] etc.

In conclusion, the focal point of these studies indicates that the final cell morphologies of immiscible foam blends are dependent upon the interfacial properties, which can be manipulated by the blend ratios and processing parameters.

2.5 Blowing agents for foaming

Blowing agents (BA) are substances that are capable of expanding to create the cellular structures required in polymeric foams. The quantity of blowing agent that is absorbed by polymer matrix influences properties such as the cell sizes, cell densities and, most importantly, the volume expansion ratios of the foams or foam densities. These blowing agents are classified into chemical blowing agents (CBA) and physical blowing agents (PBA) depending on the phase transitions[43] which they undergo.

---

[42] Decrease of crystallinity.

[43] Solid → gas or liquid → gas.

Some examples of blowing agents [12,13,23,82,109–130] used in foam processing are listed in Table 2.3 (for PBA) and Table 2.4 (for CBA).

2.5.1 Chemical blowing agents

CBA create the cellular structures in polymer foams by chemically reacting or decomposing either exothermically or endothermically under elevated processing conditions[44] to liberate gases that expand the foam. One of the most frequently used CBA is Azodicarbonamide (ADC) and it is exothermic in nature. Its decomposition at temperatures of 205 °C – 215 °C produces solid residues which remain in the foam plus gaseous mixtures of nitrogen (N_2), carbon monoxide (CO), carbon dioxide (CO_2) and ammonia (NH_3). N_2 makes up approximately 65 % of the total gas liberated from ADC. Bicarbonates of sodium and zinc are examples of the most frequently used endothermic CBA. The use of CBA does not give good control over porosity and they often result in foams having non-uniform cellular structures. Conclusively, in comparison to physical blowing agents, CBA have the advantage of being easier to incorporate into the polymer to be foamed via compounding but their low solubility, especially in thermoplastic materials, is a disadvantage.

2.5.2 Physical blowing agents

In contrast to CBA, PBA are generally gases that do not react chemically because of their inert nature. They result from physical processes such as evaporation or desorption at certain pressures and temperatures to liberate the desired gas.

In earlier times, Chlorofluorocarbons (CFCs) were typically the blowing agents of choice because of their ease of use. Their use was banned in 1987 by the Montreal Protocol due to stratospheric ozone depletion concerns [161]. As a result of this ban, partially-hydrogenated CFCs that have lower ozone depleting potential (ODP) were then used as temporary replacements [162] but were later phased out in 2010. As an alternative, volatile organic compounds (VOC) were also used but were strictly regulated due to their flammability issues. These restrictions necessitated the use of non-VOC and environmentally benign PBA which have zero-ODP. Nowadays, environmentally-friendly PBA such as CO_2, N_2 and water (H_2O) [30,53,87,163,164] are extensively in use either as mono- or co-BA.

---

[44] High temperatures.

Table 2.3: Commonly-used physical blowing agents for the production of polystyrene foams [12,13,23,82,109–130].

<table>
<tr><th colspan="2">Physical blowing agents</th></tr>
<tr><th>Halogenated hydrocarbons</th><th>Inorganic blowing agents</th></tr>
<tr><td>Chlorofluorocarbons (CFCs)</td><td>Carbon dioxide</td></tr>
<tr><td>Hydrochlorofluorocarbons (HCFCs)</td><td>Nitrogen</td></tr>
<tr><td>Hydrofluorocarbons (HFCs)</td><td>Water</td></tr>
<tr><td>Diffluoromethane, Trichlorofluoromethane</td><td>Argon</td></tr>
<tr><td>Dichlorofluoromethane,</td><td>Helium</td></tr>
<tr><td>Boron trifluoride</td><td>Xenon</td></tr>
<tr><td>Ethylchloride</td><td>Ammonium</td></tr>
<tr><td>Chlorotrifluoromethane</td><td></td></tr>
<tr><td>Methyl chloride</td><td></td></tr>
<tr><th>Aliphatic cyclohydrocarbons</th><th>Aliphatic alcohols</th></tr>
<tr><td>Cyclobutane</td><td>Ethanol</td></tr>
<tr><td>Cyclohexane</td><td>Methanol</td></tr>
<tr><td>Isobutane</td><td>Ethyl-hexanol</td></tr>
<tr><td>4-methylbenzene-1-sulfonohydrazide</td><td>Isopropanol</td></tr>
<tr><th>Ethers</th><th>Aliphatic hydrocarbons</th></tr>
<tr><td>Dimethyl ether</td><td>n-Pentane</td></tr>
<tr><td>Vinyl methyl ether</td><td>Isopentane</td></tr>
<tr><td></td><td>Methane</td></tr>
<tr><td></td><td>Ethane</td></tr>
<tr><th colspan="2">Ester</th></tr>
<tr><td colspan="2">Methyl formate</td></tr>
</table>

Table 2.4: Commonly-used chemical blowing agents for the production of polystyrene foams [12,13,23,82,109–130].

Chemical blowing agents
Azodicarbonamide (ADC)
Azobisisoibutyronitrile (AIBN)
Bicarbonates or carbonates
2-methacryloyloxyethylhy-hexadecyldimethyl Ammonium bromide (MHAB)
Sodium bicarbonate in combination with citric acid
Sulfonyl hydrazide

2.5.2.1 Supercritical fluids as blowing agents

Supercritical fluids (SCF) are gases that have been heated above their critical temperature (T_c) and compressed above their critical pressure (P_c) as shown in Figure 2.15. As a consequence, they exhibit intermediate properties between liquids and gases as shown in Table 2.5. SCF possess liquid-like densities, gas-like viscosities, diffusivities intermediate to that of liquid and gas and low surface tension. Although a number of substances such as nitrogen, water, ammonia, ethane, methane, etc. are useful examples of supercritical fluids, supercritical CO_2 has been the most widely used in processing polymeric foams [51,54,165–168].

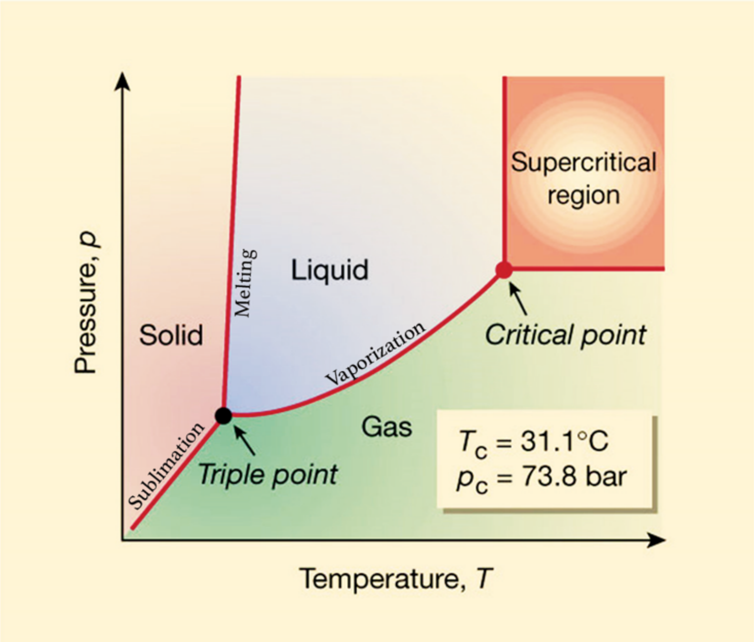

Figure 2.15: Phase diagram of supercritical fluids [169].

The non-flammable, non-toxic, chemically-inert nature of CO_2 as well as its availability at high purities and its low-cost place it as a top-notch PBA for processing of foams. Besides, the critical point of CO_2 (T_c: $31°C$, P_c: 7.38 MPa) [163] is easily accessed and allows it to be used at relatively low temperatures below 60 °C.

Table 2.5: Comparison of the properties of SCF with those of liquids and gases [170].

	Liquid	**SCF**	**Gas**
Density (kg/m^3)	0.6 – 1.6	0.1 - 1	10^{-3}
Viscosity (Pas)	10^{-3}	10^{-4} - 10^{-5}	10^{-5}
Diffusivity (cm^2/s)	10^{-5}	10^{-3} – 10^{-4}	10^{-1}

Another advantage of processing foams with supercritical fluids is the depression of T_g due to their high plasticization power effect[45]. This consequently allows for foams to be processed at lower temperatures that give the melt sufficient strength to sustain cell expansion. T_g depression has been found to be more pronounced in amorphous than in semi-crystalline polymers because, in the latter, crystallinity decreases gas solubility and diffusivity and also enhances viscosity [171].

Additionally, the high compressibility of such fluids enables their plasticizing power to be tuned and controlled by small changes in temperature and pressure. Examples of polymers where the T_g were depressed by supercritical CO_2 are listed in Table 2.6 [160].

Table 2.6: T_g of various polymers depressed by 8 wt% to 23 wt% of supercritical CO_2 [160].

Polymer matrix	**Bulk density (g/cm^3)**	**Initially measured T_g (°C)**	**Depressed T_g (°C)**
PS	1.05	103	48
PMMA	1.17	111	52
PS + SBM	1.01	98	39
PMMA + MAM	1.02	109	43
MAM	1.08	95	40
SBM	1.01	96	34

PS: polystyrene, PMMA: poly(methyl methacrylate), SBM: styrene-butadiene-methlymethacrylate.
MAM: methylmethacrylate-butylacrylate- methlymethacrylate.

The sorption experiments for these polymers were conducted at 40 °C for 16 hours using a pressure of 30 MPa. The quantity of CO_2 absorbed by the polymers was between 8 wt% to 23 wt%. It was further demonstrated in the same study that absorption of CO_2 decreased as the processing temperature was increased. This means that processing foams at lower temperatures are more likely to yield better results in terms of achieving smaller cell sizes, higher cell densities and high volume expansion ratios.

---

[45] The SCF molecules are able to act as diluents that causes chain segmental mobility to increase, thereby lowering the polymer T_g.

2.5.2.2 Solubility and diffusivity of blowing agents

For foams to be processed at relatively low temperatures, a sufficient amount of the blowing agent gas e.g. CO_2 has to be absorbed by the polymer. This quantity is dependent on the solubility limit which defines the maximum amount of gas that can be dissolved in the polymer either in the solid or melt state under a given pressure and temperature.

There are basically two methods used to estimate the total amount of CO_2 absorbed by a polymer specimen. The first method involves (i) saturating the polymer sample in a high-pressure autoclave, (ii) periodic but gradual depressurization of the autoclave at relatively low temperatures and (iii) removal of the specimen and measurement of its corresponding weight. This action is continued until no further change in weight is observed; meaning that the specimen is fully saturated with gas[46]. The mass uptake of CO_2 at any given time is then calculated using equation 2.17 [60,172], where $M_{gas\,t}$ is the gas concentration at time t, W_t is the mass of the specimen after time t and W_i is the initial mass of the sample.

$$M_{gas\,t} = \left(\frac{W_t - W_i}{W_i}\right) \times \, 100 \,\% \tag{2.17}$$

Figure 2.16a presents an example of this method using PMMA. It must be mentioned that the limitation of this method lies in the fact that it does not provide any data on the gas diffusivity of the system and does not estimate accurately the amount of gas absorbed by the sample.

Additionally, there is usually a slight loss of gas as the autoclave is depressurized inclusive of the time the sample is removed from the autoclave to be weighed. A more accurate method to make such an estimation is to use a magnetic suspension balance but it has a pressure limitation of about 25 MPa. Therefore, it cannot be used for very high gas pressure measurements.

The second method involves saturating the sample to equilibrium, removing the sample from the autoclave and subsequently measuring the weight loss of the sample at certain time intervals as CO_2 diffuses out. In order to obtain the equilibrium concentration (M_0) of CO_2 in the polymer specimen without any desorption, i.e. estimation of the total amount of CO_2 at time, t = 0, a plot of the amount of CO_2 absorbed by the polymer at time t (M_t) versus the square root of the desorption times recorded is made as illustrated in Figure 2.16b.

M_0 is obtained by fitting the desorption curve linearly and extrapolating to zero. Assuming that the sample thickness L (cm) remains unchanged, Fick's second law (equation 2.18) [173] can be applied and the diffusion coefficient D_d ($\mathrm{cm^2/min}$ or $\mathrm{cm^2/s}$) is obtained from the slope $((4/L)(D_d/\pi)^{1/2})$ of the curve.

$$M_t/M_0 = 4(D_d/\pi)^{1/2}(t^{1/2}/L) \tag{2.18}$$

---

[46] It can be said here that the polymer has attained its equilibrium gas concentration.

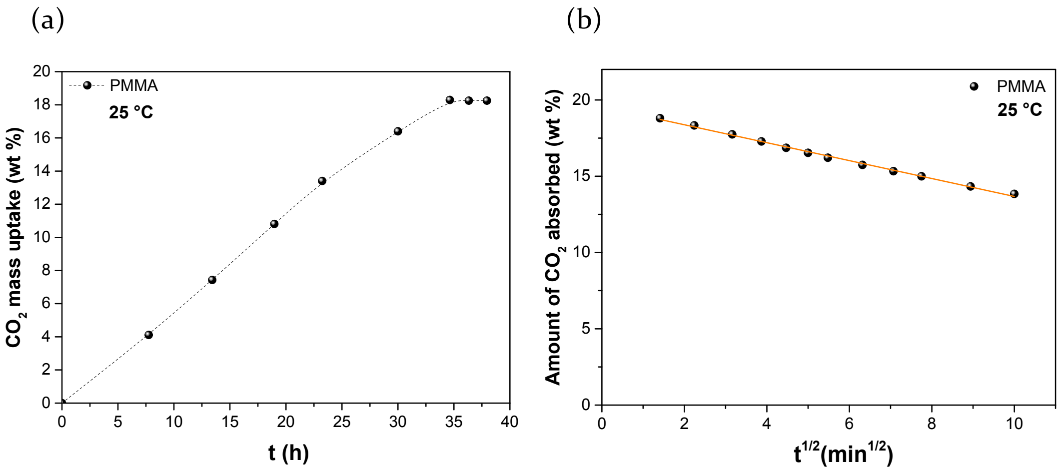

Figure 2.16: (a) CO_2 sorption curve (b) CO_2 desorption curve of poly(methyl methacrylate).

2.6 Role of rheology in foaming

Since the final foam microstructure is governed by the viscoelastic properties of the polymer matrix [174], it is important to perform rheological experiments to predict the foaming behaviour of polymers under deformational stresses. In foam extrusion, for example, the melt is subjected to two types of deformations, namely: shear and elongational deformations. Shear deformation occurs when the melt is subjected to the shearing actions of the screw in the barrel, while elongational or extensional deformation starts as soon as the melt exit the die and takes place for a very short period of between one and five seconds [88].

2.6.1 Shear Rheology

For large numbers of melt processing operations, shear deformation is essential because it provides information about the material structure and its flow characteristics [174,175]. It has been shown that the foam microstructure is strongly dependent on their shear rheological properties [176,177] and that enhanced cell morphologies were achieved for matrices with higher complex viscosities (η^*) and storage modulus (G') [178,179].

Furthermore, when polymer materials are filled with nanoparticles, additional information such as particle-particle interactions or particle-matrix interactions can be obtained from the η^*, $G'$and phase angle ($tan\ (\delta)$) data. The relationship between the complex shear viscosity and storage and loss moduli (G'') is given in equation 2.19, where ω is the angular frequency.

$$|\eta^*| = \frac{1}{\omega}\sqrt{G'^2 + G''^2} \qquad 2.19$$

Oscillating rheometers, capillary rheometers, etc. are examples of laboratory devices that can be used to obtain shear viscosity data.

2.6.1.1 Van Gurp-Palmen plot for linear and branched polymers

In 1998 [180], Van Gurp and Palmen presented what is today known as the van Gurp-Palmen plot (vGP-plot) as a rheological method to verify the time temperature superposition principle (TTS). For this, a plot of the phase angle ($\delta = \tan^{-1}$ (G'/G") is plotted against the corresponding absolute value of the complex shear modulus (|G*|). Using this approach, Tinkle S. et al. [180], discovered that more shear rheological information due to the effect of molecular weight, polydispersity, chain branching and multiple (main chain and side chain) relaxation processes [181] could be obtained from such plots. In addition, information about structural composition in relation to filler dispersion can be obtained from a vGP plot.

For linear polymers, the shape of the vGP-curve is sensitive to the chemical composition, molecular weight, molecular weight distribution and tacticity [180]. Furthermore, the shape of the curve reveals excellent information about the plateau modulus (G_N^0)[47], entanglement molecular weight (M_e) of polymers, miscibility of blends [182] etc. of linear or branched chain polymers. For example, linear polymers generally exhibit a characteristic curve like those shown for polystyrene in Figure 2.17a [180] where the the δ value decreases as the molecular weight of the polymer increases. The influence of difference in polydispersities (M_w/M_n) of some selected poly(olefin)s is presented in a reduced van Gurp-Palmen plot (rvGP-plot)[48] in Figure 2.17b. Regardless of chemical structure and tacticity, all rvGP- curves of polymers with the same polydispersity will superimpose on one another [180].

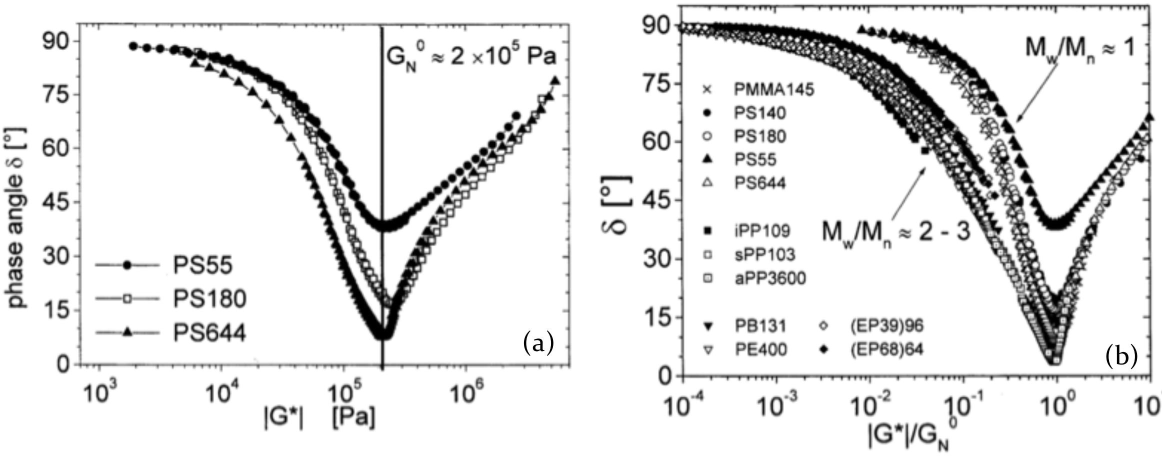

Figure 2.17: (a) Van Gurp-Palmen plots of three polystyrene samples with different molecular weight (b) reduced vGP-plots of thermoplastic polymers having different chemical composition and polydispersities [180].

Miao H. [182], employed vGP-plot to determine the plateau modulus (G_N^0) of linear and cyclic polyoctenamer (PCO). They found out that the (G_N^0) of cyclic PCOs were lower than that of linear PCOs as shown in Figure 2.18.

---

[47] The corresponding absolute value of complex modulus (|G*|) at tan (δ) minimum.

[48] The rvG-Plot is obtained by plotting the phase angle (δ) versus (|G*|)/(G_N^0)

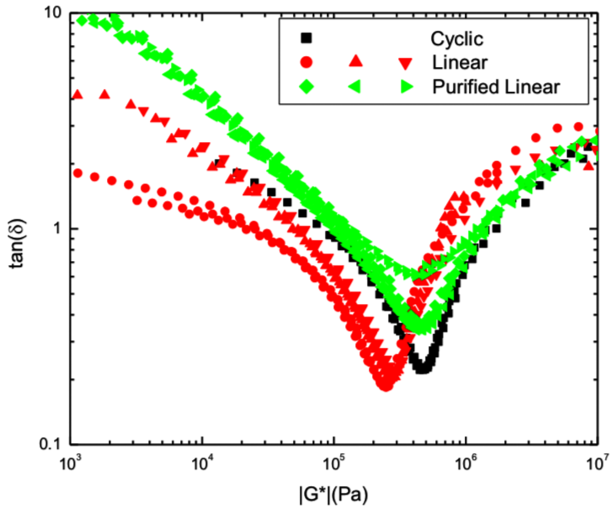

Figure 2.18: Van Gurp-Palmen plots of linear and cyclic polyoctenamer at a reference temperature of 40 °C [182].

Furthermore, vGP-plot was used by Hao X. [183] to confirm the miscibility of PLA/PMMA blends. They observed negligible deviation in comparison to the curve of neat PMMA. The superimposition of the blend curves irrespective of experimental temperature, indicated that the blends are thermorheologically simple. i.e. the various relaxation times exhibit similar temperature dependence [183].

Also, the liquid–solid transformation of filled polymer nanocomposites can be determined from vGP-plots [184,185]. An example of such transformation is shown with the shear rheological data of PLA/GNP nanocomposites in Figure 2.19. The liquid-like behaviour is indicated by δ-|G*| = 90° ($\lim_{G*\to 0} \delta = 90°$) whereas in a solid-like behaviour δ-|G*| curve approaches 0° at low absolute complex modulus [185]. The filler content beyond which the liquid-like behaviour is changed into a solid-like behaviour is referred to as the rheological percolation threshold [185].

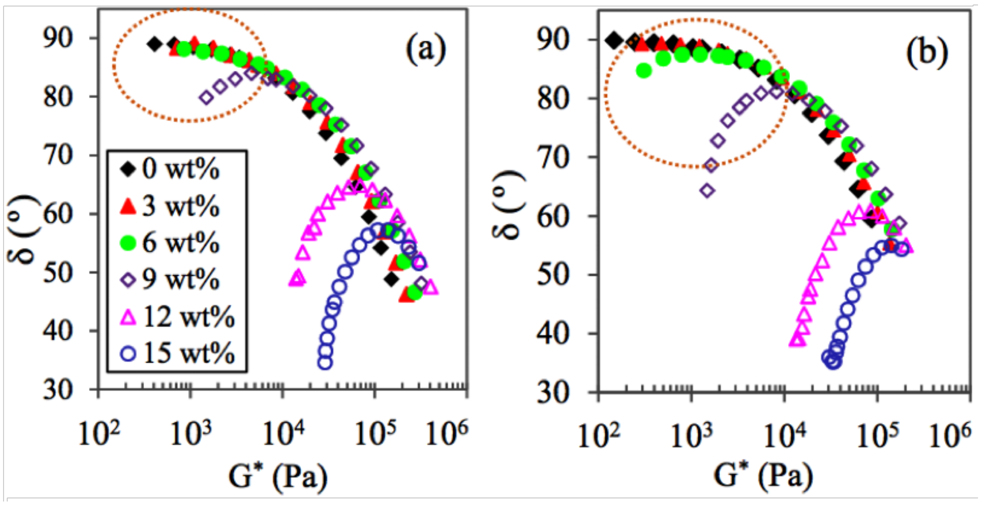

Figure 2.19: Van Gurp-Palmen plots of PLA/GNP[49] nanocomposites at (a) 180 °C (b) 200 °C [185].

---

[49] GNP: Graphene nanoplatelets

2.6.2 Elongational rheology

Elongational rheological characterization on the other hand is also vital as information about melt strength which relates to cell expansion and growth can be obtained. There are three types of elongational flow, namely: uniaxial[50], biaxial[51] and planer[52]. Biaxial elongation is the major deformation mode in polymer foaming processes but experimental complexities and the non-availability of reliable techniques makes it difficult to accurately carry out these studies [1]. Elongational properties can be calculated from shear data when the deformation is small, but when the deformation is large – i.e. outside the linear viscoelastic region – extensional properties cannot be predicted from shear data. Still, in order to compare elongational and shear data outside the linear regime, the Trouton law which relates elongational uniaxial viscosity (η_{uE}) to shear viscosity (η_s) was introduced [1] and it is given in equation 2.20. The expressions for biaxial and planer viscosities in relation to shear viscosity are also given in equations 2.21 and 2.22, respectively.

$$\eta_{uE} = 3\eta_s \qquad 2.20$$

$$\eta_B = 6\eta_s \qquad 2.21$$

$$\eta_P = 4\eta_s \qquad 2.22$$

Elongational rheological experiments are primarily done to select the optimum matrix candidate to be foamed. These experiments are basically performed for in processes such as blow-film extrusion, injection blow moulding etc. where biaxial stretching of the polymer melt is encountered. In order to have comparable results, it is important to investigate polymers that have the same processing history. In particular, polymers with very low-melt strength that do not exhibit strain hardening under extensional flow [85] are mostly appropriate for this purpose.

Polymers with such characteristics, when foamed, develop thinner cell walls during cell expansion and; when this happens, cell coalescence and even cell rupture occur. Examples of such polymers with foamability challenges are: polypropylene (PP), low-density polyethylene (LDPE), polylactic acid (PLA) etc. Despite these challenges, chain branching, blending, control of the processing temperatures and adjustment of molecular weight and molecular weight distributions [86,88,149,186–190] are some of the methods that have been used to enhance the melt strength and strain hardening properties of these polymers.

Furthermore, for illustrative purposes, the extensional deformation behaviour for two high melt strength polypropylenes (HMS-PP) having different thermo-mechanical history is shown in Figure

---

[50] Elongation in only the z-direction with corresponding contraction in the x and y-directions.

[51] Elongation in z- and x-directions with corresponding contraction in the y-direction.

[52] Elongation in z-direction, contraction in the y-direction and no elongation or contraction in the x-direction.

2.20 [191]. Strain hardening (SH) behaviour[53] can be seen for both samples and this is important for selecting the polymers to be foamed. SH is seen as a form of enhanced viscosity that is needed to help prevent cell coalescence and rupture during growth and expansion [88]. Besides, strain hardening is barely observable for biaxial extension [1].

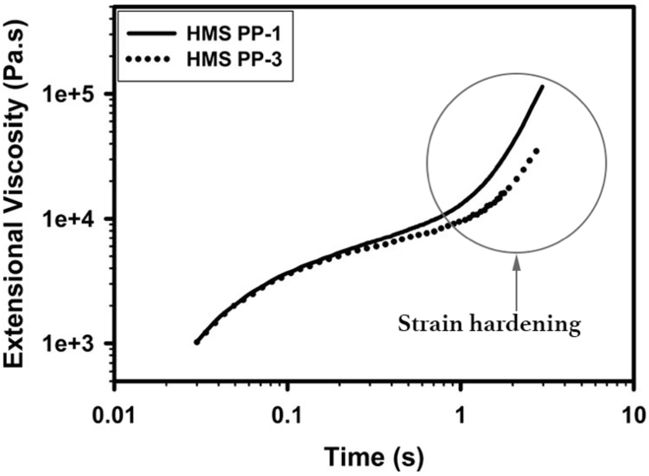

Figure 2.20: Elongational rheological behaviour of pure HMS-PP after one and three extrusion cycles [191].

Semi-crystalline polymers such as those mentioned earlier are mostly associated with low melt strength and strain hardening problems unlike amorphous polymers that exhibit better melt strength properties.

High molecular weight PS ($M_w > 150{,}000$ g/mol) [192], which is an example of an amorphous polymer, is able to form a strong entangled polymer network that leads to higher viscosity and melt strength at normal processing temperatures (190 °C to 230 °C). Additionally, its benzene ring side chain favours the formation of higher entanglement density at even higher temperatures.

Elongational measurements can be executed using Münstedt rheometer, Meissner rheometer, Rheotens extensional device etc. Procedural details of the aforesaid measuring devices can be found elsewhere [193,194]. Elongational viscosity values can also be obtained using contact-free optical methods such as Laser-Doppler anemometry (LDA) [195][196].

---

[53] Strain hardening is known as extensional thickening and is related to the rapid increase of a polymer viscosity at large strains.

2.7 Foam processing technologies

Since the focus of this work is to manufacture microcellular and nanocellular low-density closed-cell foams for thermal insulation purposes, this section will concentrate on briefly reviewing the two most extensively used foam-processing methods, namely: batch foaming and foam extrusion. The basic similarities and differences between both methods are summarized in Table 2.7.

2.7.1 Stages of the foaming process

Fundamentally, the principles of foaming are the same for the three aforesaid processing methods and the stages involved are:

- **Saturation**: the polymer is saturated with a physical blowing agent at sufficiently high pressures and defined temperatures. This of course depends on the T_g for amorphous polymers and T_m for semi-crystalline polymers.
- **Nucleation**: thermodynamic instability, i.e. pressure drop (ΔP) is introduced into the supersaturated polymer-gas mixture either by a sudden increase of temperature or a rapid decrease of pressure. At this point, phase separation of the mixture occurs, prompting cell nucleation due to decrease of gas solubility.
- **Cell growth**: growth evolves as gas diffuses into the stable nuclei. The growth rate of the successfully nucleated cells is controlled by (a) the gas diffusion rate, (b) the viscoelastic behaviour of the polymer at that temperature and (c) state of supersaturation, etc.
- **Stabilization**: cell growth is impinged by rapid cooling of the resultant foam either by water, non-reactive solvents or by air. Consequently, the cellular structure is solidified and a stabilized[54] microstructure is formed.

2.7.2 Batch-foaming process

Batch foaming, as the name implies, is a batch-wise process typically conducted in an autoclave. It involves the aforementioned sequential foaming stages which can be performed in either one-step[55] or in two-steps[56]. If a one-step procedure is observed, it is referred to as the pressure-quench method or pressure-induced method and, if a two-step process is followed, it is referred to as the temperature-induced method.

The specimens for batch-foaming experiments are usually in the form of a circular disc, rectangular or square-shaped compact materials. The thickness of such specimens is usually between 0.5 mm and 3 mm and it is a very important dimensional factor because information about gas diffusivity can be extracted.

---

[54] The stabilization of the cell structure depends on the melt-strength and cell growth stresses.

[55] All the stages of foaming are observed at once in an autoclave without any transfer of the sample.

[56] The specimen saturation stage is carried out in one-step and in another step, the inducement of cell nucleation, growth and stabilization are performed in a separate second-step.

Pressure-induced batch foaming (a one-step process)

In the pressure-induced method presented schematically in Figure 2.21, the specimen is saturated at a specified pressure in the autoclave with a physical blowing agent. After the equilibrium saturation time has been reached, cell nucleation and growth are induced by rapid depressurization of the autoclave to atmospheric pressure. Afterwards, the final cell microstructure is fixed. Unlike in the two-step method (temperature-induced batch foaming), the saturation process usually takes place at higher temperatures.

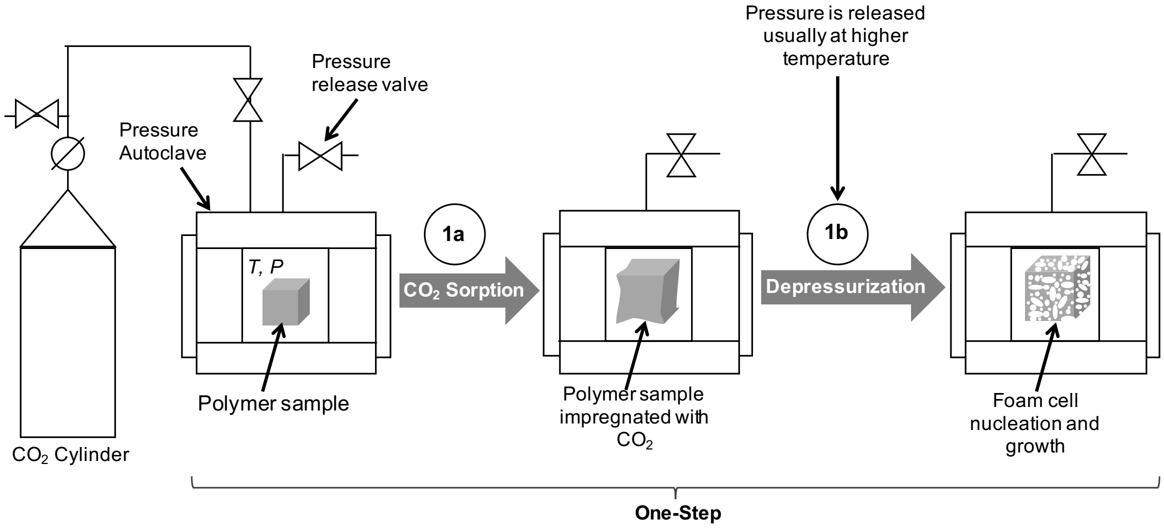

Figure 2.21: Pressure-induced $(\Delta P/\Delta t)$batch-foaming process

Temperature-induced batch foaming (a two-step process)

In contrast to the pressure-induced method, saturation here is usually conducted at moderately low temperatures. After the equilibrium saturation time has been achieved, the specimen is taken out of the autoclave as shown in Figure 2.22. Thermodynamic instability is introduced by dipping the supersaturated specimen into an already prepared hot oil bath set at a fixed temperature of choice (usually between 80 °C and 150 °C) for a specific time period (typically between 1 sec and 600 sec). Cell nucleation is induced and growth continues. The sample is taken out of the oil bath and immersed in a cooling bath filled with water or a mixture of other solvents.

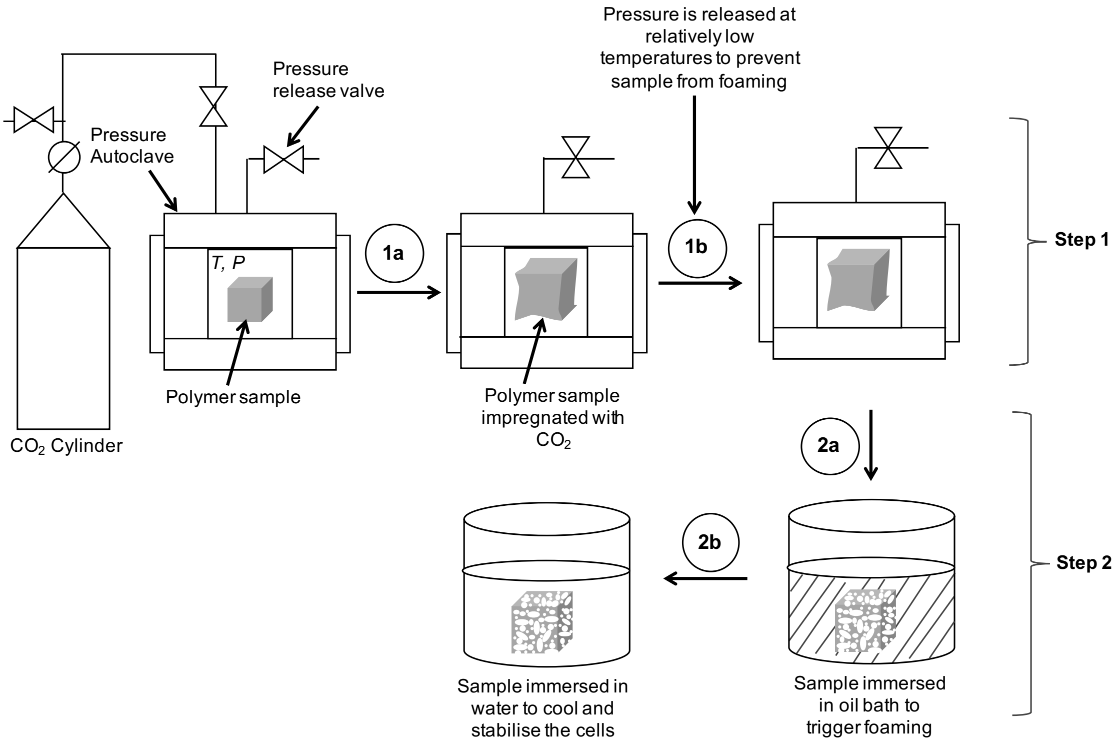

Figure 2.22: Temperature-induced $(\Delta T/\Delta t)$ batch-foaming process.

2.7.3 Foam extrusion

Foam extrusion is a continuous process which consists of an extruding unit and die-shaping unit. It follows the same principle as the conventional plastic extrusion process with the slight difference of blowing agent introduction at a certain point on the extrusion line as illustrated in Figure 2.23. Most foam extrusion lines used industrially are tandem lines as opposed to single lines because (i) they offer higher output rate and (ii) the problem of screw snap caused by temperature differential as a result of heating and cooling different zones of the screw in single lines does not occur. This is because tandem lines have one barrel specifically for melting and the other for cooling. However, single lines are still in use for sensitive polymeric materials, e.g. polylactic acid (PLA), that require shorter residence time [190].

Polymers in pellet form are introduced into the first barrel (melt-extruder) through the feed hopper. The pellets are then melted under high pressure at relatively high temperatures. Via an injecting unit located on the barrel, PBA such as CO_2 in supercritical condition is injected into the melt and a one-phase homogenous system is formed from a two-phase system (polymer-gas) due to the high pressure in the barrel. CBA can also be used but it must be fed together with the pellets. Under certain temperatures and pressures, the CBA decomposes to liberate the required gas into the melt.

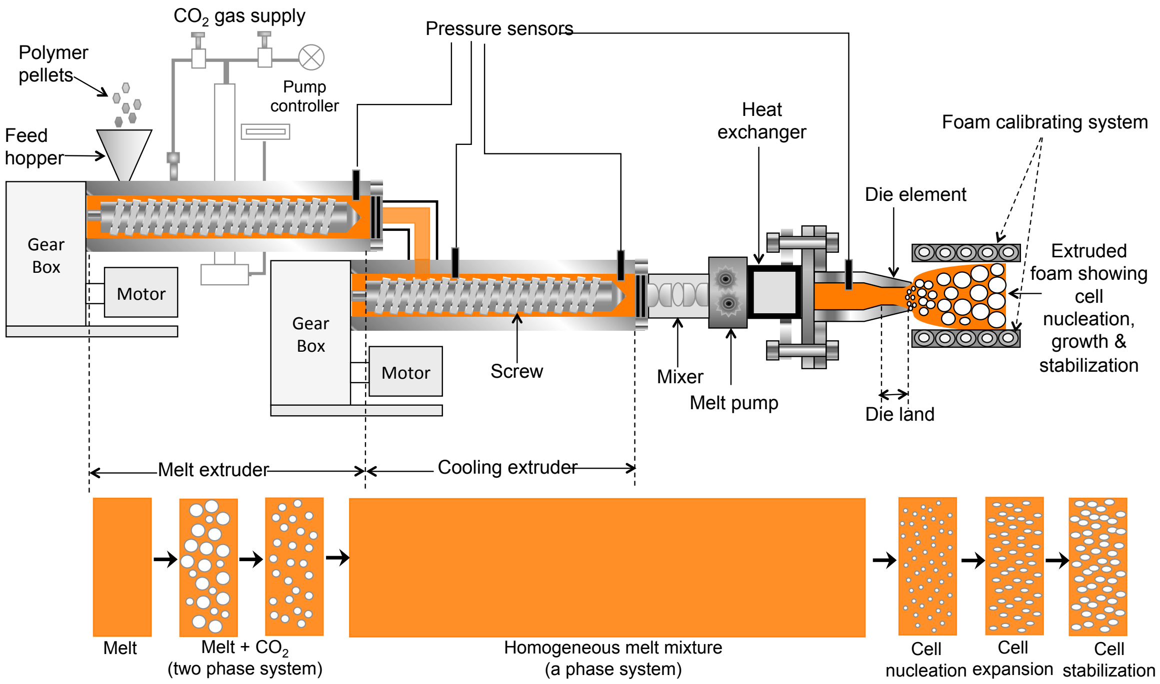

Figure 2.23: Schematic diagram of foam extrusion on tandem-line.

The gas-loaded melt is advanced into the second barrel by the motion of the screw. Here, the melt is slightly cooled to a temperature lower than in the first extruder but temperature is remaining high enough to provide good mixing. Nucleation is suppressed due to high pressure encountered in the barrel. The melt-pump controls the polymer melt flow rate, independent of the temperature and pressure changes. The heat exchanger provides further cooling for the polymer melt to suppress cell coalescence. As the polymer-gas melt leaves the extruder through the die, foam cells are nucleated by a rapid pressure drop generated as the mixture exits the die. The cells keep growing until vitrification occurs. It is important to note that cell nucleation can occur either in the die or after the die as shown in Figure 2.24. In most cases, the final part of the foam extrusion process consists of calibration and cutting of the extruded foams.

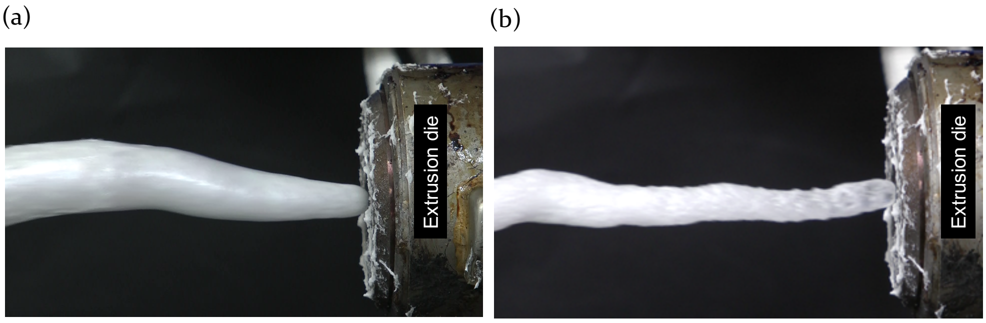

Figure 2.24: Cell nucleation (a) occurring inside the die, (b) occurring outside of the die.

Table 2.7: Comparison between batch-foaming and foam extrusion processing technologies [1,30,53,165].

Basis for comparison	**Batch foaming**	**Foam extrusion**
Process type	Batch-wise	Continuous
Purpose	Fundamental foam studies of new materials	For economically feasible and large-scale foam production
Material amount required	Small amount (in grams)	Large amount is needed (usually in kilograms).
Pre-moulding step	Pre-moulding step such as injection moulding, compression moulding or casting is normally done to mould the species into the required geometry	Not required, as it is a moulding tool in itself
Screw type	No screw	Long-single or double (usually co-rotating) screws.
Addition of nucleating agents/ process flexibility	Foam composition is fixed from the onset. Must be done in the pre-moulding step using either injection moulding or extrusion, etc.	Composition can be changed at any time. i.e. nucleating agents can be introduced at any time during processing
Filler dispersion/mixing quality	Determined from the result of the pre-moulding step	Better mixing quality compared to foam injection moulding.
Sample state during gas loading/ saturation temperature	Solid-state. Done conventionally below T_g for amorphous polymers and above T_m for semi-crystalline polymers	Melt state. Metered above T_g for amorphous polymers and above T_m for semi-crystalline polymers
Blowing agent supply	Polymer sample is saturated with the blowing agent until equilibrium is reached	Blowing agent is metered (i.e. a specific amount of gas is supplied) but not more than the melt can take
Blowing agent uptake	Moderate to high	Low to high
Maximum achievable pressure	Up to 400 bar (40 MPa) [45–74]	Up to 250 bar (25 MPa) [5,13,44,80–98].
Temperature adjustment and control	Experimental temperature is fixed but can be changed from one level to another. This method offers only one temperature zone	Offers more opportunities to use different temperatures due to the availability of different zones
Driving force for nucleation	Pressure drop or change in temperature	Pressure drop
Shear impact on polymer	No shear, therefore sensitive materials can be processed	High shear
Cell density range	10^6 - 10^{16} cells/cm^3	10^4 - 10^{11} cells/cm^3
Cell size distribution	Uniform cell size distribution can be achieved	Although uniform cell size distribution can be achieved, sometimes the diameter of the cells found at the core are different from those found at the edges. This might be due to variations in cooling between the foam surfaces and the core

Basis for comparison	Batch foaming	Foam extrusion
Foam density reduction achievable	Up to 85 %	Up to 80 %
Volume expansion ratio	moderate to high expansion	Low to very high expansion
Surface quality	Good	Good and often glossy
Foam skin	Light skin	Light skinned foams
Size of foam parts that can be produced	Small parts that can be used to make some very basic measurements	Simple but large parts such as foam slabs.
Shaping element/flexibility	Foams take the shape of the preformed sample but are often irregular.	The geometry of the die determines the shape of the part. Foams exiting the die can be calibrated. Allows for more flexibility of changing dies
Total experimental time required to obtain a foam sample	Varies from 30 minutes to 72 hours depending on polymer type and sample thickness	Shorter times (2-15 minutes)
Foaming of multiple specimens	Possible with many sample holders in the pressure autoclave	Limited/not possible
Tooling cost	Relatively cheap compared to the other two methods.	Expensive depending on machine capacity. Additional cost is incurred from other peripherals like melt pump, calibrator, etc.

2.8 Polymeric foam characterization and classification

2.8.1 Foam structure characterization

The features of polymeric foams are characterized by the following terms:

Foam density

The density of foams (ρ_f) is usually evaluated by a density kit based on the water-displacement method of Archimedes' principle. The expression in equation 2.23 shows how the foam density is calculated. X represents the mass of the sample in air and Y is the mass of the sample in water.

$$\rho_f = \frac{X}{X-Y} \tag{2.23}$$

Foam relative density

The relative density (ρ_{rel}) of a foam is the ρ_f divided by the density of the unfoamed or solid polymer ($\rho_{polymer}$). It is the inverse of the volume foam expansion ratio as shown in equation 2.24.

$$\rho_{rel} = \frac{\rho_f}{\rho_{polymer}} = \frac{1}{VER} \tag{2.24}$$

Cell density

Cell density (ρ_{cell}) signifies the number of cells per unit volume with respect to either the foamed polymer (equation 2.25) or with respect to the unfoamed solid polymer (equation 2.26), where n is the number of cells selected for evaluation, A is the total area occupied by the selected cells, and M is the magnification factor of the microscope. V_f stands for the void fraction of the foam in equation 2.27.

$$\rho_{cell} = (nM^2/A)^{\frac{3}{2}} \tag{2.25}$$

$$\rho_{cell} = (nM^2/A)^{\frac{3}{2}}\left(1/1 - V_f\right) \tag{2.26}$$

$$V_f = 1 - \left(\frac{\rho_f}{\rho_{polymer}}\right) \tag{2.27}$$

Further information about the purposes of the respective equations serve is given in greater detail elsewhere [197,198].

Cell size

The mean cell size (ϕ_m) is usually the average value of all cell sizes estimated by examining a reasonable number (usually three) of scanning electron micrographs. The cell size distribution is also another important characteristic to consider because it indicates the homogeneity level of the foam cell morphology. It is calculated according to equation 2.28 [199] by assuming the cells to be spherical in shape.

$$\phi_m = \left[\frac{1}{\rho_{cell}} \times \frac{6}{\pi} \times (1 - \frac{\rho_f}{\rho_{polymer}})\right]^{1/3} \tag{2.28}$$

Nucleation density

The nucleation density (ρ_{nucl}) gives an indication of the nucleation efficiency of the nucleating agents especially by assuming the absence of cell coalescence. It is expressed in equation 2.29 [199,200] as the number of nuclei or nucleated cells per cubic centimetre of the unfoamed polymer. This calculation is also based on the assumption that the cells are spherical.

$$\rho_{nucl} = \frac{\rho_{cell}}{1 - V_f} = \frac{\rho_{cell}}{\rho_{rel}} \tag{2.29}$$

Nucleation efficiency

The efficiency of the nucleants (N_{Nul}) can be estimated from equation 2.30 [201], where w_p is the weight fraction of the nucleating particle in the polymer composite, ρ_p and $\rho_{polymer}$ are the densities of the nucleating particles and the polymer, respectively, and V_p is the volume of an individual nucleating particle.

$$N_{Nul} = \frac{Nucleants}{cm^3} = \frac{w_p}{\rho_p} \times \frac{\rho_{polymer}}{V_p} \tag{2.30}$$

2.8.2 Classification of polymeric foams

Polymeric foams are commonly classified according to their cellularity, wall stiffness, volume expansion ratios and mean cell sizes.

Cellular structure

This refers to connectivity of cells within the foam. When the cells are interconnected[57], they are referred to as having an open-cell structure. But if the cells exist as separate discrete entities, they are described as having a closed-cellular structure.

Wall stiffness

Foams with cell walls that collapse when pressed are said to be flexible while those with relatively stiff cell walls are referred to as rigid foams.

Volume expansion ratio

Volume expansion ratio refers to the ratio of the bulk density of the pure or compact polymer material to the bulk density of the foamed polymer material. Based on this definition, foams are categorised as:

- High-density foams: VER ≤ 4.
- Medium-density foams: VER > 4 – 9.
- Low-density foams: VER ≥ 10 – 50.

Size of foam cells

Polymeric foams are classified nowadays as macrocellular, fine-cell, microcellular and nanocellular based on the following criteria:

- Macrocellular: cell size ≥ 100 µm
- Fine-cell: cell size ≥ 11-100 µm
- Microcellular: cell size ≤ 1-10 µm
- Nanocellular: cell size ≤ 1 µm

It is important to mention that the aforesaid classification unfortunately does not take into account the foam densities; a property which is considered one of the most important properties of polymeric foams.

---

[57] Connection of cells through holes.

3 Motivation, aims and strategies

3.1 Motivation

About 40 % of the energy generated in the EU is consumed by commercial and domestic buildings [17]. Concerns over enhanced energy efficiency in buildings coupled with rising energy prices have triggered demand for high performance thermal insulation materials. One of the key ways to decrease energy consumption has been the use of polymeric microcellular closed-cell. To achieve a low thermal conductivity (less than 34 mW/mK), low density foams (less than 64 kg/m^3) [44] foams are required. The current trends in microcellular and nanocellular foam production, involves the use of mostly carbon-based nano-sized nucleating agents. Some of these nucleating agents have infrared radiation absorption and reflection capabilities [21,22], that enable the reduction of the overall thermal conductivity by decreasing the thermal radiative contributing component.

The conventional methods for preparing microcellular and nanocellular nanocomposite foams are via batch-foaming and foam extrusion techniques using CO_2 as the blowing agent.

Literature survey on microcellular (cell size ≤ 10 µm) low-density (*VER* ≥ 10) closed-cell foams manufactured either through a batch foam process [45,46,50,54,71,202–204] or via foam extrusion [13,14,87,110,127,205], revealed that polystyrene (PS) and poly(methyl methacrylate) (PMMA) were the most frequently used polymer matrices to fabricate these foams. Analysis of the data which is presented in Figure 3.1 showed that low-density foams[58] could be generated with PS while foams with cell sizes less than 10 µm were generated with PMMA.

Astonishingly, it can be seen that microcellular low-density foams have so far not been successfully fabricated using either PS or PMMA [31,53,54,56,57,70,72,206]. This is indicated by the target area marked with a blue rectangular box in Figure 3.1.

Therefore, the focus of this work is to prepare microcellular low-density nanocomposite foams of PS, PMMA and PS/PMMA blend that meet the criteria in the target area.

Blending PS with PMMA provides a synergistic approach to exploit the high CO_2 absorption capacity of PMMA in order to:

- reduce the overall foam density, decrease the mean cell size and increase of cell density.
- improve foam processability at lower temperatures due to a further decrease of the glass transition temperature in order to increase *VER*.

Carbon-based fillers such as carbon black (CB) and thermally-reduced graphite oxide (TRGO) well known for its infrared radiation absorption and reflection capabilities [21,22], will be used as cell-nucleating agents, while talc will serve as the benchmark nucleating agent. Therefore, foams with superior thermal insulation performance compared to commercially-available foam materials that show thermal conductivity values between 34 mW/mK and 37 mW/mK is also one of the focus of this study.

---

[58] Foams with volume expansion ratio greater than 10 (*VER* > 10).

Besides, there is no available literature on extruded PS (XPS) or PMMA (XPMMA) foams with TRGO as nucleating agent.

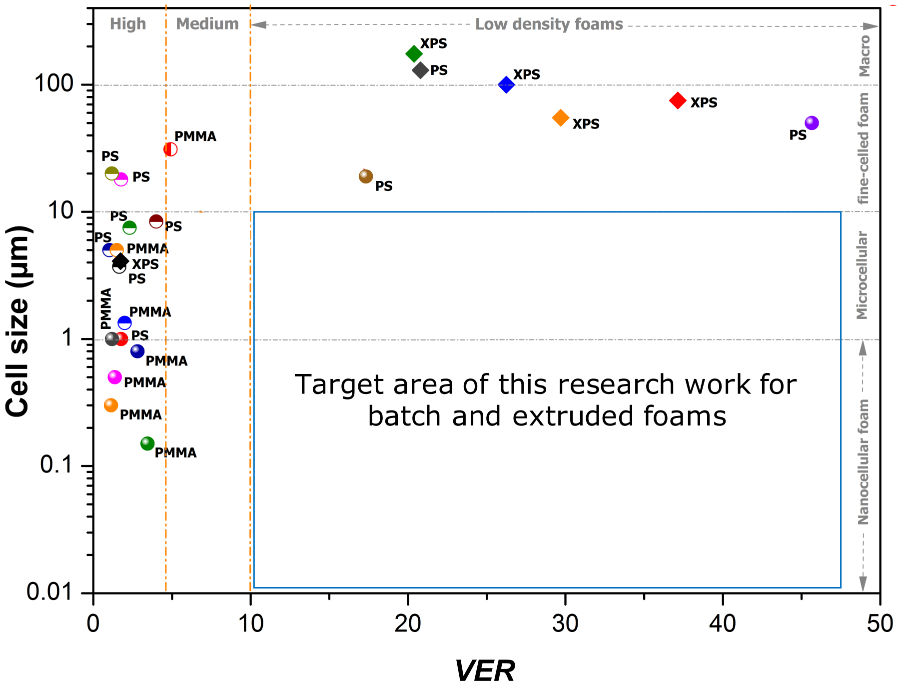

Figure 3.1: Volume expansion ratios (*VER*) as a function of mean cell size for batch and extruded PS and PMMA nanocomposite foams[59] [13,14,45,46,50,54,71,87,110,127,202–205].

3.2 Aims

- The ultimate aim of this thesis is to prepare low thermal conductivity (≤ 33 mW/mK) microcellular low-density closed-cell nanocomposite foams based on PS, PMMA and PS/PMMA blends. As mentioned before, the foams are to be characterized by mean cell sizes of less than 10 µm, density of less than 64 kg/m^3 or volume expansion ratio larger than 10.
- To investigate the influence of blending on CO_2 sorption, desorption and diffusivity properties of the nanocomposites and how it affects the cell sizes, cell densities and volume expansion ratio.
- To investigate the influence of filler size, geometry and content, surface area and dispersion quality in order to control the cell morphology.
- To study the effect of the filler-matrix interfacial interaction on the tensile and rheological properties of the nanocomposites in order to understand and predict foaming behaviour under deformational stresses.
- To study the influence of the use of variable amounts of CO_2 and different die temperatures on the cell microstructure in order to identify the optimum processing conditions for foaming.

---

[59] The survey only considered articles where the densities and corresponding cell sizes were stated. No published articles were found in the literature on XPMMA foams that fulfilled such criteria.

3.3 Strategies

The approaches to be taken in order to realize the set objectives are as follows:

- The nanocomposites of different filler concentrations will be prepared via melt blending from synthesized masterbatches.
- Compounding of the nanocomposites will be performed on a lab-scale twin-screw extruder having configurations that differ in pitch length and number of kneading blocks. This is aimed at achieving high filler dispersion quality within the selected polymer matrices.
- In order to understand and analyse the influence of interfacial strength[60] on the resultant nanocomposite properties, tensile test will be carried out. In addition, dynamic shear rheological experiments will be performed to determine the viscoelastic properties of the nanocomposites, especially if the added fillers are able to form a percolation threshold at very low filler concentration.
- CO_2 solubility experiments will be performed with unfilled and filled nanocomposites to determine their maximum sorption capacities and the diffusivity properties of CO_2.
- The knowledge gained from the gas solubility kinetic experiments will serve as a guide for subsequent solid-state batch foaming studies. From the batch foaming experiments, (i) the foaming behaviour of the homopolymers nanocomposites and nanocomposite blends will be understood. (ii) The right processing parameters will be determined and fine-tuned to realise foams with smaller cell sizes, high cell densities and high volume expansion ratios.
- Foam extrusion studies will be conducted on a tandem line. Since solid-state batch process conditions are not identical to the conditions of the melt state, the knowledge gained from batch foam experimental studies will provide a good base for defining the amount of blowing agent to be metered during foam extrusion.

---

[60] Interface between the fillers and the matrix.

4 Experimental Section

4.1 Materials

4.1.1 Polymer matrix

Commercially-available thermoplastic amorphous polymers: polystyrene (PS 158 K) and poly(methyl methacrylate) (PMMA Plexiglas®7N), were used as base matrices in this work. PS and PMMA were provided by BASF SE, Ludwigshafen, Germany and Evonik Industries AG, Germany, respectively.

The PS 158 K is characterized by a density of 1048 kg/m^3, a weight average molecular weight (M_w) of 335,000 g/mol and a melt flow rate (MFR)[61] of 3 g/10 min. PMMA, on the other hand, has a density of 1190 kg/m^3, M_w of 78,000 g/mol and MFR[62] of 7.14 g/10 min. The chemical structures of both polymers are illustrated in Figure 4.1.

Figure 4.1: Chemical structural formulas of (a) Polystyrene, (b) Poly(methyl methacrylate)

4.1.2 Physical blowing agents

Liquid carbon dioxide with less than 5% moisture content was purchased from Riessner-Gase, Lichtenfels, Germany and ethanol (EtOH ≥ 95 %) was purchased from Sigma-Aldrich, Germany.

4.1.3 Nucleating agents

Nanofillers such as talc, carbon black (CB) and thermally-reduced graphite oxide (TRGO) were used as the main foam nucleating agents, while multi-walled carbon nanotubes (MWCNT) and expanded graphite (EG) were used solely for supplementary experimental purposes. The nanofillers were provided by the respective companies listed in Table 4.1.

All the aforementioned nucleating agents are commercially available with the exception of TRGO. TRGO was synthesized as described in section 4.2.1 at Freiburg Materials Research Centre (FMF), Institute of Macromolecular Chemistry, University of Freiburg, Germany within the framework of the joint project “FUNgraphen” with grant number 03X0111A-D.

---

[61] *MFR* measured according to ASTM D955, at 200 °C, 5 kg.

[62] *MFR* measured according to ISO 1133 at 230 °C, 3.8 kg.

Table 4.1: Suppliers of the respective nucleating agents used in this research work.

Filler	Designation	Supplier	Particle size (µm)
Talc	Mistrocell® M90	Imerys-Talc, Belgium	6^d
CB	Printex® 60-A	Orion Engineered Carbons, Germany	0.021^d
TRGO	TRGO	FMF, Freiburg	5-7^e
MWCNT	Baytubes C 150 P	Bayer Material Science, Leverkusen, Germany	(4 – 13) x 10^{-3d} L > 1
EG	V-EG 98-40	Graphit Krofmühl AG, Germany	6 -11^e

d: Median diameter provided by material suppliers.
e: Mean particle length estimated by scanning electron microscopy.
L: Length of nanotubes.

4.2 Sample preparation

4.2.1 Synthesis of thermally-reduced graphite oxide

Thermally-reduced graphite oxide was synthesized via a modified two-step procedure (Figure 4.2) described by Hummers and Offeman [207]. In a standard experimental procedure, 60 g of natural graphite (KFL 99.5, AMG Mining AG, Hauzenberg, Germany) was dispersed in sulfuric acid (1.4 L). Sodium nitrate (30 g) was introduced into the mixture and it was stirred overnight to allow for complete reaction. The mixture was cooled with an ice bath during which potassium permanganate (180 g) was slowly added over a period of 3 h. The ice bath was then removed and the mixture was left to stir for another 2.5 h until a highly viscous paste was formed. Quenching of the mixture was done by adding ice water and hydrogen peroxide (3%, 200 mL) in a slow fashion until no further gas formation was observed.

In order to obtain graphite oxide (GO) flakes, the resulting mixture was subjected to the following sequential steps: (i) purification by cross-flow filtration with water, (ii) drying under circulating air at 40 °C, (iii) milling with a Cryo-ball mill (Retsch GmbH, Haan, Germany), while being cooled by liquid nitrogen, (iv) drying again at 40 °C under vacuum.

In the second step, the dried GO particles were thermally reduced in a tube furnace at 750 °C under a nitrogen atmosphere to yield TRGO. Elemental analysis of TRGO reveal it to contain: carbon (85.0%), hydrogen (0.4%), sulphur (0.5%) and a total oxygen content of 14.0%.

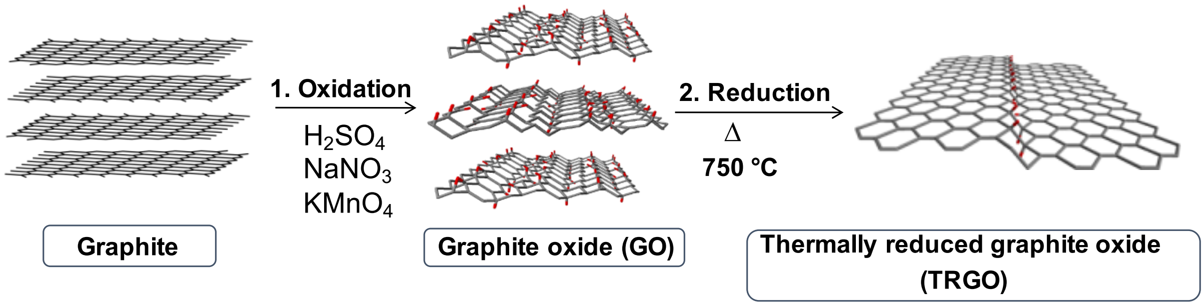

Figure 4.2: Schematic route to TRGO synthesis [208]. *The red colour pendant groups on the surface of GO and TRGO represent oxygen functional groups.*

4.2.2 Masterbatch production

Masterbatches containing 5 wt% of the respective nanofillers (nucleating agents) were prepared as follows:

In separate glass beakers, the fillers were dispersed in ethanol for the synthesis of PS masterbatches and in THF for PMMA masterbatches. By means of an ultrasonic tip dispenser (Sonopuls HD 2200), a typical mixture was sonicated typically for 12 min.

In a second stand-alone step, the respective neat polymer granules were first cooled down with liquid nitrogen and then milled into powder form using a variable speed rotor mill (Pulverisette 14 classic line). The powders were afterwards introduced into another beaker containing the filler-solvent solution mentioned earlier. The resulting dispersion was further sonicated for another 20 min while the beaker is being cooled in a water bath to prevent a rise in temperature of the mixture. The solvent was removed from the dispersion on a rotary evaporator at 40 °C under vacuum, with a pressure of 0.012 MPa. The resultant masterbatches (also in powder form) were subsequently oven-dried at 80 °C under vacuum for 7 days prior to melt blending. It is worth mentioning that the same procedures were carried out for preparing the nanocomposite blends.

4.2.3 Melt compounding

The masterbatches were extruded using an intermeshing co-rotating twin screw extruder (Brabender DSE 20/40, Duisburg, Germany) characterized by an L/D ratio of 40 and a diameter of 20 mm. The setup of the screw is shown in Figure 5.2. The screws were configured with conveying elements having two different pitch lengths (45 mm and 30 mm) in addition to three 45° kneading blocks placed at different zones of the screw. A screw speed of 100 rpm together with the temperature profiles, which can also be found in Figure 5.2, were fixed to achieve a throughput of 2.5 kg/h. A 3-mm-diameter round die was used to extrude the melt strands which were then under-water pelletized into cylindrical pellets in a 2-m-long water bath of 23 °C. The pellets were oven-dried under vacuum at 80 °C for a minimum of 48 h.

In a second extrusion step, the masterbatches were diluted further to the desired filler concentrations (0.1 wt. % to 2.5 wt. %) as required for succeeding experimental steps.

4.2.4 Injection moulding

Prior to moulding, the pellets of the respective polymer matrix were dried in a vacuum oven for 24 h at 80 °C. Afterwards, dumbbell tensile test specimens were moulded on an injection moulding machine (Krauss Maffei KM 65/180/55 CX V) according to DIN EN ISO 527-1, type 1A. The processing parameters are summarized in Table 4.2.

Table 4.2: Injection moulding machine specification and processing parameters.

Clamping force	**L/D**	**D (mm)**	**Max. injection Vol (cm^3)**	**Max. injection *P* (MPa)**
65	26	25	52	250

Injection moulding processing parameters

Sample	**Melt temperature (°C)**	**Mould temperature (°C)**
PS	210	60
PMMA	230	80
PS/PMMA blends	230	80

L: screw length; D: screw diameter; Vol: volume; P: pressure

4.2.5 Compression moulding

Compression-moulded specimens were prepared either for CO_2 sorption experiments, dynamic shear rheological or batch foaming experiments. A hydraulic laboratory hot press PW 100 (P/O/ Weber) with a maximum compression force of 130 kN and maximum operating temperature of 500 °C was used for moulding the samples. Prior to compression, the pellets were dried at 85 °C under vacuum for a period of 24 h. For PS-based samples, a compression melt-temperature of 200 °C was used, while a temperature of 230 °C was used for all PMMA and PS/PMMA blend samples.

First, the pellets were loaded in the appropriate mould and compressed with a force of 10 kN for 5 min at the aforesaid temperatures. Afterwards, the compression force was increased to 110 kN and compression was continued for another 7 min. Secondly, the mould containing the compressed specimens was removed from the hot press and transferred to a cold press which was cooled by circulating water at room temperature. Further compression was continued but with a lower force of 20 kN. The mould was left to stand for 4 min and the specimens were manually removed. The dimensions of the specimens pressed for each test are reported in the corresponding measurement subsections.

4.3 Material characterization

4.3.1 Nanofiller surface area characterization

Brunauer-Emmett-Teller (BET) specific surface area measurements were carried out on a surface area and pore size analyser (Quantachrome Nova 2000 e) at 25 °C and 40 °C, respectively. Prior to carrying out the measurement, the fillers were degassed at 200 °C with standard mantles for 24 h under reduced pressure so as not to cause any structural change to the fillers. BET analysis was conducted under nitrogen gas at 77 K and the specific surface areas of the fillers were determined from the adsorption and desorption isotherms based on equation 4.1 under nitrogen at a 77 K.

$$\frac{1}{W((P_o/P)-1)} = \frac{1}{W_m C} + \frac{C-1}{W_m C}\left(\frac{P}{P_o}\right) \tag{4.1}$$

where W is weight of gas adsorbed, P/P_o is the gas's relative pressure, $W_m C$ is the weight of the fillers that relates directly to the surface area, C is the BET constant which is related to the interaction between the nitrogen gas and the fillers.

4.3.2 CO_2 sorption and desorption kinetics

For these measurements, a pressure autoclave (BERGHOF Lab autoclave HR-500) having a capacity of 500 cm^3 with a maximum operating temperature and pressure of 100 °C and 5 MPa, respectively, was used. As an example, a rectangular compression moulded sample with dimensions (13 mm x 9 mm x 2 mm) was placed into the autoclave and was saturated at 23 °C with a pressure of 5 MPa for 24 h. There were two methods that were employed to estimate the maximum amount of CO_2 absorbed by the sample.

In the first method, the weight gain of the specimen was determined by removing the specimen at regular intervals from the autoclave and weighing the sample on a precise scale. As soon as the specimen exhibited constant weight over time, it meant that the specimen had absorbed the maximum amount of CO_2. The final weight of the specimen was compared to its initial weight prior to sorption. In the second method, the specimen was saturated with CO_2 until equilibrium was achieved. The specimen was then removed and the weight loss at selected intervals was recorded. From equation 2.18, the equilibrium concentration of CO_2 in the specimen (M_0) without any desorption (i.e. estimation of the total amount of CO_2 at time, t = 0) was estimated. For each system, three samples each were measured and the average value was reported. The standard deviations of the measurements were in the range of ± 0.09 wt%.

4.3.3 Dynamic shear rheology

The dynamic shear rheological characteristics of the pressed circular disk samples of the nanocomposites with dimensions (24 mm x 2 mm) were studied under a nitrogen atmosphere using an oscillatory parallel plate rheometer (Rheometric Scientific RDA III).

Prior to testing, the specimens were dried under vacuum at 80 °C for 15 h. The gap between the plates was adjusted to zero position and measurements were conducted at 200 °C. Dynamic strain-controlled sweep measurements (0.1 % to 100 % at 1 rad/s) were performed at first so as to determine the linear elastic regime of the samples, and thereafter frequency sweep tests (0.01 rad/s to 500 rad/s, at 10 % strain) were conducted. A minimum of three samples were tested to obtain the complex shear viscosity η^*, dynamic storage modulus ($G^{/}$), dynamic loss modulus ($G^{//}$) and tan delta (δ).

The conversion of the filler content from weight percentage (wt% into volume percentage (vol%) was calculated using equation 4.2.

$$V_f = \frac{\rho_m . W_f}{\rho_f . W_m + \rho_m . W_f} \tag{4.2}$$

Where V_f is the volume fraction of the filler, ρ_m and ρ_f are the densities of the polymer matrix and filler respectively and W_m and W_f are the weight fractions of the matrix and filler. The densities of the respective fillers are given in Table 4.3

Table 4.3: Densities and geometry nanofillers employed in this study.

Filler type	**Geometry**	**Density (g/cm^3)**
Talc	Plate	2.78
Carbon black (CB)	Spherical	1.80
Thermally reduced graphite oxide (TRGO)	Platelet	2.30

4.4 Morphology characterization

4.4.1 Scanning electron microscopy

The morphologies of compact nanocomposite materials as well as foamed samples were examined on a scanning electron microscope (SEM) (Carl Zeiss Ultra plus FE SEM, Oberkochen, Germany) with an acceleration voltage of 2 kV. To be able to analyse the resultant cellular structures of the foamed materials, the samples were immersed in liquid nitrogen and fractured using a pair of pliers to expose the needed surface area. These surfaces were then manually sputtered with a thin layer of gold prior to microscopic investigation.

4.4.2 Transmission electron microscopy

The quality of filler dispersion in the compact as well as foamed nanocomposite materials were observed under a transmission electron microscope (Zeiss CEM 902A EFTEM) at an acceleration voltage of 80 kV. Ultra-thin sections of the specimens (50 nm) were cut at room temperature using a microtome. For foamed materials, the samples were either pressed into compact form or were embedded in epoxy resin at room temperature prior to being microtomed.

For the estimation of the mean droplet sizes (D_m) of PMMA in PS matrix, a minimum of three TEM images of each blend nanocomposite were analysed using a public domain software "Image J" and the mean taken. The number average densities (ρ_{mn}) of the droplets were estimated by counting the number of droplets per total area of the image under evaluation.

4.5 Mechanical testing

4.5.1 Tensile test

The tensile properties of the compact nanocomposites were measured on a Zwick 1445 universal testing machine according to DIN EN ISO 527-2. The tests were carried out with an initial cross-head speed of 1 mm/min to determine the tensile modulus (E) and was increased afterwards to 10 mm/min to determine the tensile strength (σ_m) and elongation at break (ε_b) until the specimen yielded to fracture. The tensile property values reported are the average of 5 independent measurements from each specimen.

4.6 Foam processing

4.6.1 Batch foaming

Rectangular specimens (13 x 9 x 2 mm^3) were used for all batch-foaming studies. Prior to foaming, the specimens were dried in an oven at 80 °C under vacuum for 12 h.

Temperature-induced batch foaming

For temperature-induced ($\Delta T/\Delta t$) batch-foaming experiments, the specimens were loaded in the autoclave as shown in Figure 4.3a. Saturation was done with a pressure of 5 MPa at 23 °C for 24 h to ensure complete equilibrium concentration condition. Afterwards, the autoclave was slowly depressurized and the samples were taken out. After a desorption time of not more than 5 seconds, the samples were dipped into a pre-heated hot silicon oil bath (Thermal H, Julabo Labortechnik) of 120 °C for between 10 s and 25 s to foam the specimens.

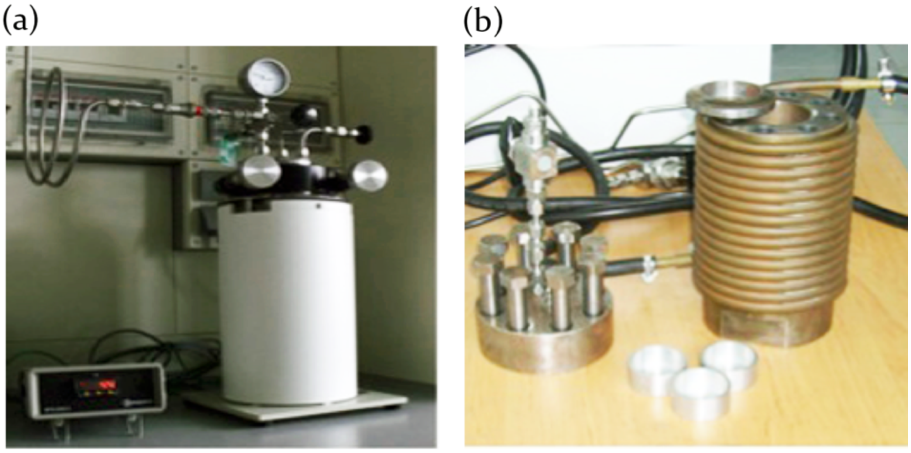

Figure 4.3: Batch-foaming autoclaves (a) BERGHOF lab autoclave HR-500, (b) customized high-pressure autoclave.

The specimens were removed from the hot oil bath and transferred into another cold silicon bath and lastly into a beaker of water (23 °C) to finally quench, stabilize and fix the final cell microstructure.

Pressure-induced batch foaming

The pressure quench ($\Delta P/\Delta t$) experiments were performed in a customized autoclave as shown in Figure 4.3b. The autoclave has a capacity of 25 cm^3 with a maximum operating temperature of 200 °C and a maximum pressure of 30 MPa.

In a standard experiment, the specimens were placed into the autoclave which was then sealed. The autoclave was heated from room temperature up to 135 °C (selected saturation temperature). After the set temperature was reached, the specimens were saturated with CO_2 at a constant pressure of 15 MPa to 20 MPa for 6 h to 20 h to attain the equilibrium saturation concentration. The autoclave was then rapidly depressurized through a valve at a controlled pressure drop rate of 2 MPa/s to 6 MPa/s. The foamed specimens were promptly removed from the autoclave and cooled by air or water. After several trials, the following conditions were fixed as the optimum foam-processing parameters: $T_{saturation}$ = $T_{foaming}$ = 135 °C, $P_{saturation}$ = 20 MPa, $\mathrm{d}P/\mathrm{d}t$[63] = 6 MPa/s because foams with smaller cells, homogenous cell structures and *VER* larger than 5 were generated.

4.6.2 Foam extrusion

All foam extrusion studies were performed on a tandem-extrusion-line (Dr Collin) schematically illustrated in Figure 4.4. The primary melt-extruder had a screw length of 42 D and the secondary extruder had a screw length of 30 D. The maximum allowable screw speeds were: 460 rpm for the primary melt extruder and 240 rpm for the secondary extruder. The maximum throughput of the tandem line was 15 kg/h and foams were processed with a maximum melt temperature of 450 °C.

---

[63] Pressure drop rate.

Supercritical CO_2 was injected into the melt by means of a positive displacement syringe pump connected to a gas-dosing Maximator at a specific point indicated in Figure 4.4.

A standard representative processing profile for the nanocomposite foams is depicted in Figure 4.4 and other processing details are reported in the corresponding results and discussion section of this thesis. Typically, nanocomposite foams using 0.025 wt%, 0.1 wt%, and 1 wt% and the respective nucleating agents were prepared using the standard temperature profile with a deviation of ± 10 °C. Supercritical CO_2 and ethanol were used individually and in combination (details are explained in the results and discussion section).

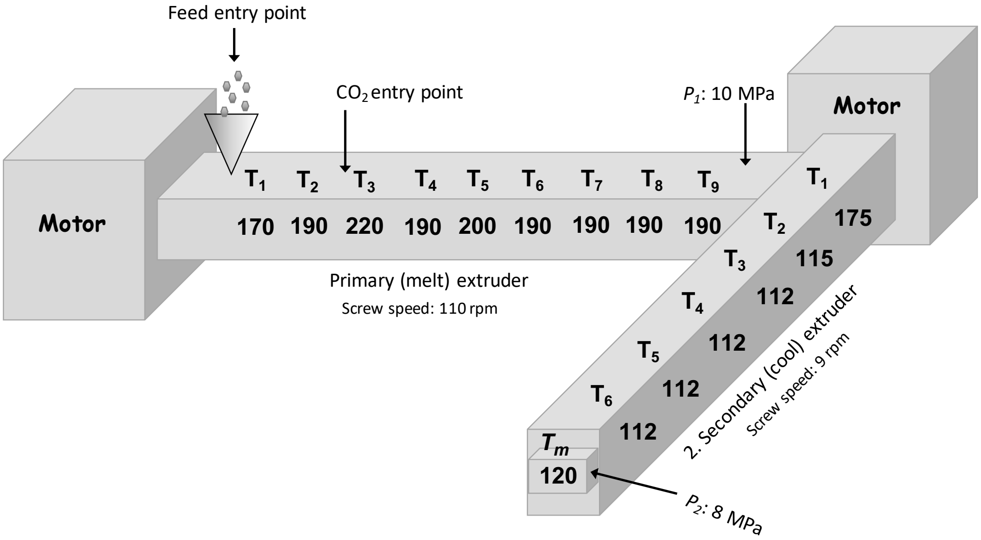

Figure 4.4: Standard foam extrusion processing parameters and conditions. P_1 and P_2 are the pressures in the respective extruders

For foam expansion ratio experiments, a round die of diameter 3 mm was used, while a slit die of 10 mm in length and gap of 0.5 mm was used for the production of regular foam panels. The cylindrical foams obtained from the round die needed no form of calibration but the foam panels were calibrated by means of two metal fabric-coated temperature-controlled-plates (200 mm x 100 mm). The plates were fixed between 5 mm and 10 mm away from the die and the foam panels were cut manually at specific lengths after exiting from the plates.

4.7 Foam property characterization

Foam density

The foam densities of the prepared nanocomposite foams were ascertained by a water-displacement method density scale kit (Mettler Toledo AG245) and according to ISO 1183. A minimum of 5 specimens of each nanocomposite foam were measured and the average values are reported.

Cell density

The cell densities were estimated from equation 2.26. As a standard, a minimum of three SEM images of each foam sample were analysed to obtain the mean cell size, cell size distribution and cell density. About 100 to 200 cells were selected from a well-defined area on the 2D SEM images and the estimations were made using a public domain software "Image J".

Cell wall and struct thickness

The t_{cw} and $t_{s.eq}$ were determined from the evaluation of three SEM images of the respective foams having more than 150 cells. t_{cw} was estimated by measuring the thickness in the middle of the cell walls, while $t_{s.eq}$ was estimated according to equation 4.3 by modelling the cell strut as a circle.

$$t_{s.eq} = (\sqrt{A/\pi}) \tag{4.3}$$

Open cell content

The open cell contents of the prepared nanocomposite foams were analysed according to DIN ISO 4590 with the aid of a gas pycnometer (ULTRAFOAM 1000 Model UPY - 15F). Cylindrical samples were loaded into the cell of 10 cm^3 which was then closed. Nitrogen gas was passed through the specimen at a very low pressure (0.035 MPa) for a designated period of time. The open-cell content (OC) was then determined from the expression in equation 4.4 which compares the volume of the sample into which the applied gas diffused ($V_{diffused}$), with the geometric volume ($V_{geometric}$) of the sample. Three specimens were analysed per foam material.

$$OC = \left(\frac{V_{geometric} - V_{diffused}}{V_{diffused}}\right) \times 100\ \% \tag{4.4}$$

Thermal conductivity

A Lasercomp FOX50 double-plate heat flow meter with a resolution of 10^{-4} W/mK was used to measure the thermal conductivities of the extruded nanocomposite foams. The measurements were conducted at the following temperatures: 23 °C, 35 °C, 50 °C, 70 °C, 90 °C with a temperature difference of 10 °C between the hot and cold plate. Circular samples of diameter 60 mm and thickness 2.5 mm were used for these measurements.

5 Results and Discussion

5.1 Characterization of bulk materials

5.1.1 Specific surface areas of nanofillers

The specific surface areas (A_{sp}) of the nanofillers were determined via Brunauer-Emmett-Teller (BET) measurements and the results are presented in Table 5.1. The graphite-based fillers such as TRGO and EG were observed to have the highest specific surface areas. The fillers were further examined under a scanning electron microscope to reveal their primary structures as shown in Figure 5.1.

Table 5.1: Particle characteristics of the fillers employed in this study.

Filler type	**Geometry**	**Specific surface area (m^2/g)**
Talc	Plate	17
Carbon black (CB)	Spherical	122
Thermally reduced graphite oxide (TRGO)	Platelet	600
Expanded graphite (EG)	Platelet	60
Multi-walled carbon nanotubes (MWCNT)	Tube	198

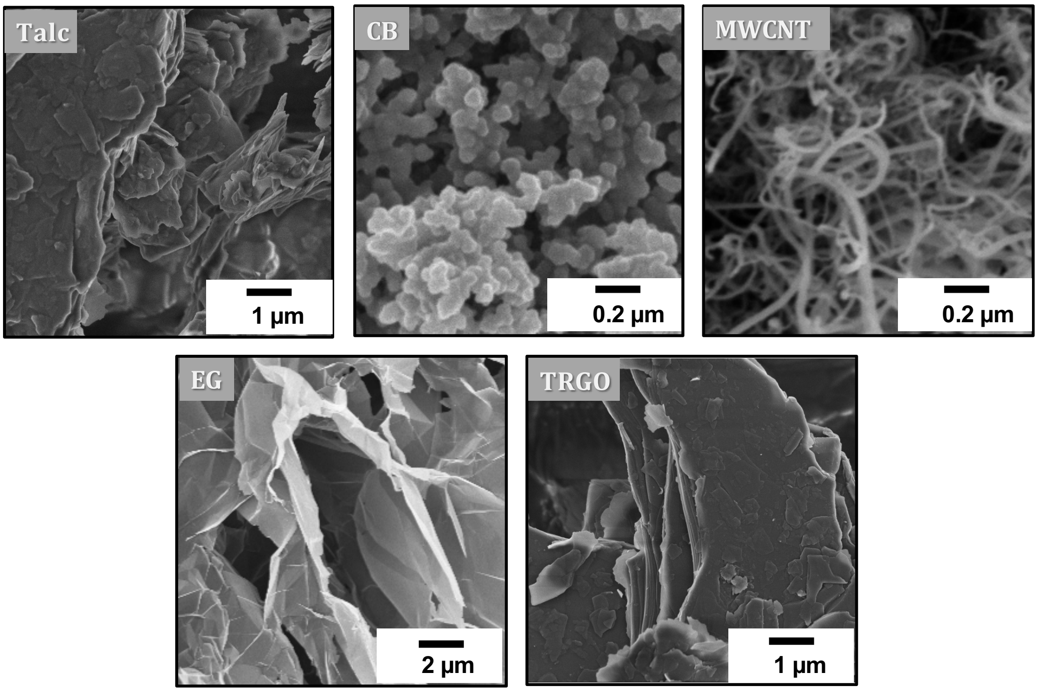

Figure 5.1: Scanning electron microscope images of the primary filler structures.

5.2 Morphology of compact nanocomposites

5.2.1 Nanocomposite production via melt blending

The masterbatches and nanocomposites were compounded with closely intermeshing co-rotating twin-screws having a configuration that is illustrated in Figure 5.2. The very close gaps between the screws and the different pitch lengths of the conveying elements enabled good mixing in the axial and radial (cross-sectional) directions of the screws. Prior to selecting this screw configuration, which was designated as medium-shear (*MS-C*), several other combinations were tested and were evaluated based on the quality of the filler distribution[64] and dispersion[65] in the polymer matrix.

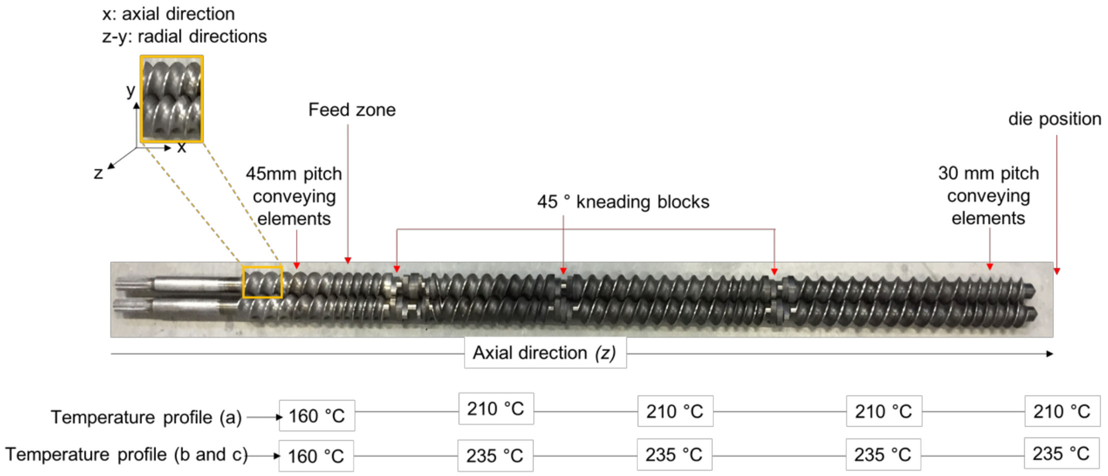

Figure 5.2: Schematic of the *MS-C* screw setup and temperature profile for melting blending of (a) PS, (b) PMMA and (c) PS/PMMA blends (90/10 and 80/20).

For instance, the dispersion quality of expanded graphite in PS processed under identical processing conditions (screw speed: 100 rpm; throughput: 2 kg/h) by two differently configured screws, namely low-shear screw (*LS-C*) and medium shear screws, was evaluated. The *LS-C* screw was configured with four 45 ° kneading blocks and all-through 45 mm conveying elements while the *MS-C* screw was designed with six kneading blocks and a mixture of 45 mm and 30 mm conveying elements.

The light microscopic images in Figure 5.3 reveal that better dispersion of EG was achieved with the *MS-C* screw. Furthermore, agglomerates were apparent in the PS nanocomposite compounded with *LS-C*. The is because of the longer pitch lengths of the conveying elements in the *LS-C* screw which implies that higher pitch lengths lead to faster transportation (higher velocity) of polymer melt along the axial direction but with less mixing in the cross-sectional direction of the screw and vice versa. However, in the case of *MS-C* screw, having a mixture of both 45 mm and 30 mm conveying elements led to improved mixing in both directions and this interpretation is well supported by the light microscopic image. Based on these results, the *MS-C* screw was adopted as the standard screw configuration for all other compounding trials.

---

[64] Distribution refers to the way the particles fill homogenously in the space or spatial arrangement of the particles; i.e. how equally spaced the particles are from their nearest neighbor.

[65] Dispersion refers to the level of particle agglomeration.

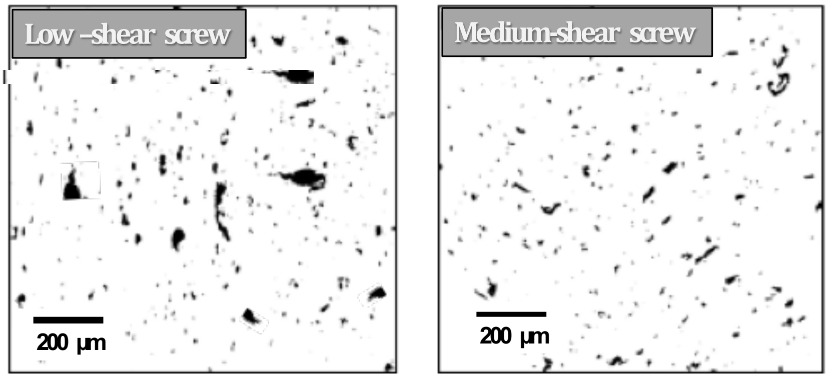

Figure 5.3: Light microscopy micrographs of PS/1.0 wt% EG compounded *LS-C* screw and *MS-C* screw.

5.2.2 Morphology of PS nanocomposites

For PS nanocomposite morphology studies, the geometries of the fillers were taken into account. PS nanocomposites were first prepared with talc, CB and TRGO at a filler content of 5 wt% and were further diluted to lower concentrations of 0.1 wt%, 0.5 wt% and 1 wt% that are suitable for subsequent foaming studies.

The morphologies of the nanocomposites were examined under a transmission electron microscope and the images are shown in Figure 5.4. At low magnification, the fillers appear well dispersed in the matrix but a closer look at images at higher resolution shows the presence of tiny agglomerates. It is well-known that particles that possess van der Waals forces of attraction are able to agglomerate even if these forces are weak. The characteristic properties of the particles are presented[66] in Table 5.2.

The number of particles (N_p) per area (µm²) of the respective fillers estimated from at least three TEM images can be found in Table 5.2 as well. The mean thickness of the individual talc particles was found to be 25 nm and about 190 nm for the talc particle agglomerates. The mean particle thickness of TRGO particles was estimated to be 10 nm. Irrespective of the filler concentrations, the mean thickness of the individual fillers more or less did not change. Slight changes were only observed with respect to the mean particle sizes for all particles.

The aspect ratio (A_R) of the particles estimated from equation 5.1 shows talc particles to have larger A_R than that of TRGO.

$$A_R = \frac{l_{\text{ave}}}{t_{\text{ave}}} \tag{5.1}$$

where l_{ave} is the average lateral length and t_{ave} is the average thickness or diameter of the filler particle. The A_R of TRGO is seen to decrease as the filler content was decreased to 0.5 wt% by 23 %. These reductions are a result of filler attrition caused by melt-blending. Further to that, the inter-particle distance was found to be larger for talc particles, followed by CB[67], and then TRGO particles.

---

[66] Please note: the estimated values for nanocomposites of 0.1 wt% and 1 wt% are omitted as the results do not significantly differ from those of 0.5 wt% nanocomposites.

[67] if the tiny size of the agglomerates is not considered.

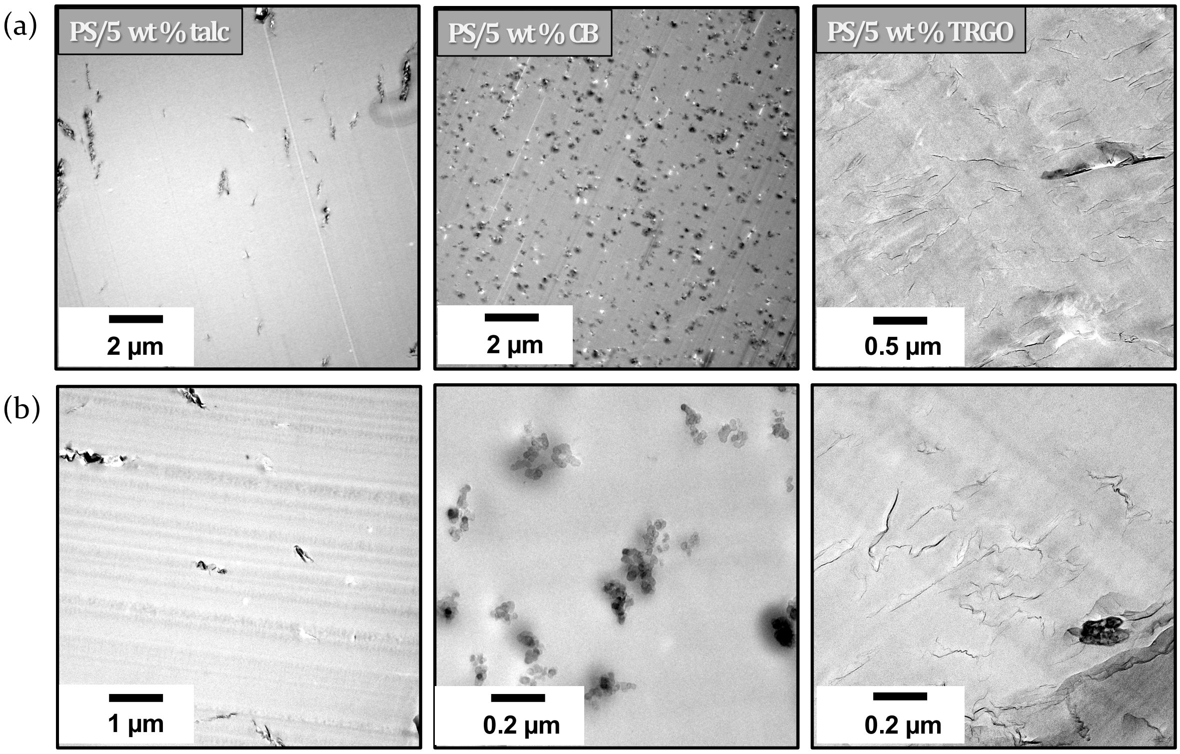

Figure 5.4: TEM images of PS nanocomposite morphologies (a) low magnification (b) high magnification.

Table 5.2: Particle characterization of PS nanocomposites.

	Filler content (5 wt%)			Filler content (0.5 wt%)		
Filler	l_{mp} (nm)	N_p (µm^{-2})	A_R	l_{mp} (nm)	N_p (µm^{-2})	A_R
CB	105 ± 4	11^{ag}	1	92 ± 5	0.40^{ag}	1
Talc	502 ± 20	0.61	20	483 ± 26	0.32	19
TRGO	208 ± 24	35	21	157 ± 33	6.11	16

l_{mp}: mean particle lateral length; ag: agglomerated particles.

Conclusively, the screw configuration *MS-C* used for the compounding of the nanocomposites resulted in good distribution and dispersion, also at lower filler content (Figure 5.5).

Since TRGO fillers have the highest N_p values, PS/TRGO nanocomposite foams are expected to generate higher cell and nucleation densities, followed by PS/CB, and then PS/talc nanocomposite foam.

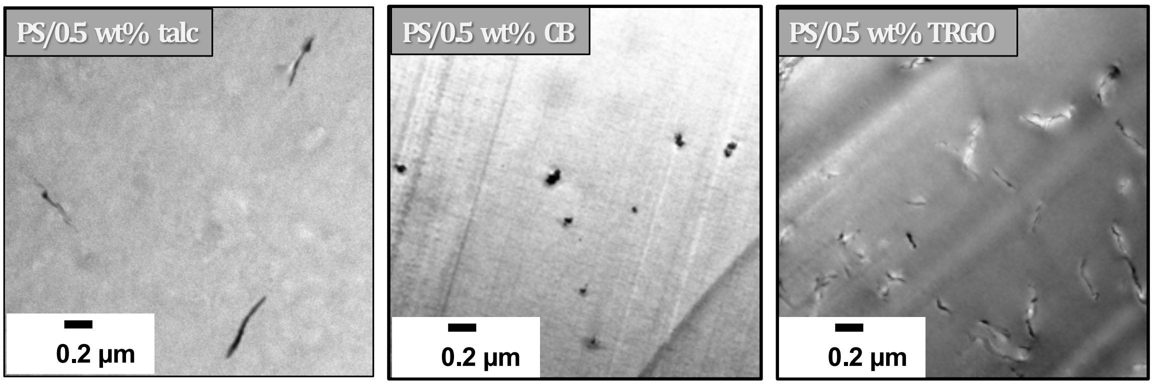

Figure 5.5: TEM micrographs showing the morphologies of the PS nanocomposites at filler content of 0.5 wt%.

5.2.3 Morphology of PMMA nanocomposites

Analogous to PS nanocomposites, PMMA nanocomposites were prepared with talc, CB and TRGO with exactly the same filler content. The morphology results shown in Figure 5.6 (a–b) indicate that, at a filler content of 5 wt%, talc and TRGO fillers were well dispersed in PMMA matrix in comparison to CB nanoparticles. The CB particles appeared to form large clusters about three orders of magnitude larger than was seen in PS nanocomposites (Table 5.3). A possible reason for this might be insufficient shear force impacted by the *MS-C* screw or that the surface functional groups of the CB particles are hydrophobic to the carbonyl functional groups of PMMA.
Further dilution of the filler content to 0.5 wt% resulted in breakage and a tremendous decrease of the cluster sizes from about 1400 nm to 285 nm. Figure 5.6c shows that CB nanoparticles were successfully distributed and dispersed within the PMMA matrix. Table 5.3 summarizes the characteristics of the nanocomposite morphology. The t_{ave} of talc particles was estimated to be 35 nm and 100 nm for the small agglomerates present in the system. The t_{ave} of TRGO particles was found to be approximately 10 nm, similar to their size in the PS matrix. Similarly, there were no noticeable changes in t_{ave} at low filler concentration.

By comparing the morphology of PS and PMMA nanocomposites based on N_p and t_{ave}, it can be concluded that talc particles are better dispersed in PMMA than in PS while CB and TRGO fillers are well dispersed in PS compared to PMMA.

Again, the higher N_p values of TRGO in comparison to talc and CB means that PMMA/nanocomposites would deliver foams characterized by higher cell and nucleation densities, followed by PMMA/CB, and then PS/talc nanocomposite foams.

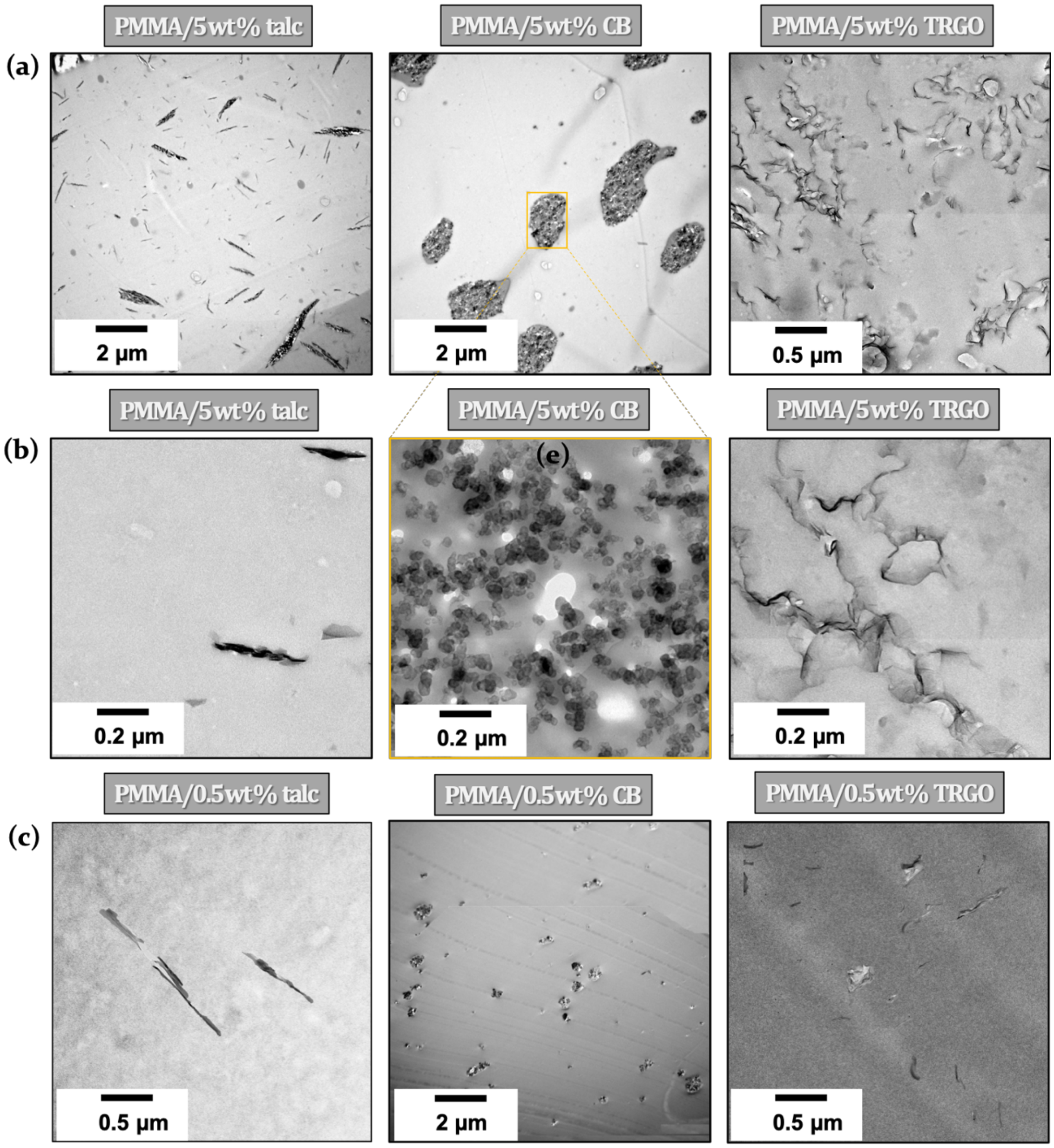

Figure 5.6: Morphology PMMA nanocomposites at (a) low magnification (b) high magnification (c) low filler content.

Table 5.3: Filler size characterization of PMMA nanocomposites.

	Filler content (5 wt%)			**Filler content (0.5 wt%)**		
Filler	l_{mp} (nm)	N_p (µm^{-2})	A_R	l_{mp} (nm)	N_p (µm^{-2})	A_R
CB	1148 ± 22	0.07^{ag}	1	285 ± 4	0.35^{ag}	1
Talc	470 ± 12	1.23	13	376 ± 20	0.95	8
TRGO	225 ± 14	22	23	221 ± 7	3.50	22

l_{mp}: mean particle lateral length; ag: agglomerated particles.

5.2.4 Morphology of PS/PMMA blend nanocomposites

Blends of PS with PMMA were processed for synergistic reasons as earlier stated. Unfilled blends ratios: 90/10 and 80/20 were prepared and the resultant morphologies were examined under a transmission electron microscope. Both blend ratios resulted in sea-island structures as shown in Figure 5.7; i.e. droplets of PMMA dispersed in PS (the continuous phase). This is a consequence of the viscosity ratio difference between PS and PMMA.

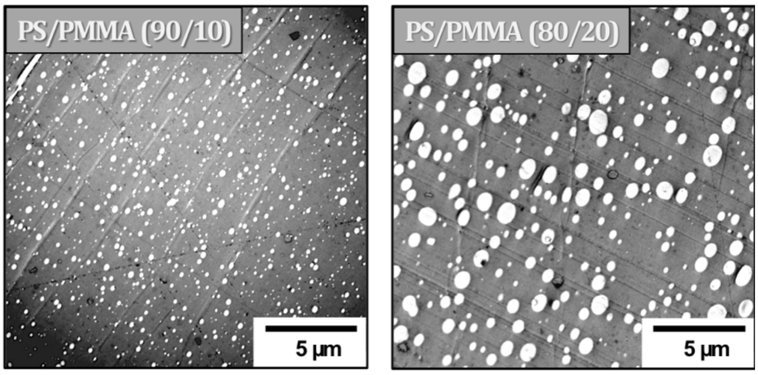

Figure 5.7: Morphology of neat PS/PMMA blends.

The morphologies of the blends are observed to be characterized by small[68] and big[69] droplets of distinct sizes. The corresponding mean droplet diameter (D_m) and droplet number average densities (ρ_{mn}) of the respective blends are given in Table 5.4.

On one hand, D_m, $D_{m.s}$, and $D_{m.b}$ of the dispersed phase in the 90/10 blend were increased by at least 100 % when the PMMA component was increased from 10 wt% to 20 wt% (i.e. 80/20 blend). On the other hand, the ρ_{mdn}, $\rho_{mdn.s}$ and $\rho_{mdn.b}$ decreased in equal fashion when PMMA content was increased from 10 wt% to 20 wt%.

Table 5.4: Characteristics of PMMA droplet sizes in PS matrix.

Blend ratio (PS/PMMA)	$D_{m.s}$ (µm)	$D_{m.b}$ (µm)	D_m (µm)	$\rho_{mn.s}$ (µm^{-2})	$\rho_{mn.b}$ (µm^{-2})	ρ_{mn} (µm^{-2})
90/10	0.14 ± 0.01	0.27 ± 0.01	0.17 ± 0.02	1.73	0.58	2.30
80/20	0.29 ± 0.02	0.71 ± 0.03	0.45 ± 0.01	0.57	0.29	0.76

$D_{m.s}$: mean diameter of small droplets; $D_{m.b}$: mean diameter of big droplets

$\rho_{mn.s}$: number average density of small droplets; $\rho_{mn.b}$: number average density of big droplets

For subsequent morphology studies, the blends were prepared only with TRGO based on the fact that TRGO filled nanocomposites displayed noteworthy and remarkable flow behaviour compared to the

---

[68] Droplets are designated as small if they fall below the median value of the distribution.

[69] Droplets are designated as big if they fall above the median value of the distribution.

nanocomposites filled with talc and CB. Similar filler concentrations (0.1 wt%, 0.5 wt%, 1 wt% and 5 wt%) were used to prepare the blend nanocomposites. The resultant morphologies of the neat versus filled blends are displayed in Figure 5.8.

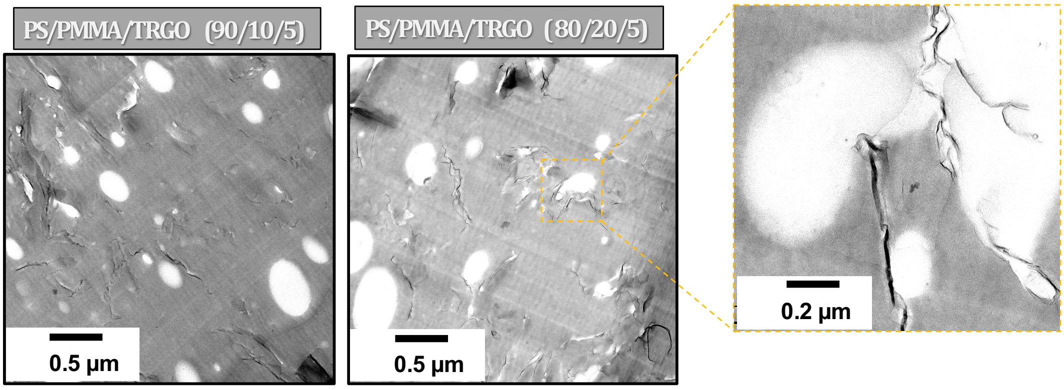

Figure 5.8: TEM images showing the morphology of PS/PMMA/TRGO blends.

The dimensional characteristics of the TRGO fillers in the blends are summarized in Table 5.5. There were no considerable changes observed in the length and aspect ratio of TRGO particles at lower content of 0.1 wt%, 0.5 wt% and 1 wt%. The t_{ave} was estimated to be 10 nm at all filler concentration.

Table 5.5: Filler size characterization of PS/PMMA blend nanocomposites

	Filler content (5 wt%)			**Filler content (0.5 wt%)**		
Filler	l_{mp} (nm)	N_p (µm^{-2})	A_R	l_{mp} (nm)	N_p (µm^{-2})	A_R
90/10	188 ± 24	29	19	180 ± 18	4.1	18
80/20	196 ± 15	25	20	185 ± 20	3.4	19

5.2.5 Conclusions on nanocomposite morphology

Based on the morphologies of the respective nanocomposites prepared, the following conclusions could be drawn:

- Irrespective of the filler concentration, the size of CB nanoparticle agglomerates observed in PMMA was larger than that in PS nanocomposites. This might be due to hydrophobic interaction between the functional groups of CB nanoparticles.
- CB and TRGO fillers show a higher N_p in PS than in PMMA while talc particles demonstrated a higher N_p in PMMA than in PS.
- The designed *MS-C* screw led to better mixing and dispersion of the fillers in the PS and PMMA matrices, especially with TRGO fillers.
- Judging from the estimated N_p of TRGO in PS, PMMA and PS/PMMA blends, it can be concluded that TRGO particles have stronger affinity for PS than for PMMA.

- Increase of the PMMA content by a factor of two in the blend increased the mean sizes of the droplets as well as the droplet number average densities by at least a factor of two.

5.3 Rheology of compact nanocomposites

Rheological studies of nanocomposites are important because information obtained from these experiments can be used to predict the foaming behaviour of the nanocomposites under deformational stresses. As explained earlier, elongational rheological studies are best suited for semi-crystalline polymers that have low melt strength such as PP and polymers that display a different viscoelastic behaviour when a slight change such as branching is made to their molecular architecture. Since such challenges are not associated with neither high molecular weight PS nor PMMA, shear rheological experiments were used to characterize the nanocomposites in this work.

By performing isothermal dynamic frequency sweep measurements on an oscillatory parallel plate-plate rheometer, the viscoelastic responses of the prepared nanocomposites reinforced with talc, CB and TRGO at different filler content were investigated. The test results revealed the melt rheological and microstructural characteristics at the molecular level in relation to the filler concentration.

5.3.1 Dynamic shear response of PS nanocomposites

Complex shear viscosity

Figure 5.9 shows the dynamic shear responses of PS nanocomposites where the complex shear viscosity (η^*) is plotted as a function of the angular frequency (ω). The relationship between η^* and ω is expressed in equation 5.2.

$$\eta^* = \frac{G''}{\omega} \quad 5.2$$

At 5 wt% filler concentration, a two-fold increase of the $\eta^*$of PS/TRGO in the non-terminal region[70] was observed in comparison to the all other nanocomposite systems. While the nanocomposites of PS/CB and PS/talc exhibited Newtonian behaviour at low frequencies, that of PS/TRGO indicated a phenomenon known as yielding[71]. This phenomenon signifies the presence of filler-network formation, which implies that flow began after a certain magnitude of stress was reached. In other words, the shear stress overcame the chain entanglements. The filler network formation by TRGO particles can be supported by the number of particles/µm^2 (Table 5.2), which was observed to be significantly higher than that of CB and talc particles.

---

[70] Low frequency region.

[71] Yielding is a time dependent non-linear transition from elastic behaviour to flow.

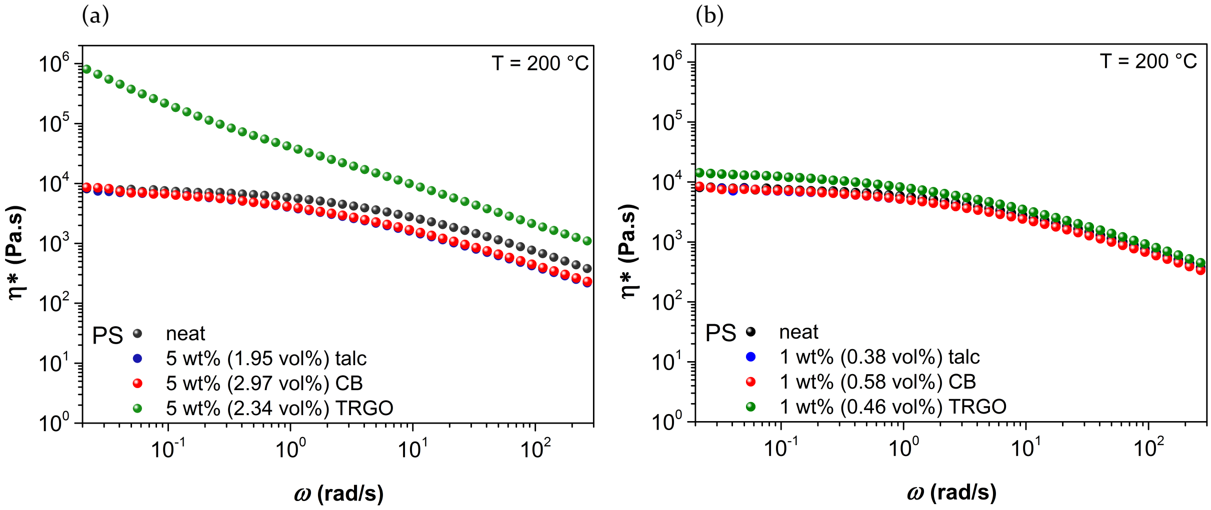

Figure 5.9: Complex shear viscosity as a function of angular frequency for PS nanocomposites (a) 5 wt%, (b) 1 wt%.

At higher angular frequencies, all nanocomposites displayed shear thinning behaviour, which is characteristic of linear chain polymers. At a lower filler content of 1 wt%, no particle network formation was observed with any of the fillers. The $\eta^*$of PS/1 wt% TRGO (0.1 wt. % and 0.5 wt % not shown) was slightly higher than PS/neat, PS/1 wt% talc and PS/1 wt% CB but all remained at the same magnitude as can be seen in Figure 5.9b.

Storage Modulus

The storage modulus (G') as a function of angular frequency for all PS nanocomposites is shown in Figure 5.10. At low angular frequencies and at a filler content of 5 wt%, a Newtonian plateau was observed for PS/TRGO nanocomposite due to particle network formation.

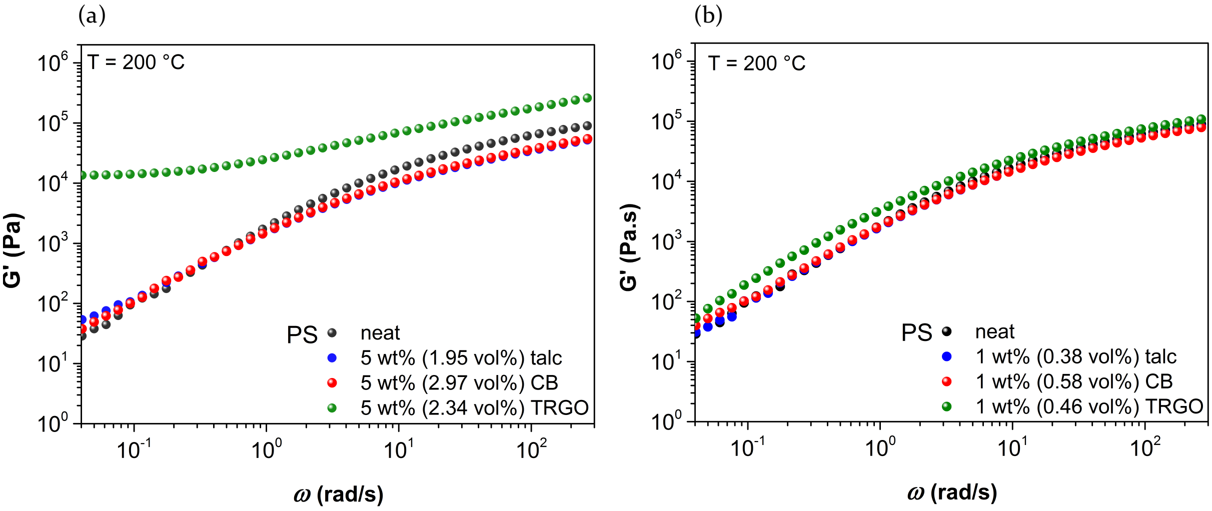

Figure 5.10: Storage modulus as a function of angular frequency for PS nanocomposites (a) 5 wt% and (b) 1 wt%.

This Newtonian plateau showed that PS/TRGO nanocomposite had a more elastic structure compared to the nanocomposites of talc and CB. At 1 wt% (Figure 5.10b), a slight increase of G'particularly at low angular frequencies was seen with TRGO compared to talc and CB fillers.

Melt percolation threshold formation

In Figure 5.11 is shown a plot of phase angle (δ) versus the absolute complex modulus ($/G^*/$). For the PS/neat nanocomposite, the δ curve rises (Figure 5.11a) as $/G^*/$ decreased until it plateaus at 90°. This type of curve is typical of unfilled PS and corresponds to what has been described in the literature [180]. It also means that unfilled PS exhibited viscous behaviour when δ = 90°.

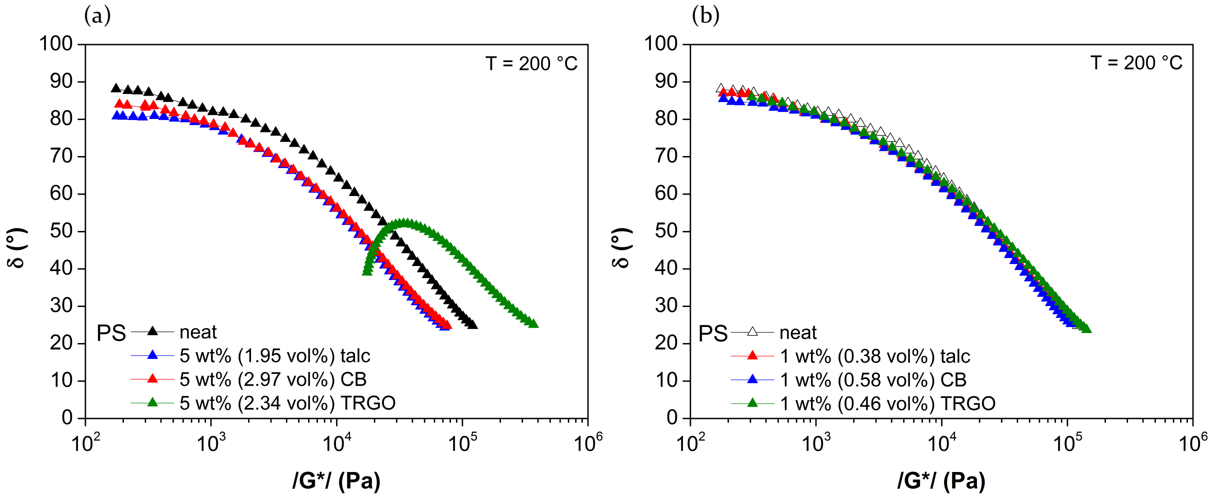

Figure 5.11: van Gurp-Palmen plot of PS nanocomposites with filler contents of (a) 5 wt%, (b) 1 wt%

At a filler concentration of 5 wt%, the phase angles of talc (δ = 84°) and CB (δ = 81°) were observed to be lower than 90° and, as such, they possessed a character similar to viscous materials. Still, at the same concentration (5 wt%), TRGO particles presented a contrasting remarkable elastic response that showed the rise of the δ-curve as $/G^*/$ decreased. It passed a maximum at δ = 52° and then dropped. This is an indication of the particle percolation threshold formation and it signifies the presence of constraints during the chain relaxation process. Unlike in electrical threshold, the particles do not necessarily have to touch each other in order to form rheological thresholds [209]. Likewise, at a filler concentration of 1 wt% (Figure 5.11b), all the nanocomposites showed characteristic curves very similar to the unfilled PS but with a slight decrease of δ from 86° to 87°.

5.3.2 Dynamic shear response of PMMA nanocomposites

Complex shear viscosity

The complex shear viscosity curves of the prepared PMMA nanocomposites can be viewed in Figure 5.12. The presence of a yield stress is visible in the η^*curve for PMMA/5 wt% TRGO nanocomposite. Similar behaviour was also observed in PS/TRGO nanocomposite at the same filler concentration. The PMMA/talc and PMMA/CB nanocomposites exhibited Newtonian behaviour identical to that of PMMA/neat at low angular frequencies. The η^*in this region is more than one order of magnitude higher than for PMMA/neat. As the angular frequency increased, all the nanocomposites displayed shear thinning behaviour as expected.

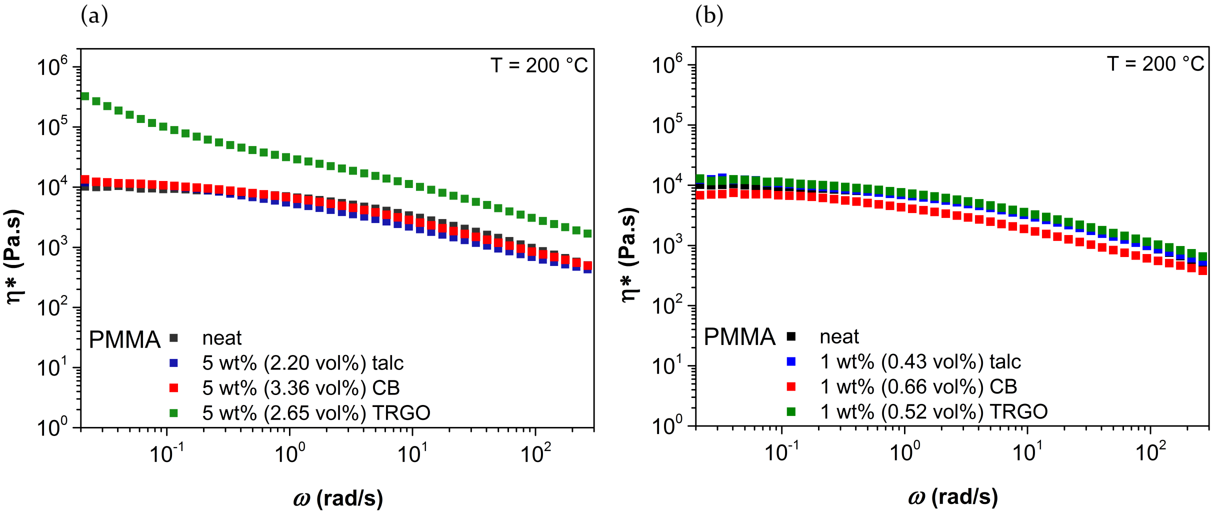

Figure 5.12: Complex shear viscosity as a function of angular frequency for PMMA nanocomposites at (a) 5 wt% (b) 1 wt% filler concentration.

At a filler content of 1 wt%, the $\eta^*$of PMMA/neat was slightly decreased by the presence of CB nanoparticles in comparison to talc and TRGO. A reasonable explanation for this might be that, at such low filler content, the molecular interaction of the CB nanoparticles with PMMA (illustrated in Figure 5.13) allows the neighbouring chains of the matrix to disentangle and thus slide past one another. Similar results have also been reported in the literature [173].

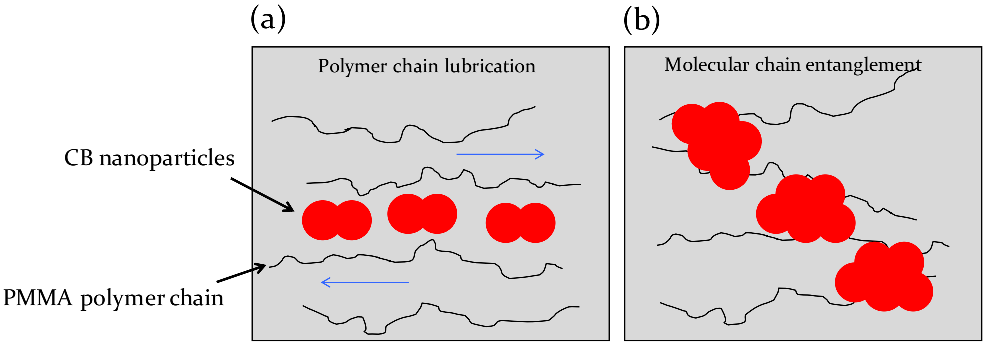

Figure 5.13: Schematic diagram showing the effect of CB spherical nanoparticles agglomerate sizes on polymer chain mobility at (a) low concentration (b) high concentration.

Storage Modulus

The storage modulus curves of the PMMA nanocomposites are presented in Figure 5.14. Interestingly, the formation of plateaus at low angular frequencies was observed for all filled PMMA nanocomposites at 5 wt% filler concentration. Although it is less pronounced for PMMA/talc and PMMA/CB nanocomposites but it is in contrast to what was observed for PS nanocomposites filled with the same fillers. Again, the significantly higher number of particles/µm^2 estimated (Table 5.3) for TRGO in comparison to talc and CB is ascribed to this result. Also, at a filler content of 1 wt%, what appears to look like the start of plateau formation can be seen for the PMMA/TRGO nanocomposite. Additionally, a slight decrease of G' is seen with CB nanoparticles at higher frequencies, due to that already reported for PS/CB nanocomposites.

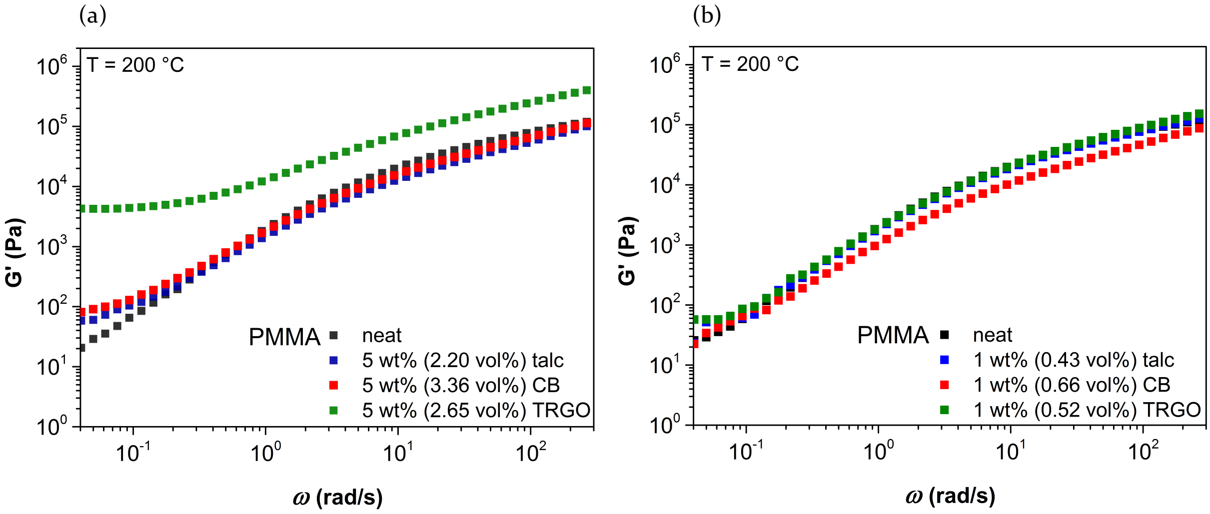

Figure 5.14: Storage modulus as a function of angular frequency for PMMA nanocomposites at (a) 5 wt% and (b) 1 wt% filler content.

Melt percolation threshold formation

The shape of the PMMA/neat curve in the van Gurp-Palmen plot shown in Figure 5.15 is concave. As $/G^*/$ decreases, the phase angle curve rises until it plateaus at $\delta = 90°$. This behaviour is consistent with viscous linear chain polymers. The inclusion of 5 wt% TRGO particles caused a maximum at $\delta = 67°$ before descending downward. This implies the formation of a rheological threshold[72] by the fillers. Unlike in PS, the curves are all shifted to the right of PMMA/neat and it is interesting to see that the shape of the curves changed slightly from concave to convex when the respective fillers were added at 5 wt% and 1 wt%, respectively.

Lastly, significant changes of the flow behaviour of PMMA are influenced more by TRGO particles than CB and talc at 5 wt%. This effect is associated with the difference in dispersion quality found in the respective nanocomposites.

---

[72] Rheological threshold is an indication of elastic behaviour.

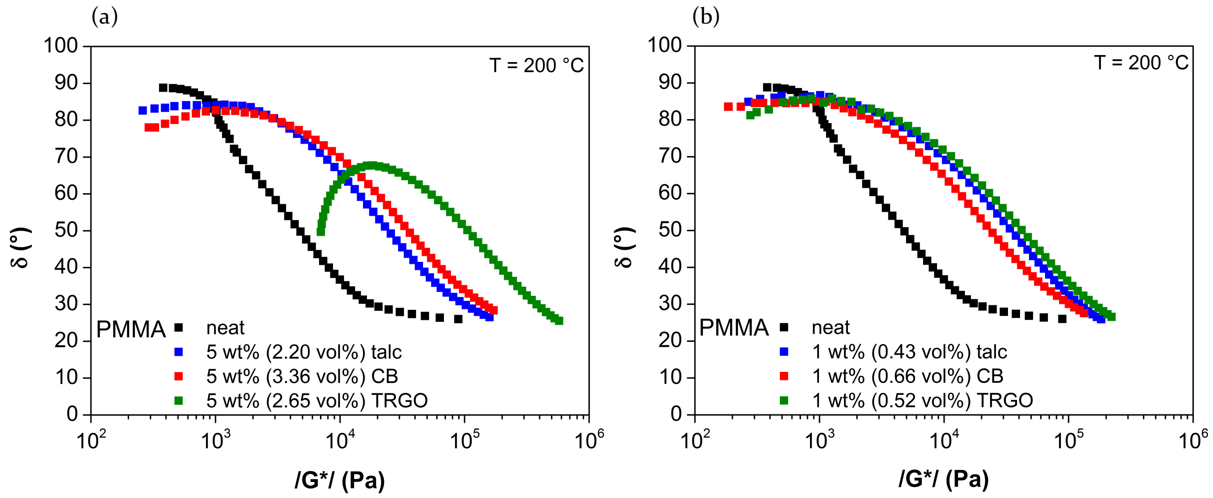

Figure 5.15: Van Gurp-Palmen plot of PMMA nanocomposites at filler content of (a) 5 wt% (b) 1 wt%.

5.3.3 Dynamic shear response of PS/PMMA blend nanocomposites

For the shear rheological studies of the blend nanocomposites, only blends filled with TRGO fillers were carried out. This is because TRGO has proven to display significant and interesting flow behaviour in both PS and PMMA nanocomposites in comparison to talc and CB nanoparticles.

Complex shear viscosity

Figure 5.16 shows comparatively complex shear viscosities of all PS, PMMA and PS/PMMA blends nanocomposites prepared with TRGO at filler concentrations of 5 wt% and 1 wt%. As expected, all nanocomposites filled with 5 wt% TRGO exhibited particle network formation at low angular frequencies, and, at higher angular frequencies, shear thinning behaviour characteristic of linear chain polymers was observed. Further to that, the PS/PMMA/neat (80/20) blend showed a slight but insignificant increase of η^* in contrast to the 90/10 blend. This can be a direct influence of the PMMA-droplet sizes in the blend as the ratio is increased from 10 wt% to 20 wt%. In a similar fashion, both 90/10 and 80/20 blends portrayed marginally higher η^* than the individual homopolymers of PS and PMMA.

Furthermore, at low angular frequencies, the $\eta^*$of the PS/PMMA blends (90/10 + 5 wt% TRGO and 80/20 + 5 wt% TRGO) were observed to increase from 10^4 to 10^6 compared to their neat counterparts (90/10/0 and 80/20/0). Blending of PS with PMMA led to a minor increase of η^* compared to the individual component systems, especially as the weight content of PMMA was increased from 10 wt% to 20 wt%. The addition of TRGO fillers at 5 wt% and 1 wt% had a more pronounced effect in increasing the complex viscosity of PS than in PMMA. This is attributed to the higher mean number of particles per μm^2 of the TRGO particles in PS in comparison to PMMA as summarized in Table 5.6. Based on the estimated N_p, higher η^* were observed for 90/10 + 5 wt% TRGO and 90/10 + 1 wt% TRGO in comparison to the 80/20 + 5 wt% TRGO and 80/20 + 1 wt% TRGO blends.

Also, judging from the η* values of the blended nanocomposites, it can be concluded that the number of particles/µm² played a more important role in raising the complex shear viscosities of the blends than did the number densities of the droplets.

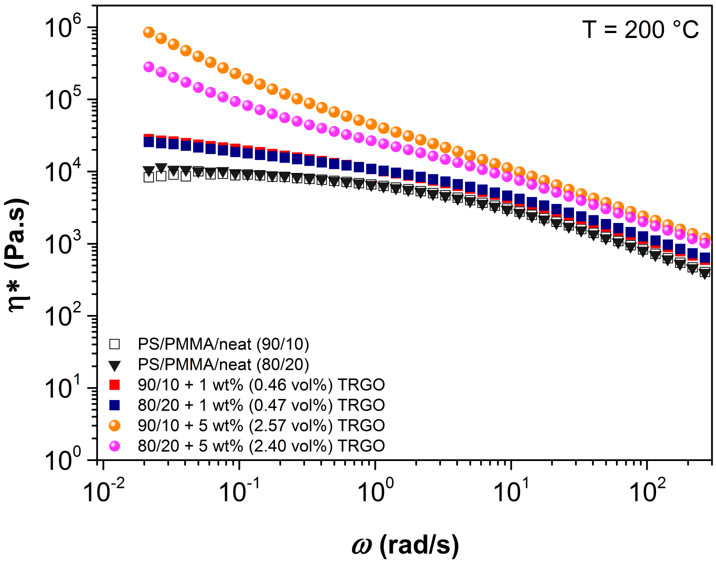

Figure 5.16: Complex shear viscosity as a function of angular frequency for PS/PMMA/TRGO blend nanocomposites at 5 wt% and 1 wt% filler content.

Table 5.6: Number of particles of TRGO in homo- and blended nanocomposites.

PS/PMMA	N_p	PS/PMMA	N_p
100/0 + 5 wt% TRGO	35 µm^{-2}	100/0 + 1 wt% TRGO	10 µm^{-2}
0/100 + 5 wt% TRGO	22 µm^{-2}	0/100 + 1 wt% TRGO	7 µm^{-2}
90/10 + 5 wt% TRGO	29 µm^{-2}	90/10 + 1 wt% TRGO	9 µm^{-2}
80/20 + 5 wt% TRGO	25 µm^{-2}	80/20 + 1 wt% TRGO	7 µm^{-2}

Storage Modulus

Figure 5.17 shows the storage modulus curve for the PS/PMMA/TRGO-blended nanocomposites. Plateaus similar to that observed for the individual components of the blends were also observed in this case at a filler concentration of 5 wt%. At lower filler concentration (1 wt%), there were no observable plateaus, probably because the particle density per µm² was not sufficient to trigger such behaviour in the blended nanocomposites.

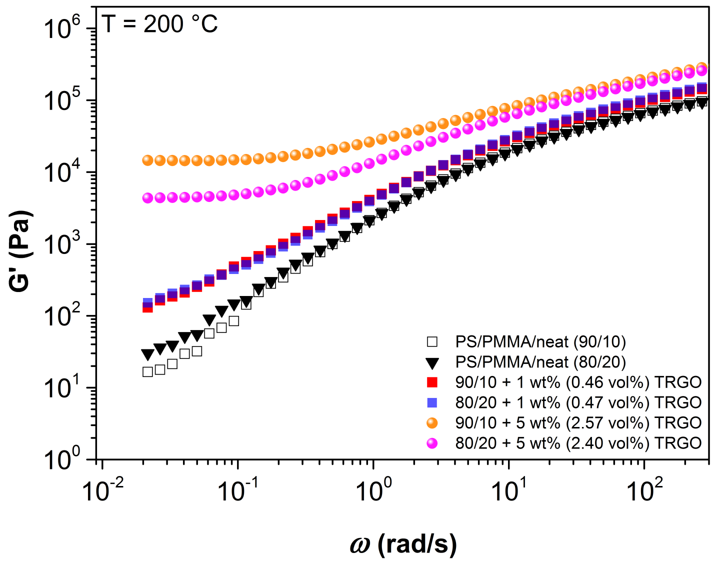

Figure 5.17: Storage modulus as a function of angular frequency for PS/PMMA/TRGO blend nanocomposites at 5 wt% and 1 wt% filler concentration.

Melt percolation threshold formation

A van Gurp-Palmen plot showing the percolation network formation of TRGO particles in the blend systems is illustrated in Figure 5.18. The phase angle curves of the unfilled polymer systems, which fell between 80° and 90° as $/G^*/$ decreased, indicate that they have more viscous characteristics. In other words, they are less elastic.

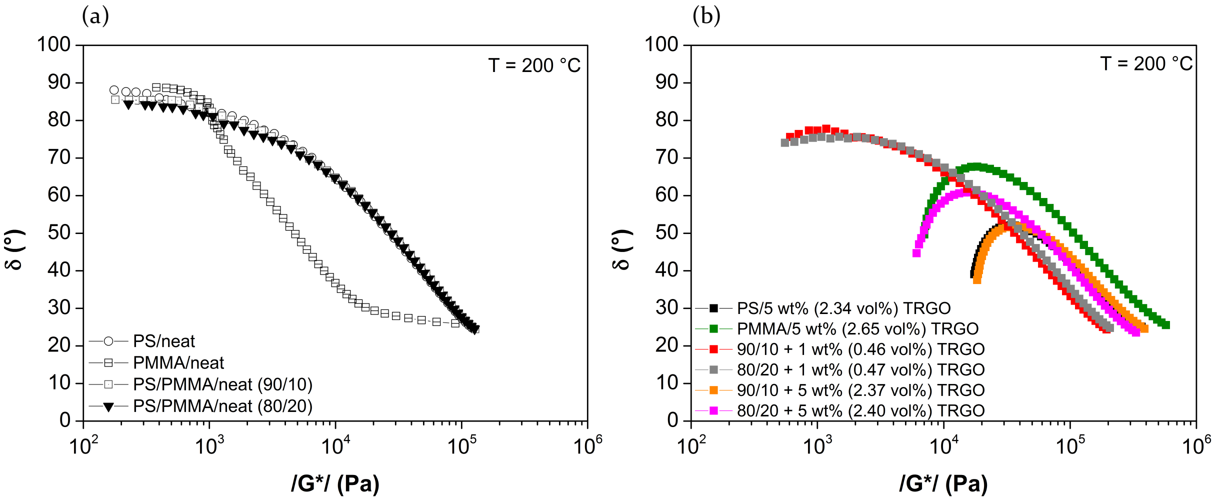

Figure 5.18: van Gurp-Palmen plot of (a) unfilled homo and blended nanocomposites and (b) filled nanocomposites at 5 wt% and 1 wt% filler concentration.

At 5 wt%, all nanocomposite systems exhibited maximums indicative of the particle percolation network as $/G^*/$ decreased to lower values. The elasticity of the respective blend systems currently being investigated ranked in descending order was as follows: 90/10/5 > 100/0/5 > 80/20/5 > 0/100/5. Likewise, the phase angles of 90/10/1 (δ = 73°) and 80/20/1 (δ = 74 °) blends indicate a more elastic flow behaviour compared to the neat nanocomposites.

5.3.4 Conclusion on dynamic shear rheology of the respective nanocomposites

The following conclusions could be drawn from the dynamic shear viscosity studies of the respective nanocomposites:

- The inclusion of TRGO in the homopolymer and blended nanocomposites of PS and PMMA caused them to behave more like elastic solids as opposed to the viscous characteristic behaviour of unfilled polymers. This means that, at a filler content of 5 wt%, a rheological threshold was achieved as evidenced by the display of maximums in the van-Gurp-Palmen-plot.
- Due to the more elastic nature displayed by nanocomposites filled with TRGO in comparison to nanocomposites of talc and CB, it can be expected that nanocomposite foams fabricated with TRGO as the nucleating agent will generate well stabilized smaller cell sizes due to suppressed cell growth. Also, the higher number of particles estimated for TRGO is expected to yield foams with higher cell densities in comparison to talc and CB foams.
- The number of particles per µm^2 of TRGO fillers contribute more to elevating the viscoelastic properties (η^*, G', δ) than the droplet densities of the dispersed phase (PMMA) in the blends.

5.4 Bonding characteristics of fillers to polymer matrix

One of the objectives of this study was to investigate the effect of the nature of the interfacial bonding between the respective fillers and the polymer matrices in order to be able to predict the foaming behaviour of the nanocomposites under deformational stresses. As mentioned earlier in chapter 2 (section 2.3.4), an ideal foam nucleating agent should not severely bond to the polymer matrix [148] in order to nucleate well and at faster rates. One of the methods used to examine the bonding nature of the fillers to the polymer matrices was to carry out a tensile test. Afterwards, the microstructures of the nanocomposite tensile specimens were examined under a scanning electron microscope. It is, however, acknowledged that the bonding behaviour of the fillers to the polymer matrix in the solid state might be different to that in the melt state. Nevertheless, a tensile test done in solid state remains a useful means to examine filler-matrix interaction.

5.4.1 Bonding characteristics of fillers to PS matrix

The tensile test results of the PS nanocomposites are shown in Figure 5.19. The tensile modulus (E) of PS/neat was found to be 3360 ± 92 MPa. While the addition of CB particles did not lead to any change of E at any given filler content, a 2 % increase was achieved by the addition of talc at 1 wt%. The greatest improvements were realized with TRGO with 13 % being the maximum achieved at a content of 1 wt%. A 5 % increase of the tensile strength (σ_m) of PS/neat (55 ± 2 MPa) was achieved with talc at all load rates. This increase is attributed to the good interfacial adhesion of talc to the PS matrix as shown in Figure 5.20.

CB nanoparticles, on the other hand, caused the σ_m to decrease by approximately 6 % at 1 wt% filler concentration. This negative effect is ascribed to the weak interfacial adhesion of the CB particles to the matrix. The CB nanoparticles can be seen to partly detach from the matrix along the interface. The largest decline of the σ_m by 13 % was observed with TRGO at a load-rate of 1 wt. %. Close examination of the SEM image in Figure 5.20c shows that the TRGO platelets appear to debond from the matrix, thereby creating micro-voids between the platelets and the matrix. Similar observations where the tensile strength of PS was decreased by TRGO have also been reported elsewhere [210].

Significant improvements of the elongation at break (ε_b) of PS/neat were observed with talc particles. A 30 % to 35 % increase was achieved at load rates of 0.1 wt% to 1 wt%, respectively. As mentioned earlier, this enhancement may be attributed to the good interfacial adhesion between PS and talc particles. Also, a decrease of ε_b by about 5 % to 10 % was observed with CB and this effect can be related to weak adhesion. A similar but more pronounced decrease of ε_b was observed for PS/TRGO nanocomposites. A decrease of 30 % to 35 % at load rates of 0.5 wt% and 1 wt% was recorded with TRGO. Weak interfacial adhesion is probably a consequence of this.

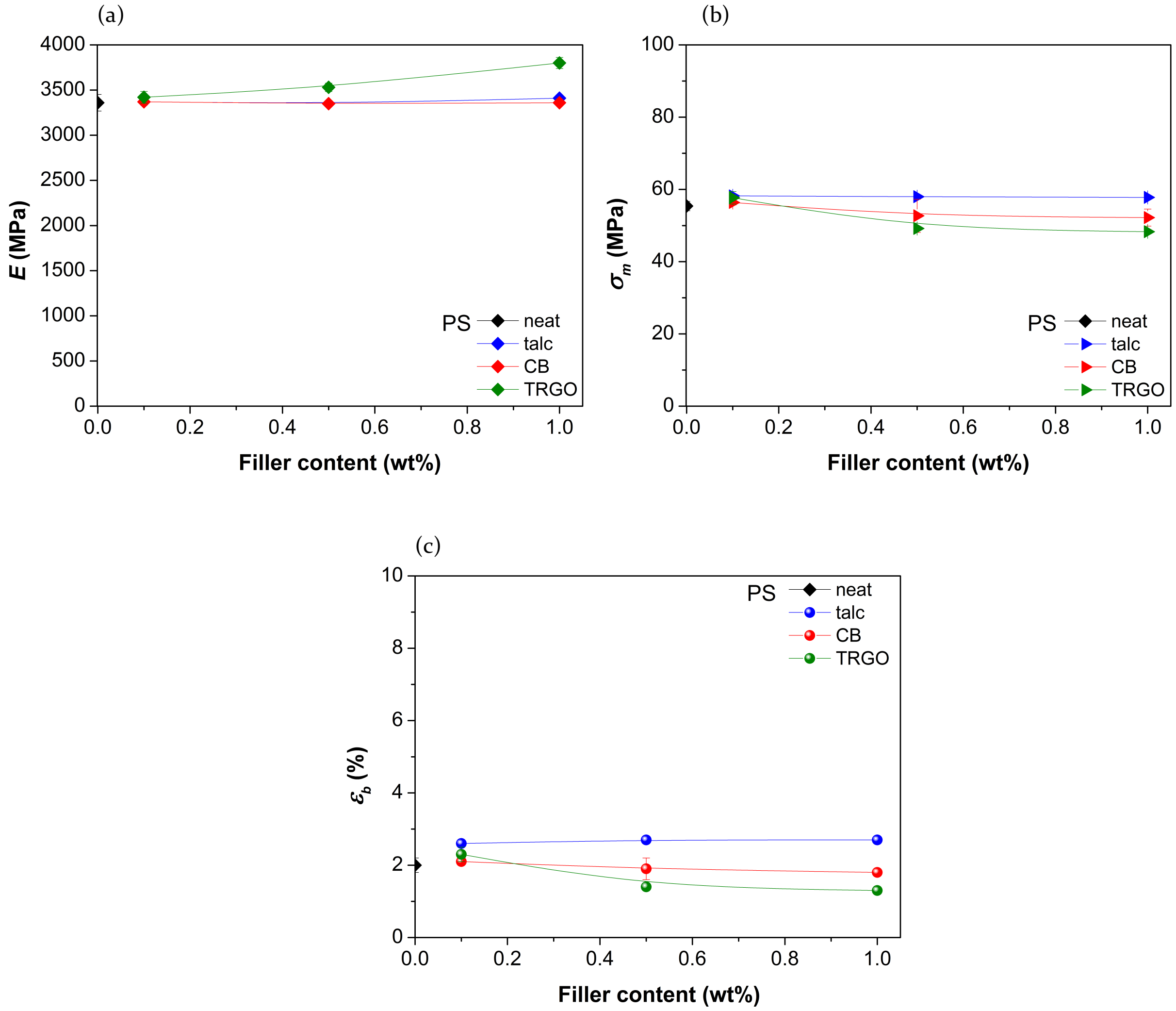

Figure 5.19: Tensile properties of PS nanocomposites (a) tensile modulus (b) tensile strength (c) elongation at break.

Talc particles can be seen to properly adhere to the matrix while CB and TRGO particles were observed to be weakly-bonded to the matrix. The bonding characteristics of the fillers to the matrix can be used to predict the foaming behaviour of the respective nanocomposites. PS/talc nanocomposite foams are expected to generate foams with lower nucleation densities in comparison to nanocomposite foams prepared with CB and TRGO.

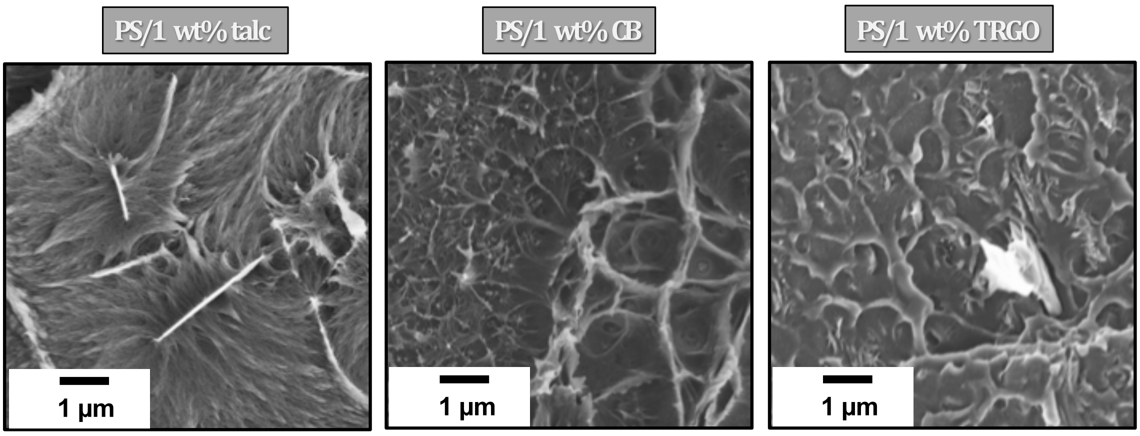

Figure 5.20: SEM microstructural images of PS nanocomposites showing filler-polymer bonding characteristics after tensile test.

5.4.2 Bonding characteristics of fillers to PMMA matrix

Figure 5.21 depicts the measured tensile properties of PMMA nanocomposites filled with talc, CB and TRGO particles. The E of PMMA/neat (3470 ± 54 MPa) was marginally increased by 3% by the addition of 1 wt% of talc. A minor increase of E by 2 % was observed with CB at all prepared filler concentration. A more significant increase of 6 % was realized with TRGO at a load rate of 0.5 wt% and a maximum increase of 11 % was achieved at 1 wt%.

The tensile strength of the PMMA/neat (73 ± 1 MPa) remained more or less the same with the addition of talc. A 6 % and 9 % decrease of the σ_m was observed by the inclusion of CB and TRGO, respectively. These declines are ascribed to the weak interfacial adhesion of the aforementioned fillers to the PMMA matrix as shown in Figure 5.22. A "pull out" effect was especially seen for CB nanoparticles which led to the creation of micro-voids. These microvoids restrain effective transfer of load from the matrix to particles and vice-versa.

The elongation at break was also seen to decrease with the incorporation of the respective fillers owing to poor interfacial interaction between the fillers and PMMA (5.22). At a load rate of 1 wt%, a decline of the ε_b was seen in ascending order to be 11 % for talc, 30 % for CB and 46 % for TRGO. From figure 5.22, it can be seen that all three fillers exhibited weak interfacial bonding to the PMMA matrix, especially CB nanoparticles. Of all three fillers, talc was seen to have better adhesion even though it was still weakly bonded to the matrix. It is interesting to note that, in comparison to PS, the fillers were weakly bonded to PMMA judging from the SEM images. From the bonding behaviour exhibited by the respective fillers, it can be expected that the nucleation densities of foams prepared from these nanocomposites would not be considerably different from one another.

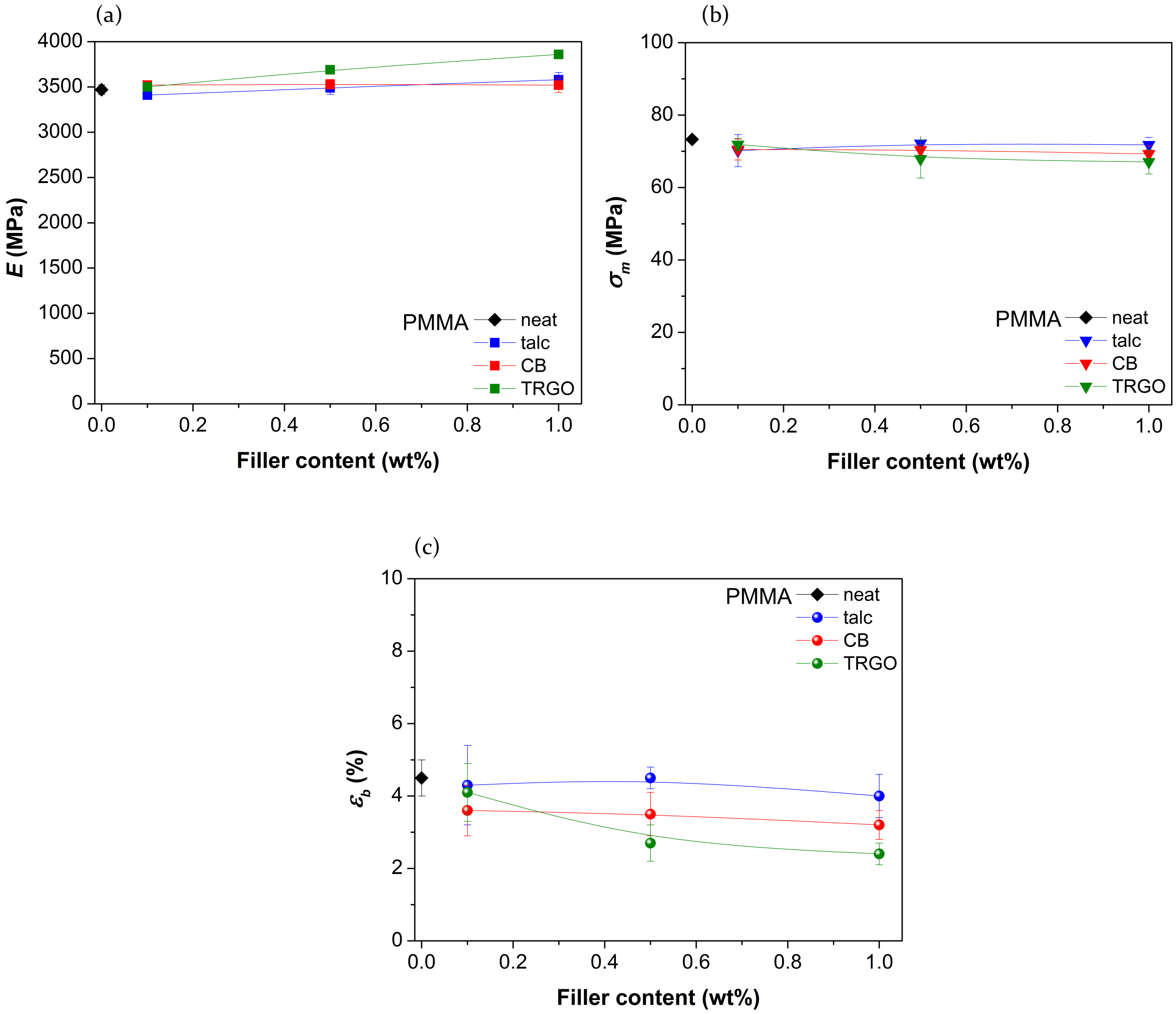

Figure 5.21: Tensile properties of PMMA nanocomposites (a) tensile modulus (b) tensile strength (c) elongation at break.

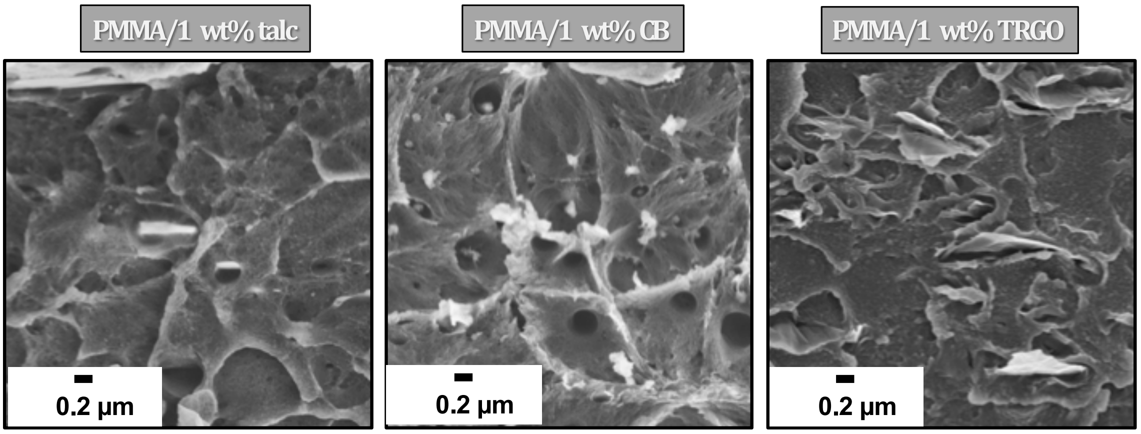

Figure 5.22: SEM microstructural images of PMMA nanocomposites showing filler-polymer bonding characteristics after tensile test.

5.4.3 Bonding characteristics of fillers to PS/PMMA blend matrix

The results of the tensile test of the prepared nanocomposite blends are presented together with the unfilled systems in Figure 5.23. The *E* of PS/neat (3360 ± 93 MPa) was improved by approximately 4% as PS was blended with 10 wt% and 20 wt% of PMMA. The inclusion of TRGO fillers into the blends further enhanced the tensile modulus. The highest increments of 10 % and 11 % were achieved at a filler content of 1 wt% for the 90/10 and 80/20 blends. An obvious decrease of the tensile strength of the blends by about 6 % was seen as the filler concentration was raised to 1 wt% in both blend systems (90/10 and 80/20). Still, in comparison to the unfilled blends, the elongation at break was also observed to decrease as the load rates of TRGO were raised. A maximum decrease of 17 % and 15 % were observed at 1 wt% for 90/10 and 80/20 blends respectively.

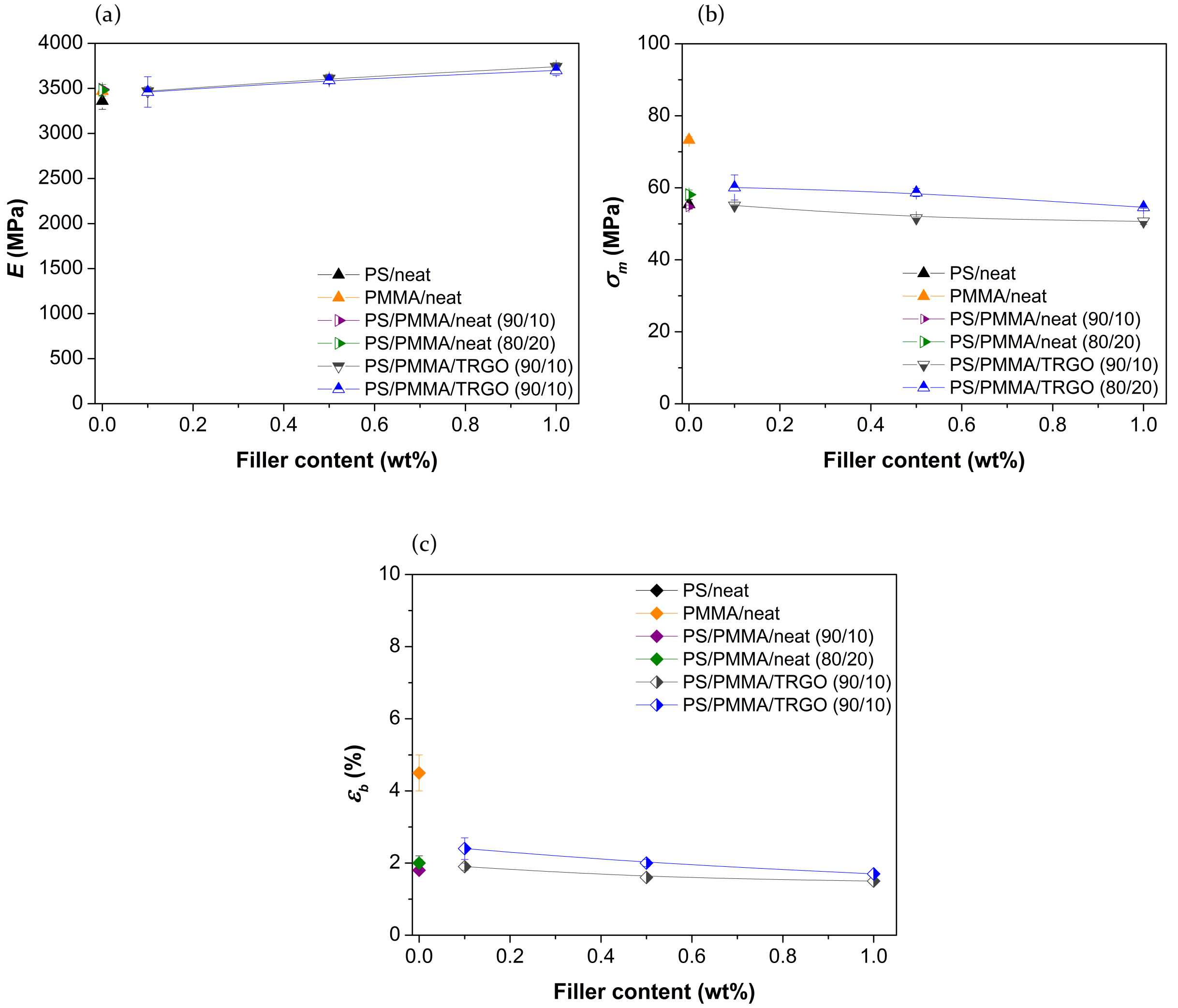

Figure 5.23: Tensile properties of PS/PMMA nanocomposite blends (a) tensile modulus (b) tensile strength (c) elongation at break.

5.4.4 Conclusion on bonding nature of fillers to the polymer matrices

- The fillers used in this study are basically non-reinforcing because of the generally weak interfacial interactions between filler particles and the matrices. A stronger adhesion is required if improvement of the tensile strengths and elongation at break of nanocomposites is desired.
- Talc particles portrayed better adhesion to both PS and PMMA matrices than CB and TRGO, which might lead to nanocomposites foams from talc having lower nucleation and cell densities.
- CB nanoparticles were seen to exhibit better adhesion to PS than PMMA matrix in the SEM microscopic images.

5.5 CO_2 absorption and desorption kinetic experiments

CO_2 sorption and desorption kinetic experiments were carried out for the purpose of estimating the maximum amount of CO_2 that can be dissolved in the selected polymer matrices as well as to obtain information about the gas diffusivity of these systems. These data will be helpful to determine the optimum foam processing parameters to achieve the best results in terms of cell size, cell density, foam density or volume expansion ratio, etc.

To perform these solubility kinetic studies, compression-moulded rectangular plate specimens of the respective nanocomposites were used. The specimens were saturated with CO_2 until equilibrium was achieved. The equilibrium saturation concentration (M_0) was obtained by extrapolating to zero a linearly-fitted plot of M_t versus $\sqrt{t^{1/2}}$ as exemplified in Figure 2.16b. By assuming that the thickness of the specimens (L) did not change during and after saturation, Fick's second law of diffusion could be applied to allow the extraction of the coefficients (D_d) from the slope of the respective curves using equation 2.18.

The results of the kinetic experiments, which are summarized in Table 5.7, clearly show that PMMA nanocomposites absorbed almost twice as much CO_2 as PS nanocomposites (9 %). This confirms the high absorption capacity of PMMA owing to the bonding of its carbonyl oxygen moiety to CO_2. Additionally, the increase of PMMA content from 10 wt% to 20 % led to an increase of the CO_2 from 13 % to 25 %. On the other hand, the diffusion coefficients were observed to be slightly higher in PMMA nanocomposites than in PS nanocomposites.

Further analysis of the results shows that nanocomposites prepared with platelet-like particles such as talc and TRGO exhibited lower D_d than when spherical particles like CB were used. A good reason for this could be that the platelets were able to form a longer tortuous path within the polymer matrix. Also, blending of PS/neat with 10 wt% and 20 wt% of PMMA (90/10 and 80/20) led to a decrease of the D_d by approximately 32 % and 29 %, respectively. In general, the nanocomposites with lower D_d generated foams with lower foam densities; i.e. foams with higher volume expansion ratios.

Table 5.7: Maximum solubility and diffusion coefficients of CO_2 in the prepared nanocomposites.

Sample	$\boldsymbol{M_0}$	$\boldsymbol{D_d}$ (cm^2/min)
	PS nanocomposites	
Neat	9.4	2.45×10^{-3}
0.1 wt % talc	9.8	2.45×10^{-3}
0.5 wt % talc	9.7	1.77×10^{-3}
1.0 wt % talc	9.6	1.48×10^{-3}
0.1 wt % CB	9.5	1.52×10^{-3}
0.5 wt % CB	9.6	1.60×10^{-3}
1.0 wt % CB	9.6	1.72×10^{-3}
0.1 wt % TRGO	9.5	1.58×10^{-3}
0.5 wt % TRGO	9.6	1.59×10^{-3}
1.0 wt % TRGO	9.6	1.30×10^{-3}
	PMMA nanocomposites	
Neat	21.0	2.74×10^{-3}
0.1 wt % talc	20.9	2.76×10^{-3}
1.0 wt % talc	19.6	1.91×10^{-3}
0.1 wt % CB	20.9	2.76×10^{-3}
1.0 wt % CB	20.8	2.85×10^{-3}
0.1 wt % TRGO	20.9	2.70×10^{-3}
1.0 wt % TRGO	19.0	1.71×10^{-3}
	PS/PMMA nanocomposite blends	
90/10	10.7	1.61×10^{-3}
90/10 + 0.1 wt% TRGO	10.6	1.55×10^{-3}
90/10 + 1.0 wt% TRGO	10.7	1.55×10^{-3}
80/20	11.8	1.72×10^{-3}
80/20 + 0.1 wt% TRGO	11.4	1.73×10^{-3}
80/20 + 1.0 wt% TRGO	11.4	1.58×10^{-3}

L = 0.2 cm; all M_0 values have a standard deviation of ± 0.02.

5.6 Nanocomposite batch foams

Initially, a two-step temperature induced ($\Delta T/\Delta t$) batch foaming technique was used to foam the nanocomposite specimens, but the densities of foams realized were somewhere between 450 kg/m^3 and 600 kg/m^3. Irrespective of the foaming temperature and foaming time selected, the corresponding cell microstructures of these foams were inhomogeneous as shown in Figure 5.24. Consequently, the pressure-induced ($\Delta P/\Delta t$) method was employed during all subsequent batch foaming experiments.

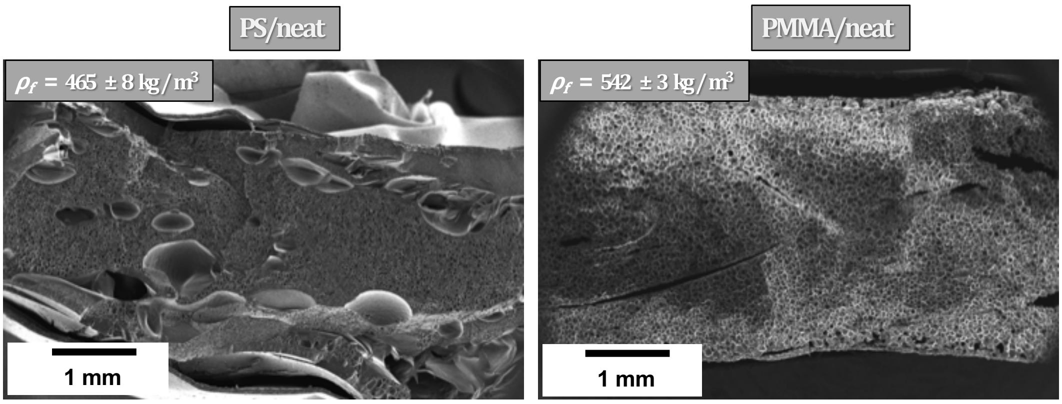

Figure 5.24: Overview of the SEM images of the microstructure of (left) PS/neat and (right) PMMA/neat foams produced using the temperature-induced batch foam method.

5.6.1 PS nanocomposite batch foams

PS nanocomposite foams were prepared with talc, CB and TRGO as heterogeneous nucleating agents and the microstructural overview of foams with 0.1 wt% of the respective fillers are shown as examples in Figure 5.25. All foams prepared were observed to have homogenous structural cellularity. Analysis made with a gas pycnometer revealed the foams to have a closed-cell content of 97 %. Greater detail of the cellular structures of the nanocomposite foams is shown in Figure 5.26. The mean cell size of PS/neat foam (ϕ_m = 21 µm) was decreased in a progressive manner as the load rates of the nucleating agents were raised from 0.1 wt% to 1 wt%. This decrease of ϕ_m was clearly due to the decrease of the Gibbs free nucleation energy barrier caused by the inclusion of the fillers. Specifically, a reduction of the cell size by 38 %, 45 % and 34 % was achieved by talc, CB and TRGO, respectively, at 1 wt% in comparison to the PS/neat foam. The cell size distribution of all prepared PS foams followed the Gaussian distribution (Figure 5.27). It is interesting to see that the mean cell sizes of each individual system remained the same even as the filler load rates were increased, e.g. from 0.5 wt% to 1 wt%. The rheological experiments at filler load rates of 1 wt% showed that PS/TRGO nanocomposites possessed higher elastic melt properties in comparison to nanocomposites of talc and CB. Therefore, it was expected that PS/TRGO foams would generate overall the smallest cell sizes due to suppression of cell growth by the elastic cell walls, but this was not the case. It might be that the complete absence of any form of shear in the melt during batch foaming was responsible for the mismatch. The lower foam densities of PS/TRGO foams overall is associated with the lower diffusion coefficient displayed by the PS/TRGO nanocomposites.

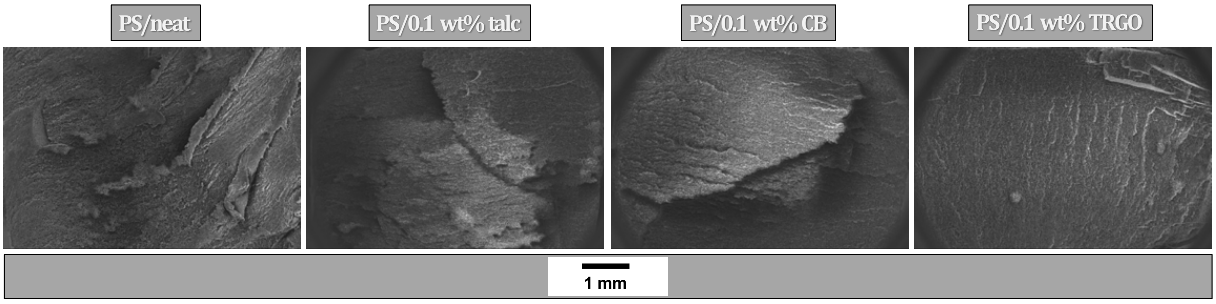

Figure 5.25: SEM micrographs showing the homogenous microstructural overview of PS nanocomposite foams prepared with talc, CB and TRGO nucleating agents.

Additionally, the cell densities (ρ_{cell}) of the nanocomposite foams shown in Figure 5.28 were observed to increase by one order of magnitude in comparison to the PS/neat foam (ρ_{cell} = 5.18 x 10^8 cells/cm^3). Regardless of filler type, no considerable difference in cell densities was observed between the nanocomposite foams. Their ρ_{cell} were within the same order of magnitude (10^9).

The nucleation densities (ρ_{nucl}) of the foams estimated from equation 2.31 are given in Figure 5.28 as well. The results show minor differences but confirms the prediction[73] from the debonding behaviour of the fillers to the matrix. The behaviour of the ρ_{nucl} still followed similar trend as that observed for ρ_{cell}. Maximum ρ_{nucl} values of up to 10^8 were achieved for all foams at a filler content of 1 wt%.

Another important feature that is used to characterize polymeric foams are the cell wall thickness (t_{cw}) and equivalent strut thickness ($t_{s.eq}$) which is depicted in Figure 5.29. The *VER* as well as the cell wall thickness (t_{cw}) and equivalent strut thickness ($t_{s.eq}$) of the nanocomposite foams as a function of filler concentration are presented in Figure 5.30 and Figure 5.31. The highest *VER* was observed for PS/TRGO nanocomposite foams at all concentrations prepared, which was followed by PS/CB and then PS/talc foams. This is associated with the lower CO_2 diffusion coefficient of PS/TRGO nanocomposites (Table 5.7) in comparison to nanocomposites of talc and CB.
A summary of the PS nanocomposite foam properties is given in Table 5.8.

---

[73] That fillers which adhere strongly to the polymer matrix may lead to foams with lower nucleation densities.

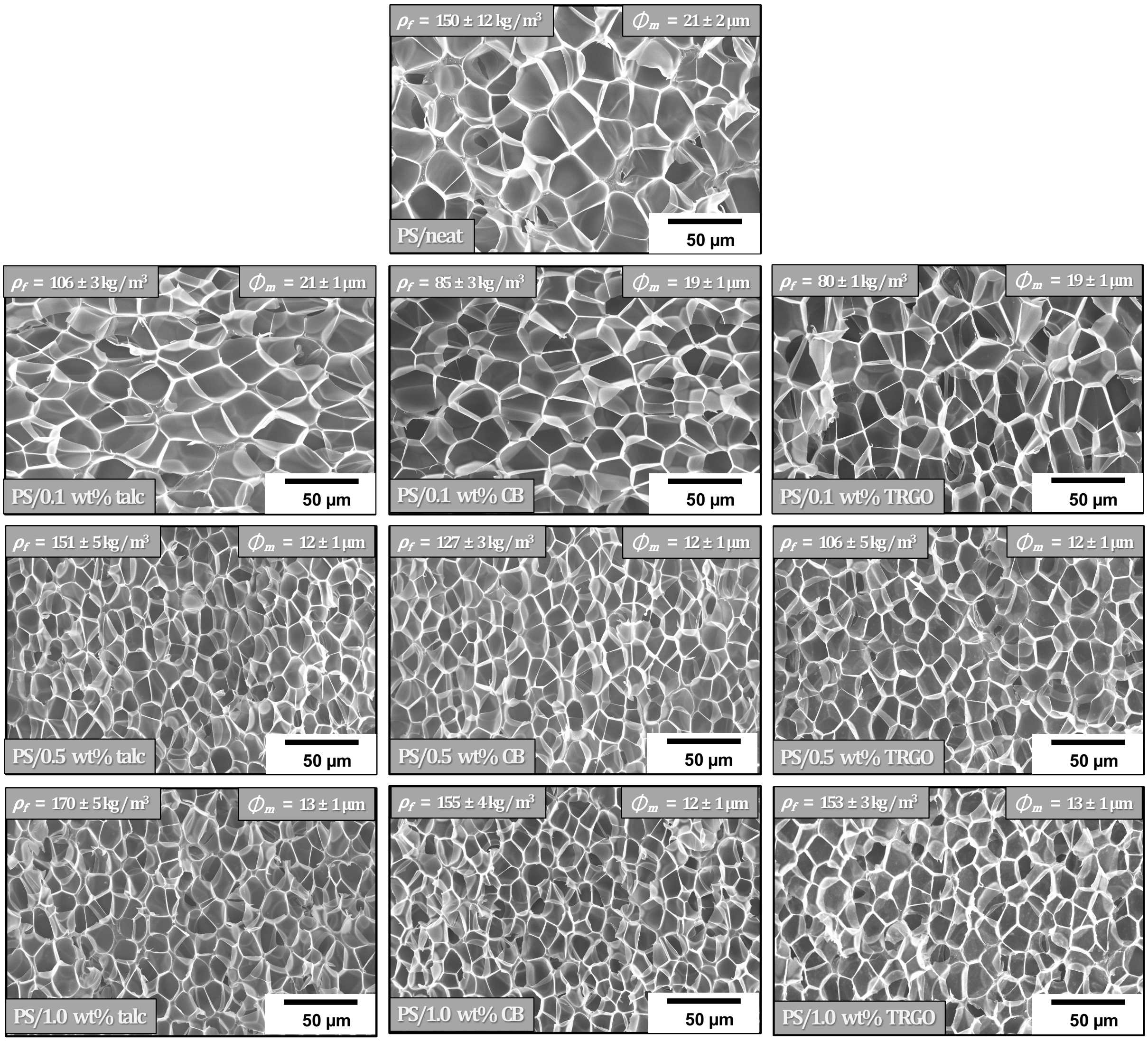

Figure 5.26: Cell morphology of PS nanocomposite foams showing their respective mean cell sizes and foam densities.

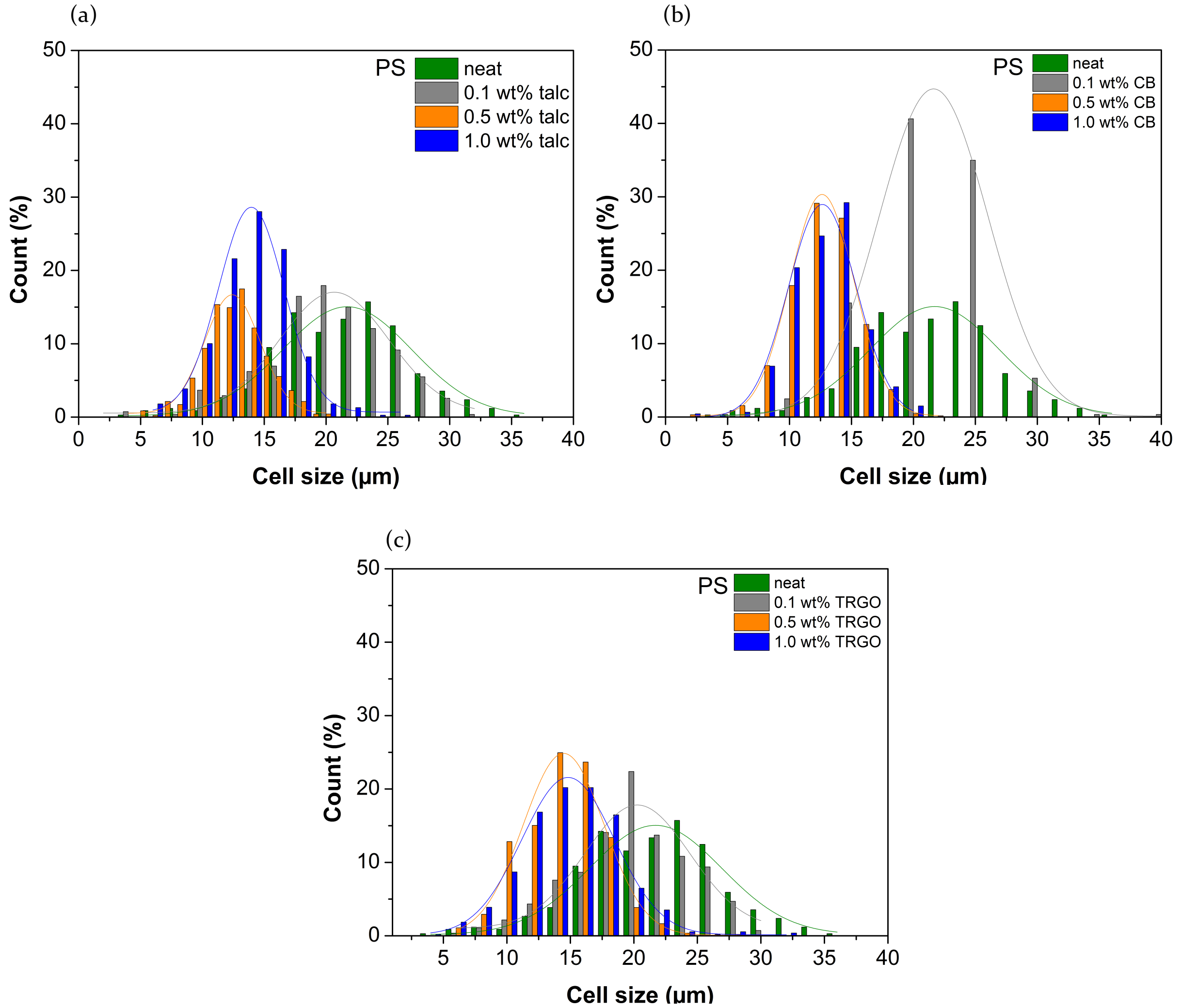

Figure 5.27: Cell size distribution of PS nanocomposite foams with densities in the range of 80 kg/m^3 and 170 kg/m^3.

Table 5.8: Summary of foam properties of PS nanocomposite foams processed via batch foaming.

Sample	Density (kg/m^3)	*VER*	Mean cell size (µm)
PS/neat	150 ± 12	7.0	21 ± 2
PS/0.1 wt% talc	106 ± 3	9.9	21 ± 1
PS/0.5 wt% talc	151 ± 5	7.0	12 ± 1
PS/1.0 wt% talc	170 ± 5	6.2	13 ± 1
PS/0.1 wt% CB	85 ± 3	12.4	19 ± 1
PS/0.5 wt% CB	127 ± 3	8.3	12 ± 1
PS/1.0 wt% CB	155 ± 4	6.8	12 ± 1
PS/0.1 wt% TRGO	80 ± 1	13.1	19 ± 1
PS/0.5 wt% TRGO	106 ± 5	9.9	12 ± 1
PS/1.0 wt% TRGO	153 ± 3	6.9	12 ± 1

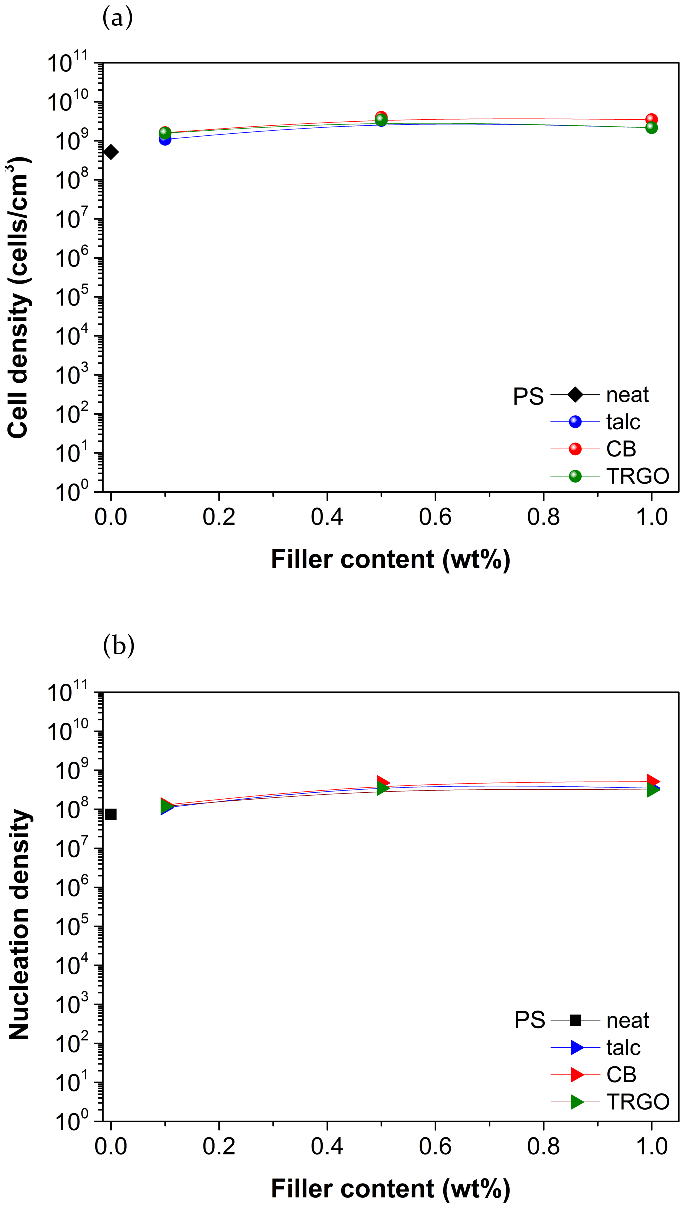

Figure 5.28: (a) Cell densities and (b) nucleation densities of PS nanocomposite foams with densities in the range of 80 kg/m^3 and 170 kg/m^3.

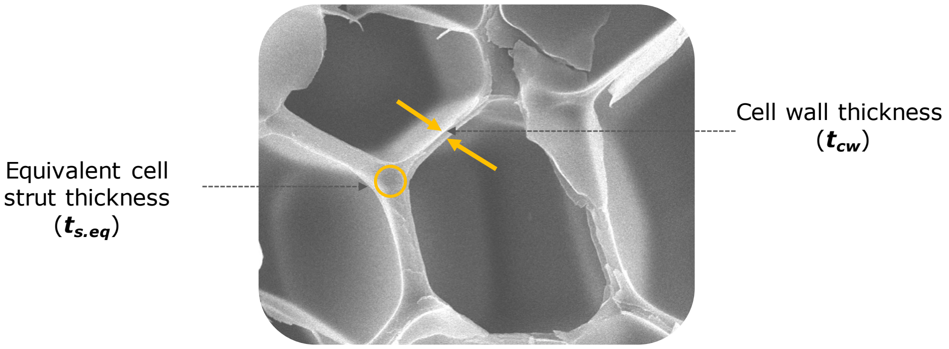

Figure 5.29: Depiction of the cell wall and strut thickness of PS nanocomposite foams.

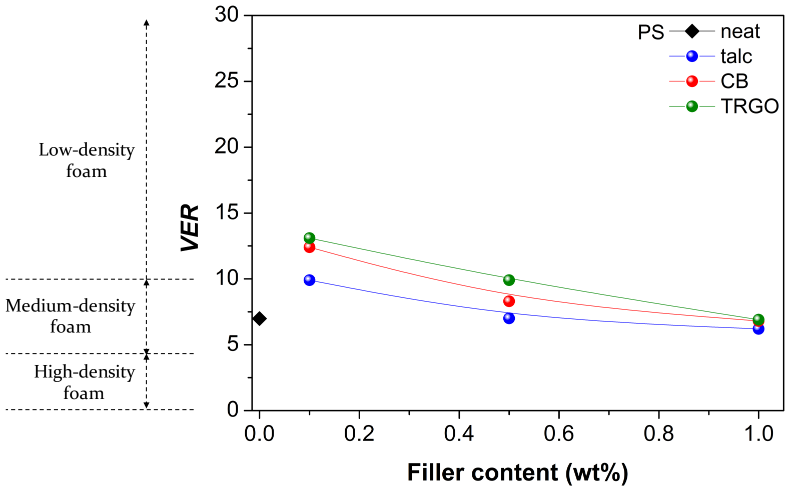

Figure 5.30: Volume expansion ratios of PS nanocomposite batch foams as function of filler concentration.

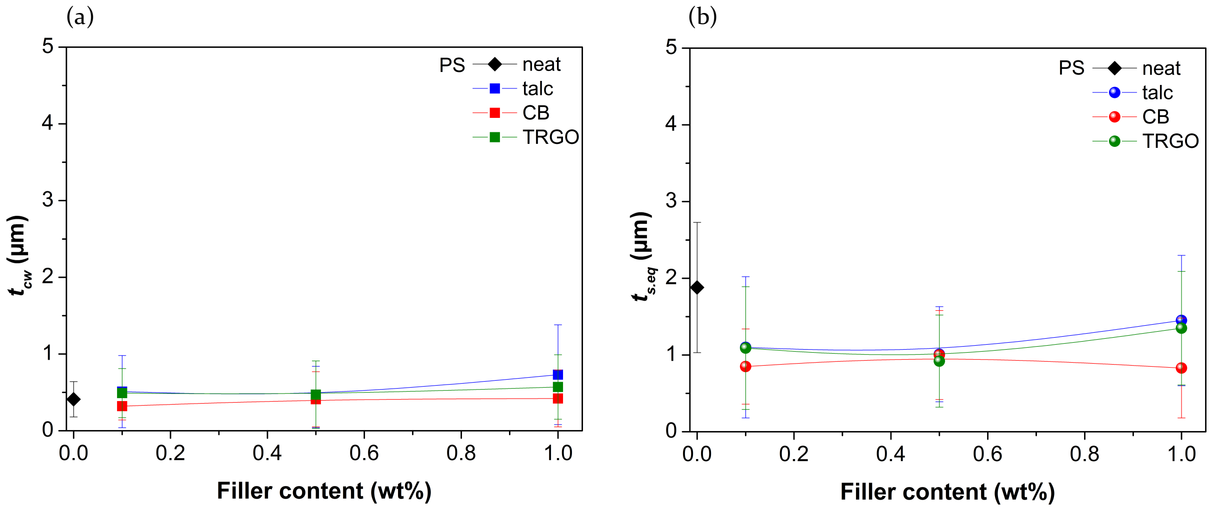

Figure 5.31: (a) Cell wall thickness (b) and equivalent strut thickness of PS nanocomposite batch foams as function of filler concentration.

The following inferences can be drawn from the *VER* results of PS nanocomposite foams:

- The *VER* of the nanocomposite foams decreases as the filler concentration increases.
- A decrease of *VER* increases the t_{cw}.
- A decrease of *VER* increases the $t_{s.eq}$.

The above deductions are supported by other studies [211,212] reported in the literature. Lastly, the nanocomposite foams generated were medium to low density by virtue of their *VER*.

5.6.2 PMMA nanocomposite batch foams

The PMMA nanocomposites prepared with talc, CB and TRGO fillers were foamed and characterized in same way as foams prepared with PS nanocomposites. At all filler concentration, the foams exhibited homogenous cell microstructures as exemplified in Figure 5.32 at a load rate of 0.5 wt%. All foams prepared showed closed cell content of 98 % as revealed by gas pycnometer measurements.

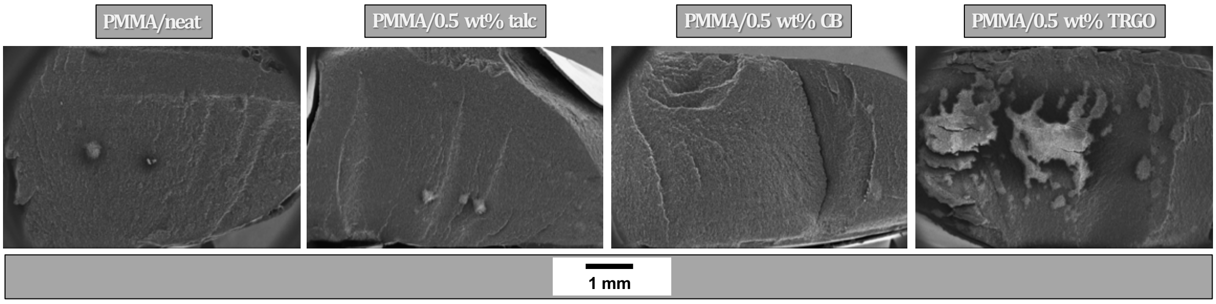

Figure 5.32: SEM micrographs showing the homogenous microstructural overview of PMMA nanocomposite foams prepared with talc, CB and TRGO nucleating agents at low magnification.

As expected, the ϕ_m of the foams in Figure 5.33 was decreased with the introduction of the respective fillers. At a filler content of 1 wt% the mean cell size of PMMA/neat (ϕ_m = 15) was decreased by approximately 33 % with talc particles and by 40 % with CB and TRGO fillers, respectively. Analysis of the cell size distribution (Figure 5.34) showed that the cells conform to a Gaussian distribution. Dynamic shear rheological experiments showed that PMMA/TRGO nanocomposite sat a filler content of 1 wt% exhibited slightly higher elasticity. Therefore, it was expected that foams prepared with PMMA/TRGO nanocomposite would generate smaller cell sizes in comparison to PMMA/CB and PMMA/talc nanocomposite foams. The cell size results did not confirm this expectation as the cell sizes of the nanocomposites were more or less the same. However, the density of the PMMA/TRGO foams was observed to be lower in comparison to others. This might be explained by the fact that the cells are elastic enough to prevent cell coalescence as well as the escape of blowing agent, which is manifested in the cell density values of the respective foams.

The highest ρ_{cell} realized with PMMA nanocomposite foams are in the order 10^9 and the results are presented comparatively in Figure 5.35. The resultant ρ_{nucl} of the foams shown in Figure 5.35b were observed to follow the same trend as ρ_{cell}. As predicted from the debonding characteristics of the respective fillers with the PMMA matrix, the ρ_{nucl} did not differ significantly from one another. In comparison to PMMA/neat foams, ρ_f of about 5 % to 31 % were achieved with the introduction of the respective fillers. These reductions are more pronounced, particularly at filler concentrations of 0.1 wt% and 0.5 wt%.

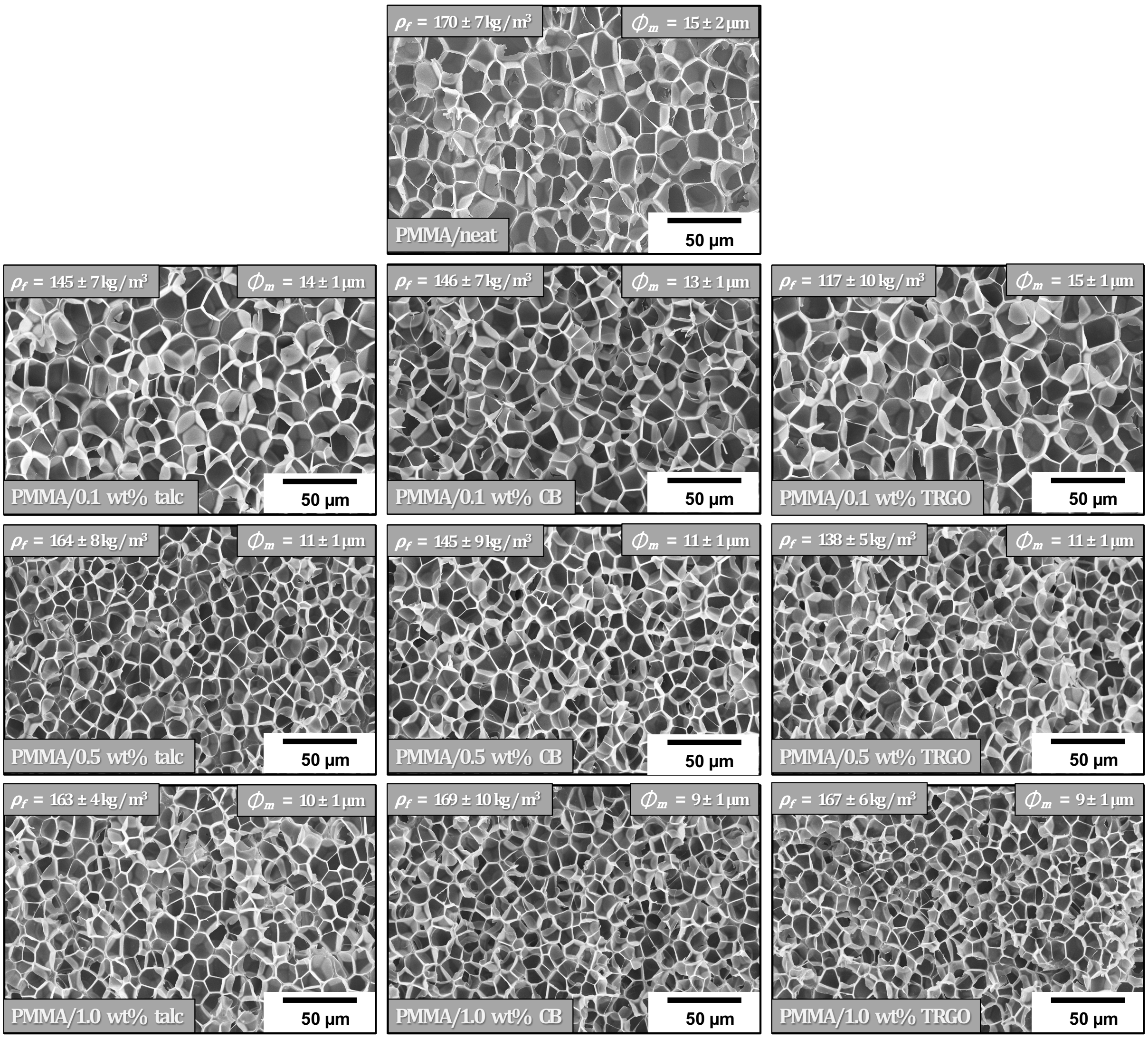

Figure 5.33: Cell morphology of PMMA nanocomposite foams with different nucleating agents.

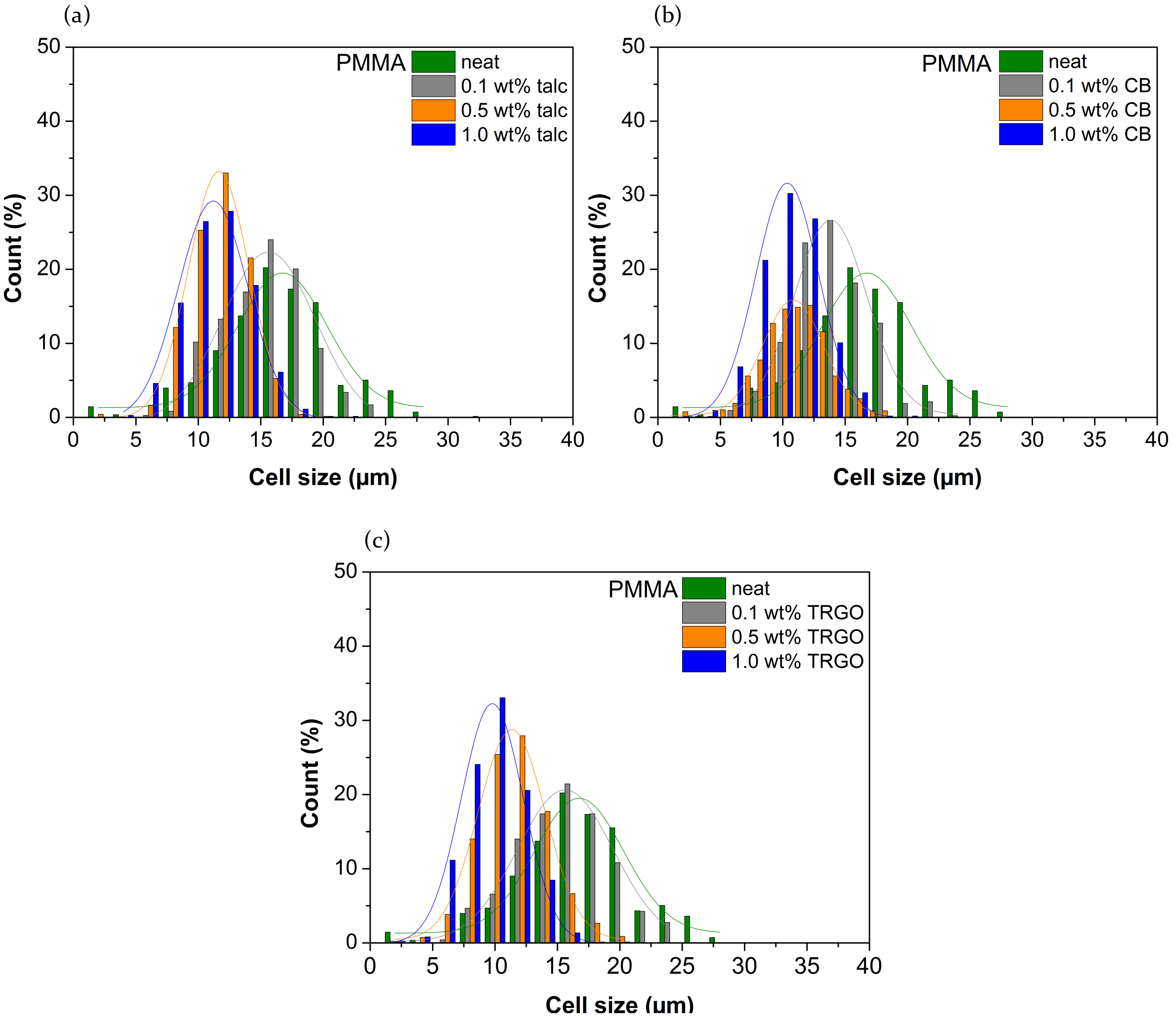

Figure 5.34: Cell size distribution of PMMA nanocomposite foams with different nucleating agents.

Plots showing the relationship between the *VER*, t_{cw} and $t_{s.eq}$. as a function of filler concentration are presented in Figure 5.36 and Figure 5.37, respectively. The highest *VER* was observed for PMMA/TRGO foams in comparison to foams produced with talc and CB, especially at load rates of 0.1 wt% and 0.5 wt%. Again, the higher *VER* is believed to be due to the low diffusion coefficient of the PMMA/TRGO nanocomposites in comparison to that of talc and CB. The geometry and number of particles per µm^2 of TRGO fillers might have formed a longer tortuous path for the gas molecules than talc and CB particles, hence the lower D_d.

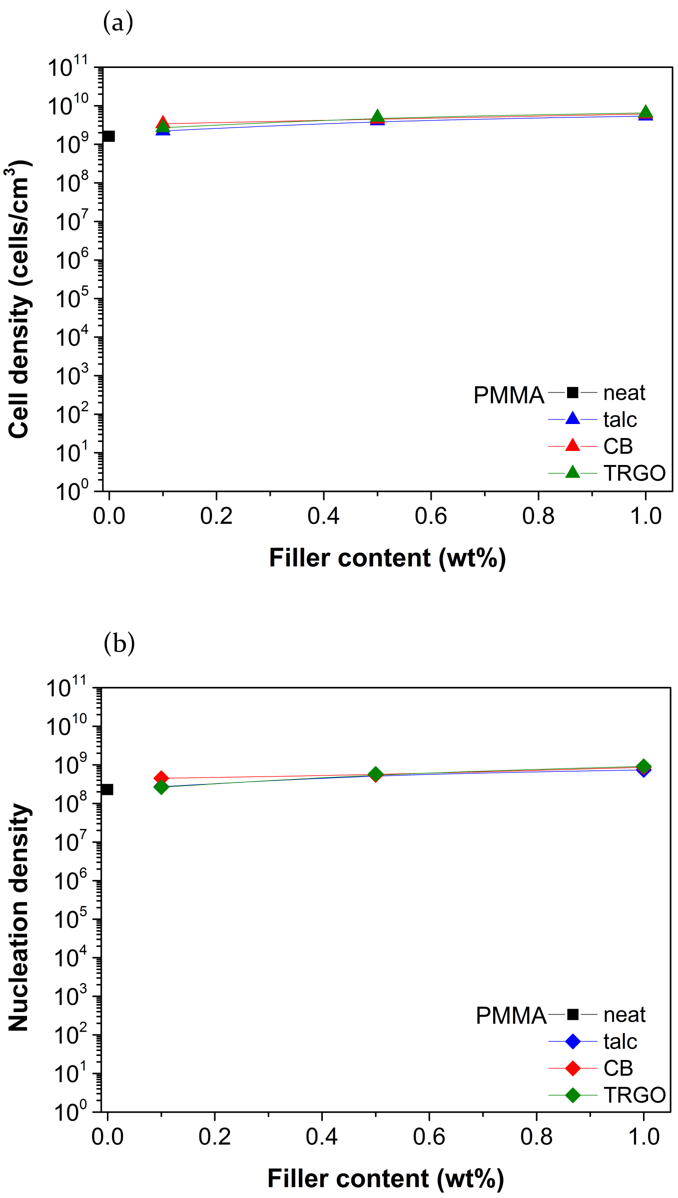

Figure 5.35: (a) Cell densities and (b) nucleation densities of PMMA nanocomposite foams.

The following conclusions can be drawn from Figure 5.36 and Figure 5.37.

- As also observed in PS nanocomposite foams, the *VER* decreased as the filler load rates were raised.
- In contrast to what was observed for PS foams, the decrease of *VER* led to a slight decrease of the t_{cw} and $t_{s.eq}$.

These results are well in agreement with what has been reported in the literature [213].

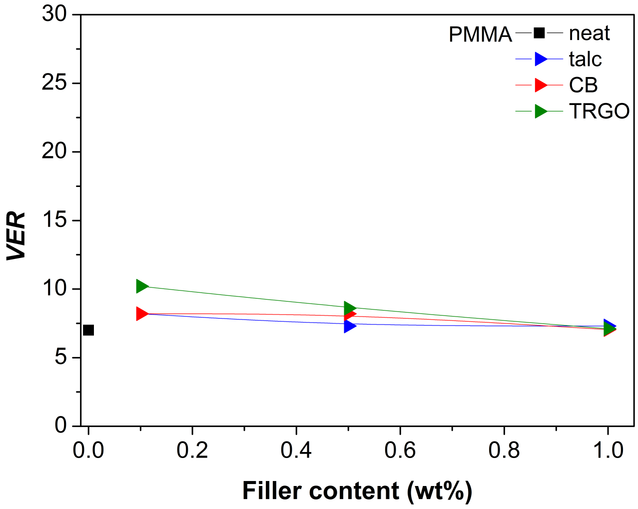

Figure 5.36: Volume expansion ratios of PMMA nanocomposite batch foams as a function of filler content.

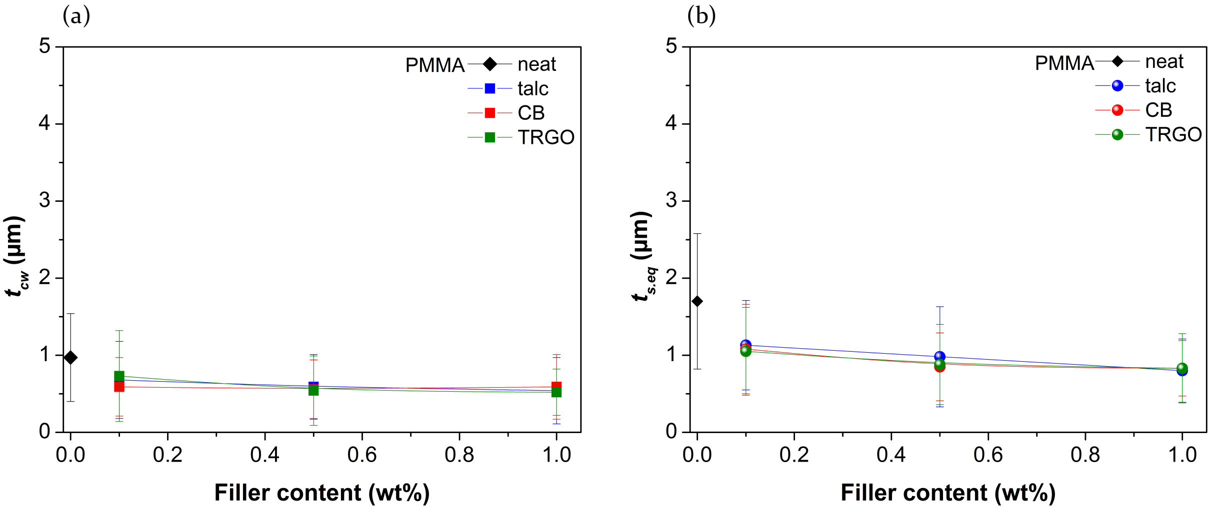

Figure 5.37: (a) Cell wall thickness (b) equivalent strut thickness of PMMA nanocomposite batch foams as a function of filler content.

5.6.3 PS/PMMA blend nanocomposite batch foams

From the comparative batch foam studies of PS and PMMA nanocomposites reported in the previous sub-sections, three important observations were made:

- The PS nanocomposite foams were characterized by high *VER* of up to 14 (low-density foams have *VER* ≥ 10) in comparison to PMMA foams.
- Foams generated with PMMA nanocomposites exhibited smaller mean cell sizes and higher cell and nucleation densities compared to PS nanocomposite foams.
- TRGO fillers have so far been the most effective nucleating agent based on the mean cell sizes and *VER* obtained with PS/TRGO and PMMA/TRGO nanocomposite foams.

In conclusion from the results on PS and PMMA foams, combining PS and PMMA to make blends that will be nucleated by TRGO particles should realize microcellular low-density foams.

Blends (PS/PMMA/TRGO) of the following compositions in weight: 90/10 and 80/20 were foamed with the same processing conditions as PS and PMMA nanocomposite foams. An overview of the foam microstructures and cell morphologies is presented in Figure 5.38 and Figure 5.39, respectively. The foams generated showed homogenous cell structures and they followed the Gaussian distribution as shown in Figure 5.40. A closed-cell content of 95 % was achieved for all foams prepared.

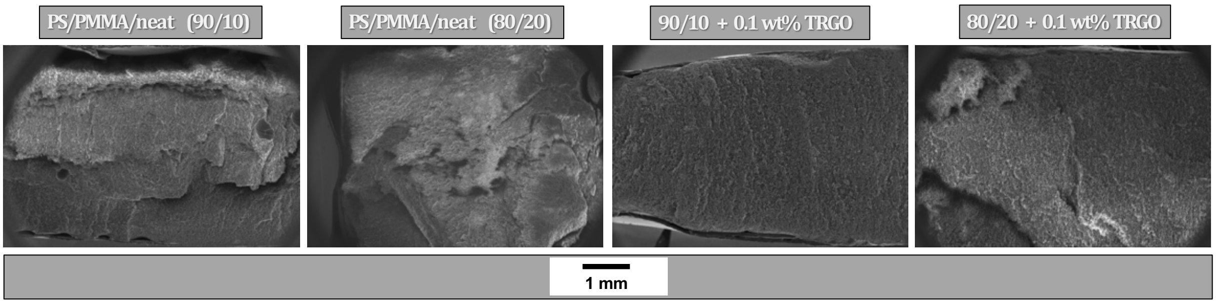

Figure 5.38: SEM images showing the homogenous microstructural overview of PS/PMMA nanocomposite foams prepared using TRGO nucleating agent.

The mean cell size ($\phi_m = 16$ µm) of the neat blend foam (90/10) was decreased by 19 % and 37 % at filler (TRGO) content of 0.5 wt% and 1 wt%. Also, the mean cell size ($\phi_m = 16$ µm) of the neat 80/20 blend foam remained more or less unchanged at a load rate of 0.5 wt% and 1 wt%, respectively. It is interesting to observe that the 90/10 and 80/20 share the same ϕ_m but their densities differ significantly. For instance, the density of 90/10 was found to be 121 kg/m^3 while that of 80/20 was 97 kg/m^3. Even at higher filler content (1 wt%), the density of the 80/20 blend foam (87 kg/m^3) was much less than that of 90/10 (110 kg/m^3). This reduction in the foam densities by raising the PMMA content from 10 wt% to 20 wt% is due to the additional CO_2 absorption by PMMA.

The ρ_{cell} and ρ_{nucl} of the blend nanocomposite foams (Table 5.9) were observed to be slightly higher than that of the individual foams (PS and PMMA). Nonetheless, the values are still within the same order of magnitude (10^9). Overall, the 90/10 nanocomposite foams exhibited higher ρ_{cell} and ρ_{nucl} than 80/20. This is related to the higher average density of the dispersed phase droplets (PMMA) in the 90/10 than in the 80/20 nanocomposite blends.

Low-density foams were produced as shown in Figure 5.41. As expected, the blends show foams with higher VER (12–15) than both PS (7–13) and PMMA (7–10) nanocomposite foams at all filler contents. Also, the VER of the blend foams was seen to decrease as the filler concentration decreased.

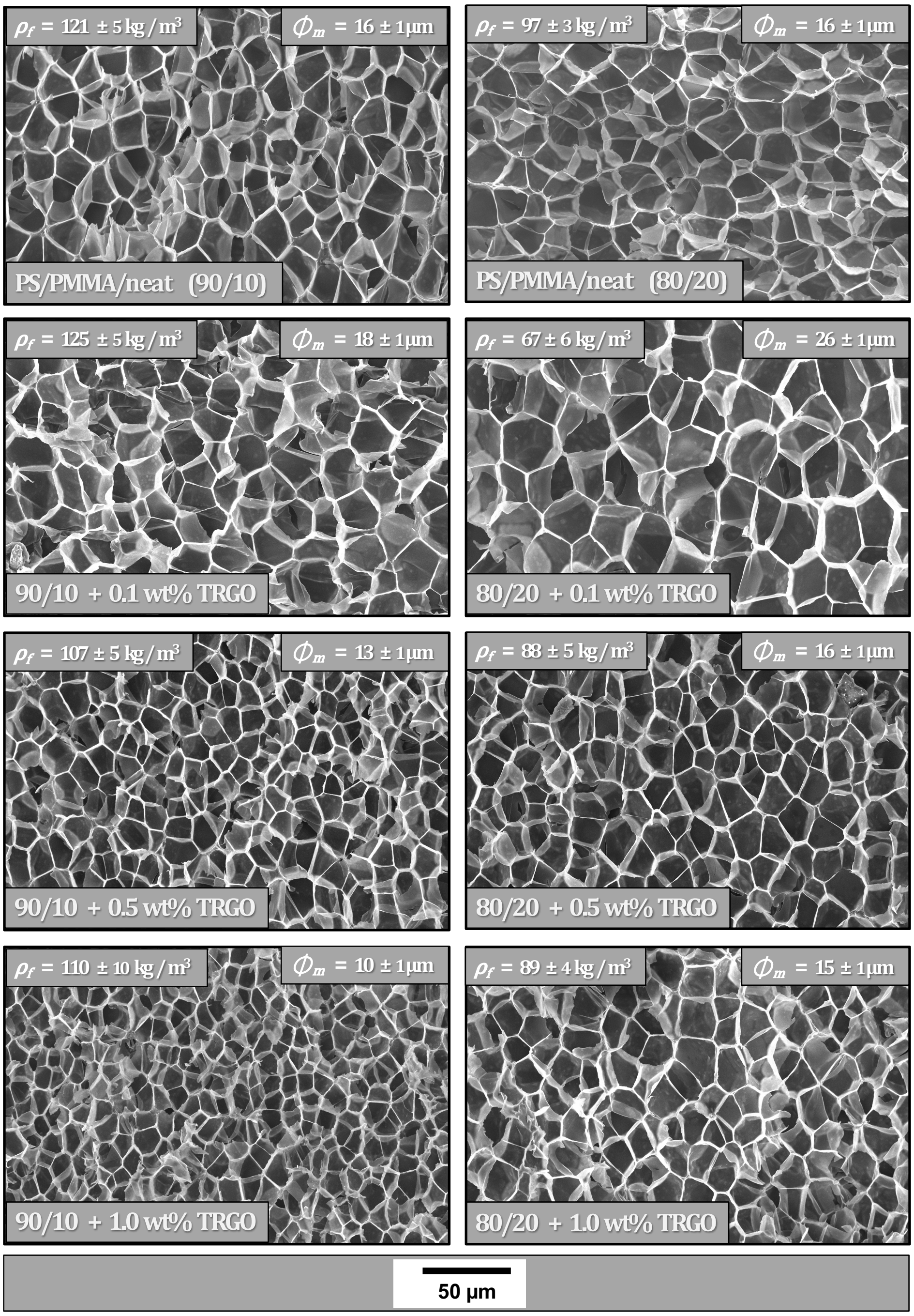

Figure 5.39: Cell morphology of PS/PMMA blend nanocomposite foams showing their respective mean cell sizes and foam densities.

The t_{cw} and $t_{s.eq}$ as a function of filler concentration are presented in Figure 5.42. The t_{cw} and $t_{s.eq}$ were slightly increased as the load rates of the fillers were increased; i.e. $VER \downarrow = t_{cw} \nearrow$; $VER \downarrow = t_{s.eq} \nearrow$. These characteristics are similar to what was observed for PS nanocomposite foams.

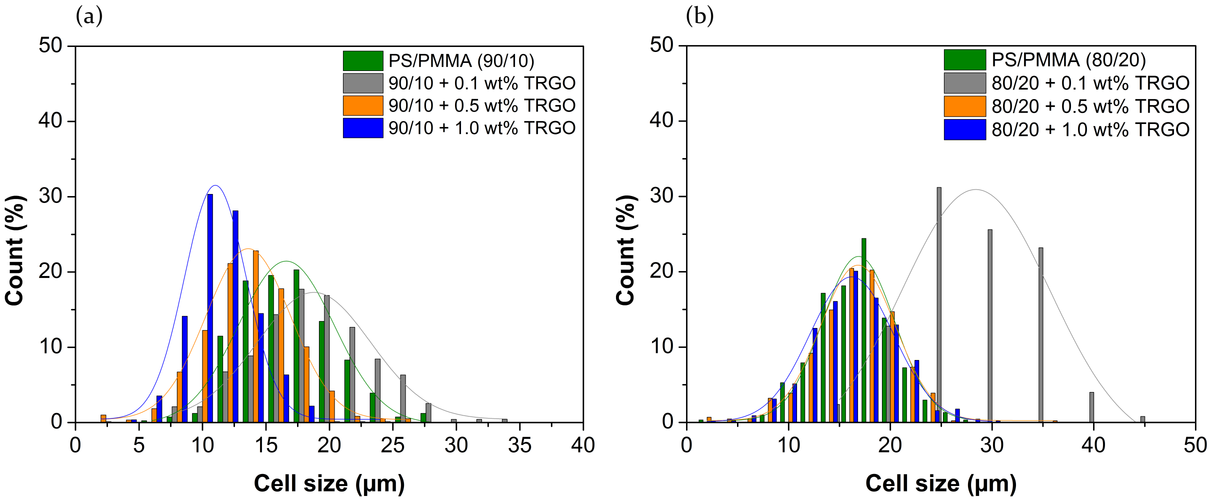

Figure 5.40: Cell size distribution of PS/PMMA blend nanocomposite foams.

Table 5.9: Summary of cell and nucleation densities of the blend nanocomposite foams.

Sample	ρ_{cell} (cells/cm^3)	ρ_{nucl}
PS/PMMA/neat (90/10)	1.94×10^9	2.20×10^8
PS/PMMA/neat (80/20)	2.33×10^9	2.10×10^8
PS/PMMA		
90/10 + 0.1 wt% TRGO	2.21×10^9	2.30×10^9
90/10 + 0.5 wt% TRGO	3.88×10^9	3.92×10^9
90/10 + 1.0 wt% TRGO	6.50×10^9	6.77×10^9
80/20 + 0.1 wt% TRGO	8.66×10^8	5.38×10^7
80/20 + 0.5 wt% TRGO	2.83×10^9	2.30×10^8
80/20 + 1.0 wt% TRGO	2.90×10^9	2.40×10^8

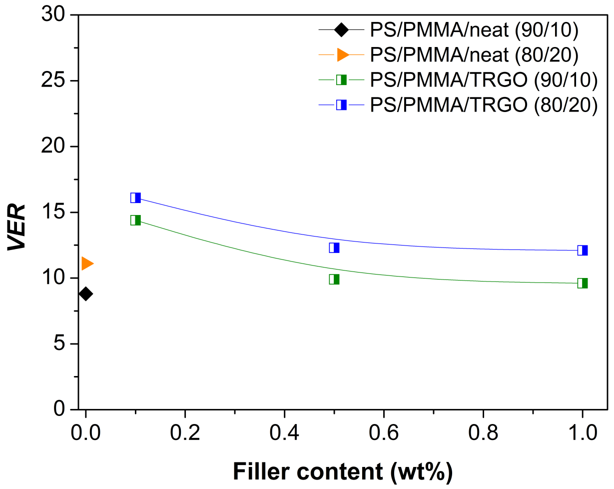

Figure 5.41: Volume expansion ratios of PS/PMMA blend nanocomposite batch foams as a function of filler content.

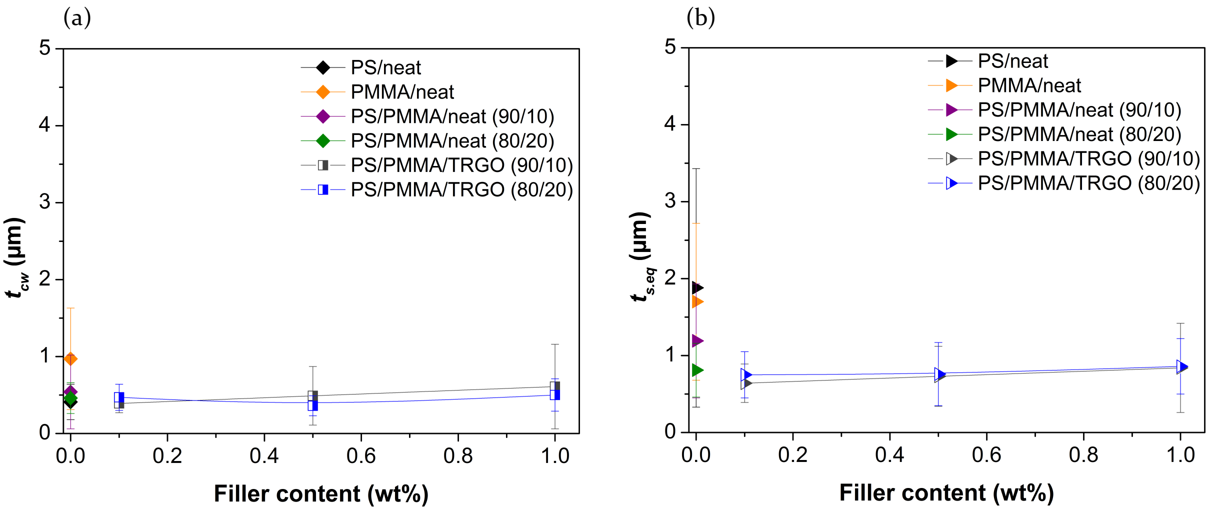

Figure 5.42: Cell wall and equivalent strut thicknesses of PS/PMMA blend nanocomposite batch foams as a function of filler content.

5.6.4 Conclusion on nanocomposite batch foams

From the comparative batch foam studies of PS and PMMA nanocomposites reported in the previous subsection, the following conclusions could be drawn:

- Overall, nanocomposite foams with the smallest mean cell sizes of 9 µm were achieved with PMMA/TRGO nanocomposite foams.
- Based on the *VER* values achieved, medium to low-density foams with cell densities and nucleation densities of the order 10^9 were generated.
- PS nanocomposite foams were majorly characterized by higher *VER* while PMMA nanocomposites yielded foams with smaller cell sizes (microcellular).

- TRGO filler were found to be the most effective foam-nucleating agent based on the mean cell sizes and volume expansion ratios achieved in comparison to foams prepared with talc and carbon black.
- The CO_2 retention capacity of PMMA was exploited to prepare microcellular low-density blend foams with VER of up to 16.
- The relationship established between the VER versus t_{cw} and $t_{s.eq}$ is summarized in Table 5.10.

Table 5.10: Established relationship between the VER and the respective cell wall and equivalent strut thicknesses, according to foam density.

	PS foams		**PMMA foams**		**PS/PMMA blend foams**	
Low-density	$VER \downarrow$	$t_{cw} \nearrow; t_{s.eq} \nearrow$	$VER \downarrow$	$t_{cw} \searrow; t_{s.eq} \searrow$	$VER \downarrow$	$t_{cw} \nearrow; t_{s.eq} \nearrow$
Medium-density	$VER \downarrow$	$t_{cw} \nearrow; t_{s.eq} \nearrow$	$VER \downarrow$	$t_{cw} \searrow; t_{s.eq} \searrow$	$VER \downarrow$	$t_{cw} \nearrow; t_{s.eq} \nearrow$
High-density[74]	-	-	-	-	-	-

5.6.5 Gained knowledge that can be transferred to foam extrusion studies

- From the CO_2 sorption experiments, the maximum amount of gas soluble in each polymer matrix will serve as a guide in subsequent foam extrusion expansion ratio studies.
- The batch foam-processing parameters such as foaming temperature, pressure, etc. that lead to the fabrication of micro cell-sized low-density foams will also serve as a guide to optimizing the processing conditions[75] in foam extrusion studies.

---

[74] The batch foam experiments carried out in this study did not lead to high density foams.

[75] Refers, for example, to die temperature, melt temperatures, etc.

5.7 Extruded nanocomposite foams

The preparation of extruded foams of PS (XPS) and PS/PMMA (XPS/XPMMA) is the primary focus of this chapter. To meet the objectives of this work, volume expansion ratio studies involving the individual and combination of physical blowing agents were carried out. The influence of the filler size, geometry, dispersion quality and load-rates on the cell morphologies and properties of the extruded foams was investigated. The effect of blending on the mean cell size, cell nucleation and foam densities were also investigated.

Furthermore, the influence of the following processing parameters – die temperature, melt temperature, etc. on the foam properties was also studied. Lastly, the thermal conductivities of the prepared extruded foams are investigated at different temperatures.

5.7.1 Extruded PS nanocomposite foams

5.7.1.1 Foam expansion ratio studies

This study focuses basically on achieving foams with low densities. There are basically two types of expansion that could be used to characterized polymeric foams:

- Volume expansion ratio (*VER*): this takes into account the change in volume of the entire foam with respect to the compact solid material.
- Radial expansion ratio (*RER*): this takes into consideration the foam's cross-sectional area; i.e. its values are estimated from the quotient of the cross-sectional area of the extruded foam strands to the cross-sectional area of the die shaping element.

VER is of paramount importance because it indirectly reveals the densities of the foams. On the other hand, RER shows the physical dimensions of the foams which are relevant to certain foam property measurements such as thermal conductivity.

PS was chosen specifically for expansion ratio studies using a cylindrical die and the processing conditions used are given in Table 5.11. The experimental die temperature (T_{die}) was kept the same as the inlet melt temperature (T_{im}) for the entire duration of the experiments. The foams under study were allowed to freely expand without any form of calibration, as depicted in Figure 5.43.

Table 5.11: Processing conditions and setup employed for XPS foam expansion ratio studies.

screw speed	throughput	die geometry	die gap	die land
11 rpm (1st barrel) 5 rpm (2nd barrel)	5 kg/h	cylindrical	3 mm	6 mm

Figure 5.43: Representation of the expansion ratio of XPS processed with 4 wt% of CO_2.

5.7.1.2 Foam expansion ratio studies with carbon dioxide

The carbon dioxide (CO_2) solubility limit of PS was investigated by metering variable amount (3 wt% to 9 wt%) of supercritical CO_2 into melt. Based on the results of a sorption kinetic experiment (described in section 5.5), 7 wt% of CO_2 was determined as the maximum amount that could be metered into the melt. This quantity is less than the estimated amount determined from sorption experiments carried out in solid state.

Figure 5.44 compares the VER values of the XPS foams prepared with 4 wt% and 7 wt% of CO_2. Higher VER were observed at $T_{die} = T_{im}$ < 150 °C. It is also evident that, with 7 wt% of CO_2, the VER were not better than with 4 wt%. This might be a result of the escape of CO_2 through the foam-skin during cell growth and expansion. Due to the fact that slightly higher VER were obtained with 4 wt% of CO_2, talc (benchmark nucleating agent) was used to perform subsequent expansion ratio test experiments. The results thereof (Figure 5.44) show that the expansion ratios of XPS with talc and without talc are comparable. The lowest densities (40 kg/m^3 to 50 kg/m^3) of the XPS foams with or without talc were achieved at T_{die} = 125 °C to 145 °C. An attempt to process foams at T_{die} < 125 °C so as to induce higher pressures that would in turn lead to higher pressure drop rates only led to freezing out of the die, as shown in Figure 5.45. The focus of expansion ratio studies was placed solely on XPS because PS is the main matrix of choice. Therefore, VER studies of XPMMA and XPS/XPMMA were left out.

Similar VER experiments were carried out using a slit die (gap: 0.5 mm gap, die length: 100 mm, die land: 60 mm). With 4 wt% of CO_2, the generated foams had corrugated surfaces. This poor surface feature has also been reported for XPS foams in particular [192]. It was claimed in the report that the use of a co-blowing agent led to better surface characteristics. Therefore, CO_2 in combination with ethanol was used in subsequent VER studies.

Lastly, the results show that metering a high amount of CO_2 does not necessarily translate to a linear increase of the VER or a decrease of foam densities, especially when the CO_2-solubility capacity of the PS has been exceeded.

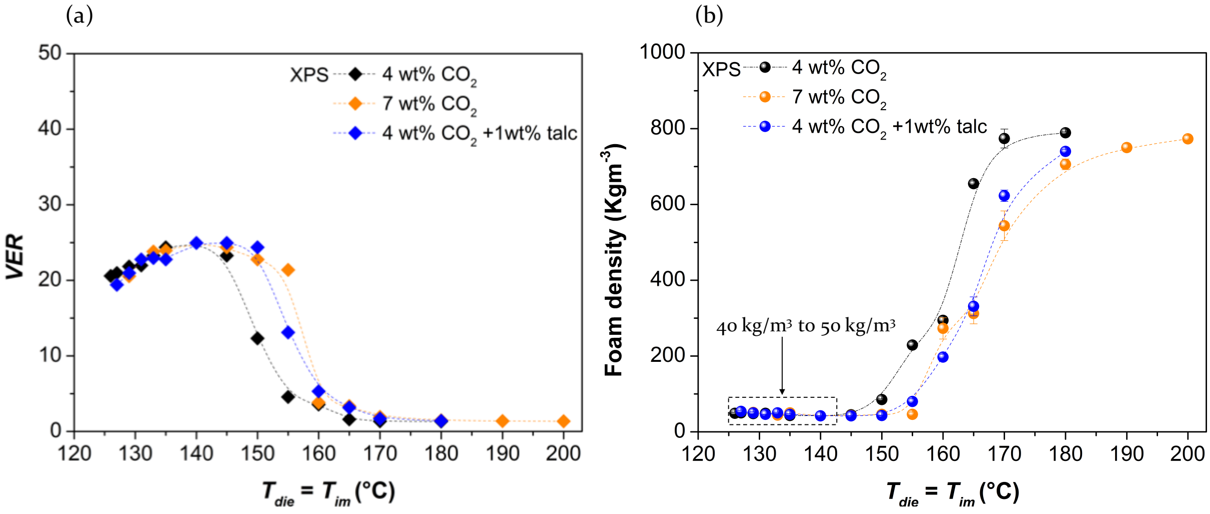

Figure 5.44: Properties of XPS foams prepared with 4 wt% and 7 wt% of CO_2 (a) *VER* and (b) foam densities.

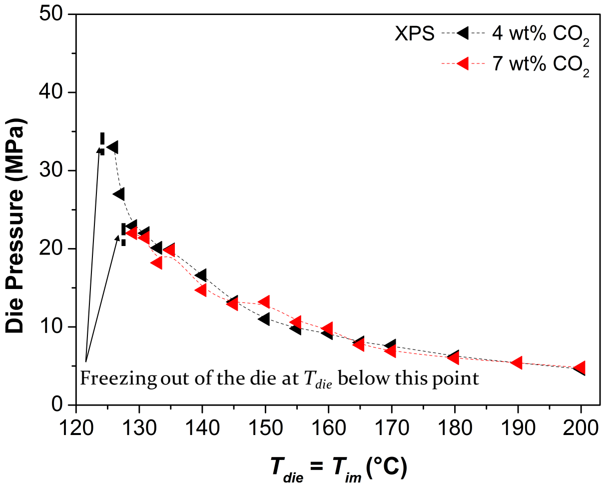

Figure 5.45: Pressure values where the extrusion die freezes out preventing foam processing at lower temperatures.

5.7.1.3 Foam expansion ratio studies with a of combination of CO_2 and ethanol

Due to the solubility limit (4 wt%) of CO_2 in PS coupled with the poor surface characteristics of the resultant XPS foams prepared using a slit die, ethanol (EtOH) was employed as a co-blowing agent with the aim of solving the corrugation problem and enhancing the plasticizing power of CO_2 [12,87,214]. The use of co-blowing agents also broadens the processing temperature window at which foams can be processed. For the purpose of this work, it means that foams could be processed at T_{die} ≤ 125 °C. Figure 5.46 shows the *VER* of the XPS foams processed with a combination of CO_2 and EtOH as a function of T_{die}. It must be mentioned here that combinations with less than 3 wt% of EtOH did not yield satisfactory results.

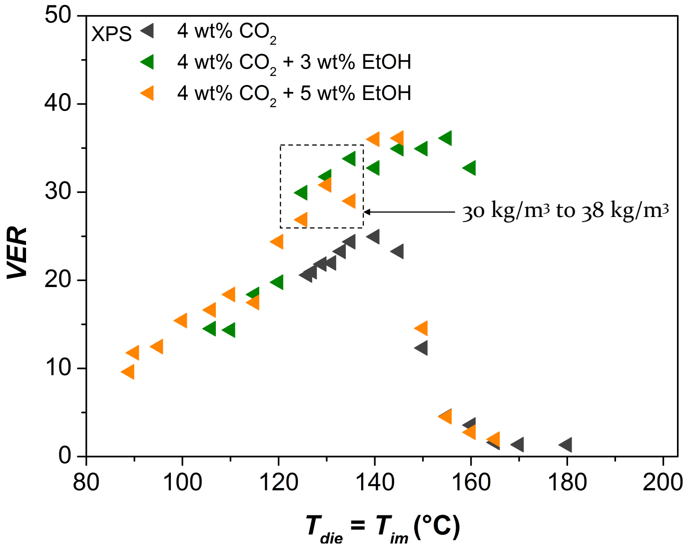

Figure 5.46: XPS processed with a combination of CO_2 and ethanol.

With the following blowing agent combinations: (i) CO_2 (4 wt%) + EtOH (3 wt%) and (ii) CO_2 (4 wt%) + EtOH (5 wt%) extruded foams with densities between 30 kg/m^3 and 38 kg/m^3 were achieved at T_{die} between 120 °C and 140 °C. These combinations enabled foams to be processed at much lower temperatures compared to when the XPS was processed with CO_2 alone. This represent about a 14 % to 30 % decrease or expansion of the foam processing window.

Furthermore, a maximum *VER* of 36 was achieved from both blowing agent combinations but at different processing temperatures. From the *VER* foam studies, the best ϕ_m of between 500 µm and 700 µm were observed at T_{die} between 120 °C to 135 °C. Ultimately, a $T_{die} = T_{me} =$ 120 °C was selected and fixed for all subsequent cell morphological studies.

5.7.2 XPS nanocomposite foams prepared with a slit die

In an attempt to fabricate foamed panels that can be used for subsequent thermal conductivity measurements, a slit-die with the following dimensions[76] was used for all foam-processing experiments on a tandem extrusion line. The predefined foam processing conditions[77] from the preceding sub-section were adopted to carry out the subsequent comparative foam extrusion studies. In addition to talc, CB and TRGO fillers, MWCNT was used to compare the geometric influence of the respective fillers on the cell morphologies of the XPS foams.

Lower filler load rates (0.025 wt%, 0.1 wt%, and 1.0 wt%) were used in order to attain optimal cellular structures and foam densities and due to the limited quantity of the laboratory synthesized TRGO fillers available for use. All the extruded foams were calibrated after die exit to obtain foam panels.

---

[76] Die gap: 0.5 mm, die length: 100 mm and die-land: 60 mm.

[77] $T_{die} = T_{im} =$ 120 °C; CO_2 (3 wt%) + EtOH (4 wt%).

Cell morphology of XPS nanocomposite foams

Figure 5.47 shows the SEM images of the microstructures of the XPS nanocomposite foams. The ρ_f as well as the ϕ_m of the respective foams are also displayed in the images. Gas pycnometer analysis showed the foams have a closed-cell content of approximately 97 % and they displayed cell size distribution that conforms to the Gaussian distribution.

Cell size evaluation revealed the ϕ_m of XPS/neat to be 400 µm. The mean size reduction by 22 %, 71 % and 84 % were respectively achieved with the inclusion of talc, MWCNT and TRGO particles at 0.025 wt%. In contrast to the others, the mean cell size was increased by 47 % with the introduction of CB nanoparticles at the same load rate. As expected, further reductions of the $\phi_m$were achieved as the filler load rates were raised to 1 wt%. Of significant importance is the tremendous cell size reduction of approximately 94 % (ϕ_m= 25 µm) by TRGO particles at a load rate of 1 wt%. This is the smallest cell size ever reported in the literature for XPS nanocomposite low-density foams. That the smallest cell sizes were achieved with TRGO fillers confirms what was predicted from the dynamic shear rheological experiments: that the higher elastic melt property of PS/TRGO nanocomposites in comparison to PS/talc and PS/CB nanocomposites would lead to the generation of foams with smaller cells due to cell growth suppression by the foam cell elastic walls. The additional effect of calibration is assumed to play a role in stabilizing the already formed cells. Still at 1 wt% filler load rate, the following mean cell sizes were achieved with talc (ϕ_m= 48 µm), CB (ϕ_m= 40 µm) and MWCNT (ϕ_m= 52 µm).

It is interesting to see that the mean cell sizes achieved with extruded nanocomposite foams are larger than that processed with batch foam process but the densities realized with extruded foams are much lower than with batch foams. For example, PS nanocomposite foams nucleated with 1 wt% TRGO showed the following foam characteristics:

extruded foam (XPS): ϕ_m = 25 µm, ρ_{foam} = 60 kg/m^3 and VER = 17.5
batch foam (PS): ϕ_m = 13 µm, ρ_{foam} = 153 kg/m^3 and VER = 6.9

The reason for this significant difference in the foam properties lies in the viscoelastic melt properties of the nanocomposites during the foaming process. In a batch foam process, the nanocomposite samples are saturated with a blowing agent in the solid state or semi-solid state. Therefore, the sample has higher melt viscosity that help to suppress cell growth thus, leading to smaller cell sizes and of course higher foam densities. On the other hand, foams processed via foam extrusion are saturated in the melt state which means a lower melt viscosity[78] that allows more room for the cells to grow and expand. This results to foams with relatively larger mean cell size and higher volume expansion ratios (i.e. low-density foams).

---

[78] The melt viscosity can be adjusted as needed by changing the processing temperatures and amount of blowing agent fed into the melt.

The ρ_{cell} and ρ_{nucl} of the XPS foams are presented in Figure 5.48. High ρ_{cell} of up to 10^8 was achieved with TRGO at the highest foam concentration prepared. A progressive increase of the ρ_{cell} was observed as the filler content were increased accordingly. Good filler dispersion and higher surface areas are among the reasons for the high ρ_{cell} experienced with TRGO particles in comparison to talc, CB and MWCNT. The relationship between the surface area and the Gibb's free energy of nucleation is expressed in equation 5.3, where f is the energy nucleation factor, m surface curvature and θ_c contact angle. This expression in the aforementioned equation implies that particles with larger surface areas will result in higher contact angles, thus reducing the heterogeneous Gibbs free energy of nucleation. A consequence of this is the nucleation of more cells.

$$\Delta G^*{}_{het} = \Delta G^*{}_{hom} \frac{f(m, \theta_c)}{2} \tag{5.3}$$

The result of ρ_{nucl} at all filler load rates showed similar trend to that of the ρ_{cell}. The maximum ρ_{nucl} achieved at 1 wt% for the respective XPS foams in descending order are: 1.40 x 10^{10} (TRGO), 9.30 x 10^9 (MWCNT), 4.1 x 10^8 (talc), 3.1 x 10^7 (TRGO). The ρ_{nucl} results appear to differ from one another by one order of magnitude.

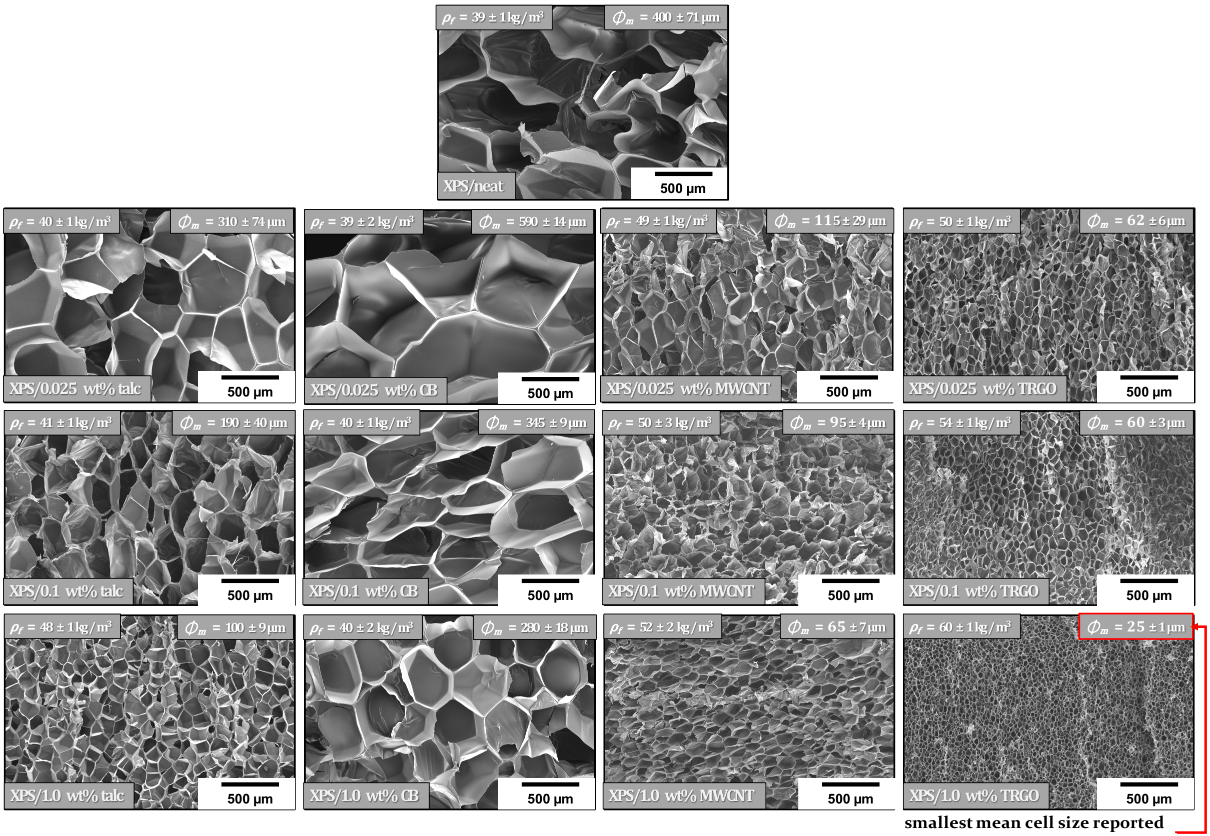

smallest mean cell size reported for any XPS low-density foam

Figure 5.47: Cell morphologies of XPS nanocomposite foams showing their respective mean cell sizes and densities at different filler concentrations.

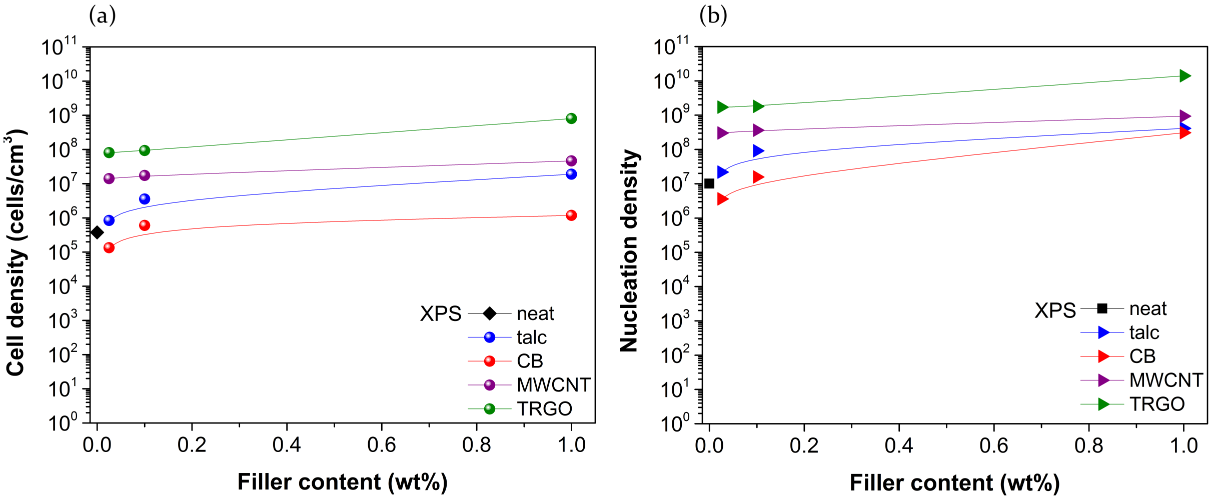

Figure 5.48: Plot showing (a) Cell densities (b) nucleation densities of XPS nanocomposite foams prepared with different filler concentrations.

Plots of the volume expansion ratios and thickness of the cell walls and cell struts as a function of filler load rates are presented in Figure 5.49 and Figure 5.50, respectively. Overall, the foams generated are low-density foams based on the values of the volume expansion ratios ($VER > 10$). Further analysis of the results revealed that when the difference in mean cell sizes between the same low-density nanocomposite foams is larger than 59 µm (i.e. $\phi_{m1} - \phi_{m2} > 59$ µm), the t_{cw} and $t_{s.eq}$ will start to differ considerably as exemplified in Table 5.12.

Table 5.12: Cell wall and cell struct thicknesses as a function of mean cell size.

Sample	**Density (kg/m^3)**	**Mean cell size (µm)**	**t_{cw} (µm)**	**$t_{s.eq}$ (µm)**
XPS/0.025 wt% talc	40 ± 1	310 ± 74	8.3 ± 4	12.7 ± 5
XPS/0.1 wt% talc	41 ± 1	190 ± 40	4.6 ± 3	7.3 ± 4
XPS/0.025 wt% CB	39 ± 2	590 ± 14	11.3 ± 5	16.3 ± 6
XPS/0.1 wt% CB	40 ± 1	345 ± 9	7.1 ± 3	9.3 ± 4
XPS/0.025 wt% MWCNT	49 ± 1	115 ± 29	3.0 ± 2	4.4 ± 2
XPS/0.1 wt% MWCNT	50 ± 3	95 ± 4	4.2 ± 2	7.7 ± 4
XPS/0.025 wt% TRGO	50 ± 1	62 ± 6	1.8 ± 1	2.0 ± 0.9
XPS/0.1 wt% TRGO	54 ± 1	60 ± 3	1.4 ± 0.6	2.1 ± 0.8

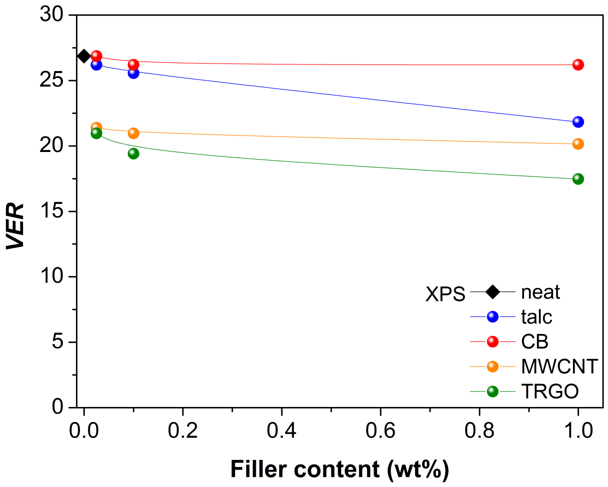

Figure 5.49: Volume expansion ratios of XPS nanocomposite as a function of filler load rates.

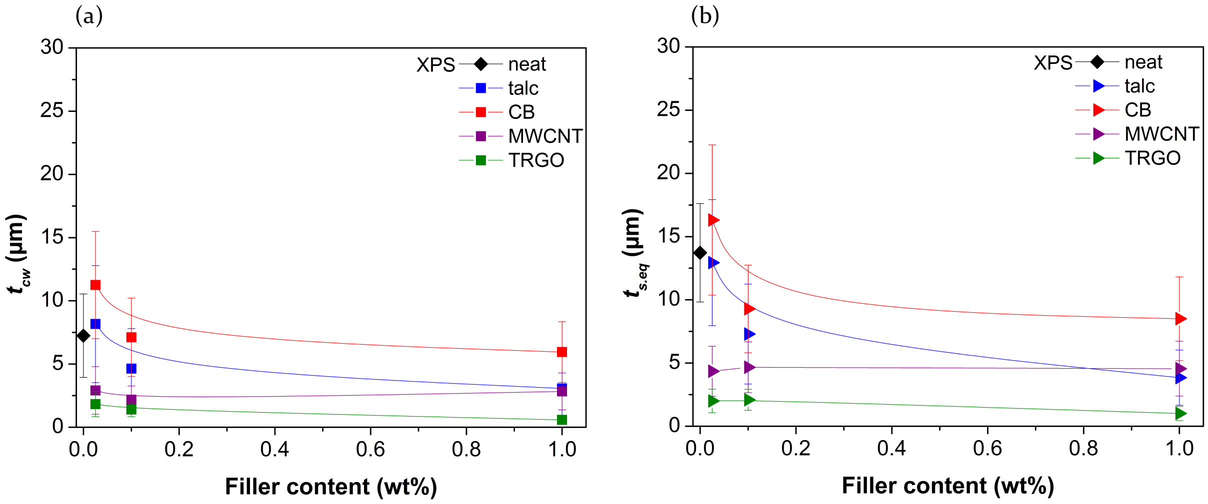

Figure 5.50: Cell wall and equivalent strut thicknesses as a function of filler concentrations.

The cell wall and strut thickness of the extruded foams when arranged in descending order were found to be: XPS/CB > XPS/talc > XPS/MWCNT > XPS/TRGO.

The findings of these studies suggest that the t_{cw} and $t_{s.eq}$ of low-density XPS foams with very similar densities can be affected in the following ways:

- When $\phi_{m1} - \phi_{m2} \geq 60$ µm, then $t_{cw1} > t_{cw2}$ and $t_{s.eq1} > t_{s.eq2}$.
- When $\phi_{m1} - \phi_{m2} < 60$ µm, then $t_{cw1} \equiv t_{cw2}$ and $t_{s.eq1} \equiv t_{s.eq2}$.
- As $VER \downarrow = t_{cw} \rightarrow$; $VER \downarrow = t_{s.eq} \rightarrow$

5.7.3 Thermal conductivity of XPS nanocomposite foams

As earlier explained, CB and TRGO have infrared absorbing and reflective capabilities that contribute to the decrease in the thermal gas component (λ_{gas}), which is one of the components of the overall foam thermal conductivity (λ_{foam}). As explained in section 2.1, at temperatures above 50 °C, the influence of ($\lambda_{radiation}$) will increase relative to (λ_{solid}) and (λ_{gas}). Therefore, the thermal conductivity measurements of the XPS foams were conducted at temperatures ranging between 23 °C to 90 °C as shown in Figure 5.51, in order reveal the potentials of infrared absorbing carbon-based fillers (CB and TRGO) in particular.

The lowest λ_{foam} = 31 mW/mK at 23 °C was achieved with XPS/1 wt% TRGO foams. This translates to approximately an 8 % reduction of λ_{foam} in comparison to XPS/neat (reference material) and a 3 % reduction in comparison to Styrodur® C (a commercially available XPS from BASF). Even at higher temperatures, i.e. 35 °C, 50 °C, 70 °C and 90 °C, the XPS/TRGO outperforms the others.

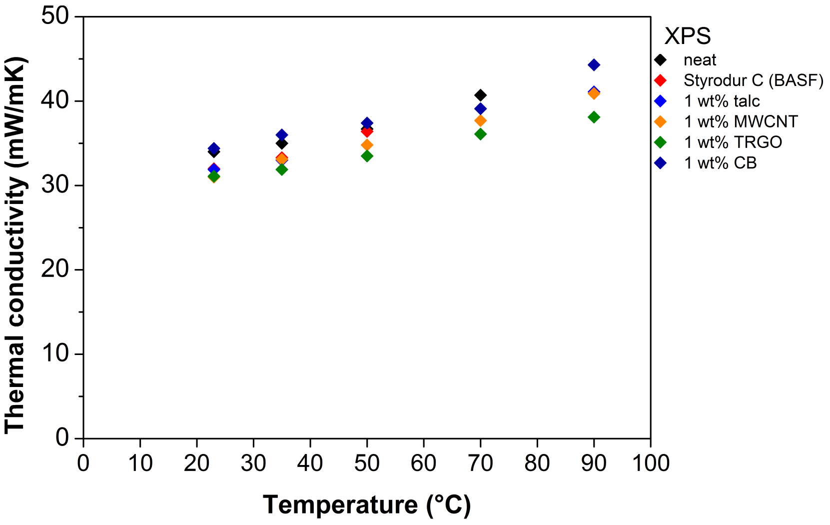

Figure 5.51: Thermal conductivity values of the XPS foams measured at temperatures: 23 °C, 35 °C, 70 °C and 90 °C.

The observed lower thermal conductivity values of XPS/TRGO foams in comparison to other nanocomposite foams is attributed to (i) the absorption of infrared radiation by TRGO fillers and (ii) the smaller mean cell size (Figure 5.47). Lee L. J. et al. [82] prepared XPS foams with wood-based activated carbon (AC), carbon nanofiber (CNF) and graphite (GR) particles. The results of their work are presented in Figure 5.52. With 2 wt% of GR, a thermal conductivity of approximately 31 mW/mK was achieved. It must be stated here that the same feat was achieved in this study but with a lower amount of filler (1 wt% TRGO). Furthermore, the XPS/neat foam displayed, in comparison to all other nanocomposite foams, the highest thermal conductivities at all temperatures measured.

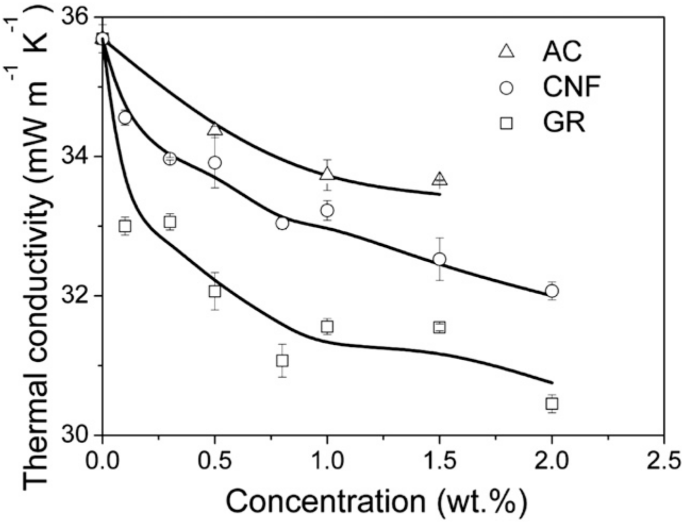

Figure 5.52: Thermal conductivity of XPS foams with different fillers [82].

5.7.4 Conclusion on XPS nanocomposite foams

The foam extrusion of PS using the defined foaming conditions from the preceding chapter led to the fabrication of low-density foams with all displaying homogenous cell microstructures. TRGO fillers, in comparison to talc, CB and MWCNT, has proven to be the most effective nucleating agent owing to:

- The generation of XPS foams with the smallest mean cell size of 25 ± 1 µm. This feat to the best of our knowledge is the smallest mean cell for any low-density (60 kg/m^3; *VER* = 17.5) XPS foam that has been reported in the literature.
- The higher cell densities and nucleation densities (10^9 cells/cm^3) achieved.
- The low thermal conductivity (31 mW/mK) that was achieved, which is 8 % and 3 % better than XPS/neat foam and Styrodur ® C.

5.8 Extruded PS/PMMA blend nanocomposite foams

The results obtained from solid-state batch foaming of PS, PMMA and PS/PMMA blends showed that when PS is blended with PMMA, the resultant foams exhibit increased volume expansion ratios, cell densities and foam nucleation densities. In addition, the use of TRGO fillers led to the realisation of PMMA nanocomposite foams with a mean cell size of 9 µm. To recap, the aims of this section were to:

- Process foams with the maximum amount (up to 15 %) of CO_2 in which the melt can dissolve.
- Extrude foams at low temperatures (90 °C to 110 °C) in order to maximise the dissolved blowing agent (CO_2) in order to increase the cell densities and nucleation densities, thereby decreasing the mean cell size.

In light of this, a one-to-one comparison between the extruded foams will not be made but, rather, the results will be discussed and comparisons made between individual systems (filled and unfilled). Just like in batch-foamed PS/PMMA blend, TRGO fillers will be employed as the sole nucleating agent. The nanocomposite foam concentrations will be prepared at very low filler load rates due to the limited amount of TRGO available at the time the experiments are to be conducted. Talc and CB fillers were excluded as TRGO outperformed them according to the XPS foam extrusion study results.

5.8.1 Cell morphology of XPS/XPMMA blend nanocomposite foams

The SEM micrographs in Figure 5.53 show the cell morphological structures of the unfilled extruded blend foams. The amount of CO_2 used to process the respective foams is also shown in the figure. By blending PS with 10 wt% of PMMA (XPS/XPMMA, 90/10), the mean cell size of XPS (175 µm) was decreased by approximately 44% while the foam density remained more or less unchanged. As the PMMA component of the blend was increased to 20 wt% (80/20), the ϕ_m decreased further to 59 µm. The corresponding foam density of the 80/20 blend decreased by 20 % as well. This result confirms that the high CO_2 retention capacity of PMMA was successfully exploited to decrease the densities of the foams. It was also observed that, as the PMMA component of the XPS/XPMMA blend was increased from 10 wt% to 20 wt%, the open-cell content of the foams was raised from 8 % to 19 % due to the dissolution of more CO_2 in the melt.

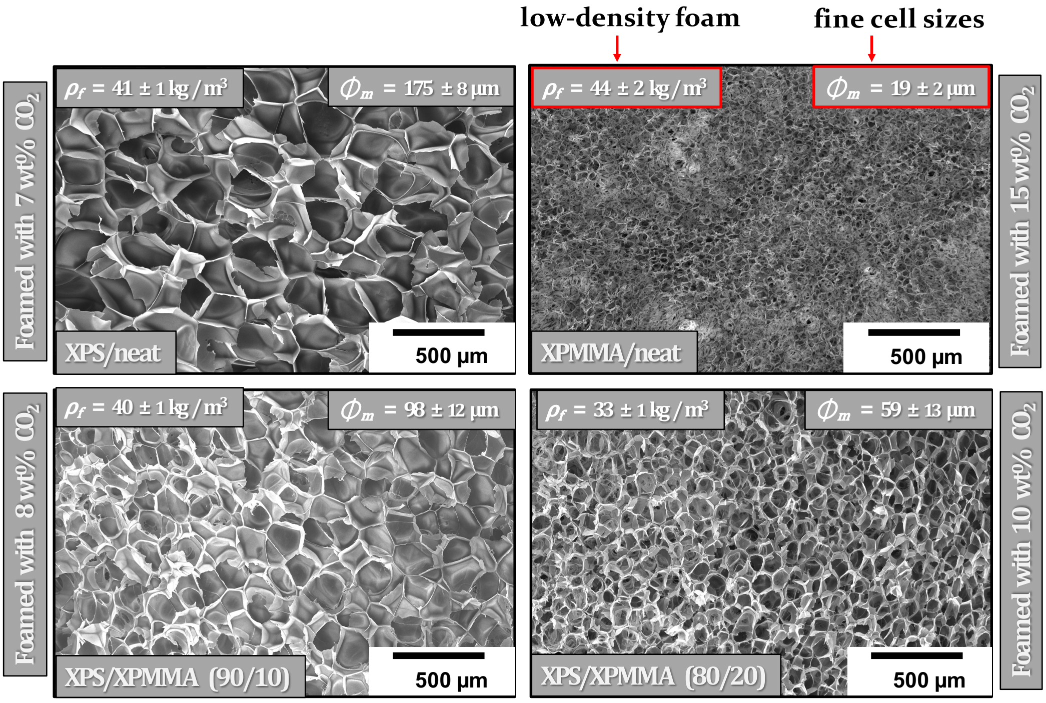

Figure 5.53: Cell morphologies of unfilled homo and blended nanocomposite foams prepared using the maximum dissolvable CO_2 possible (7 wt% to 15 wt%).

Furthermore, a ϕ_m of 19 µm was achieved for XPMMA/neat foam processed with 15 wt% of CO_2. The high amount of CO_2 metered gave a XPMMA/neat foam with a *VER* of 27.1 (ρ_f = 44 kg/m^3) and the cell microstructure was characterised by a mixture of open and closed-cells. A summary of the ρ_{cell} and ρ_{nucl} of the respective foams is given in Table 5.11. Ruckdäschel H. et al. [215] also demonstrated that an increase in the size of the dispersed droplets (PMMA in this case) enhances nucleation efficiency. Therefore, it is not surprising to see in the 80/20 blend foam an increase of the ρ_{cell} and ρ_{nucl} by one order of magnitude in comparison to the 90/10 foams. Conversely, contrasting observations were made with the introduction of 0.5 wt% of TRGO. The 90/10 + 0.5 wt% (XPS/XPMMA/TRGO) foams exhibited higher ρ_{cell} and ρ_{nucl} than the 80/20/0.5 extruded foams. This particular result is analogous to what was observed in PS/PMMA/TRGO nanocomposites batch foams.

Figure 5.54 shows the cell morphologies of the filled blend nanocomposite foams. The mean cell size (98 µm) of 90/10 was reduced to 30 µm (a 69 % cell size reduction) as 0.5 wt% of TRGO was added. Likewise, but not in equal measure, the ϕ_m of 80/20 + 0.5 wt% blend foam was decreased by about 19 %. While the ρ_f of 90/10 + 0.5 wt% decreased with the introduction of TRGO, that of 80/20 + 0.5 wt% slightly increased.

Table 5.11: Properties of homo and blended nanocomposite extruded foams.

Sample	**CO_2 content**[79]	***VER***	**Density (kg/m^3)**	**ρ_{cell} ($cells/cm^3$)**	**ρ_{nucl}**
XPS/neat	7 wt%	25.6	175 ± 8	4.0×10^6	1.0×10^8
XPMMA/neat	15 wt%	27.1	44 ± 2	2.4×10^9	6.4×10^{10}
XPS/XPMMA/neat (90/10)	8 wt%	26.6	40 ± 1	2.1×10^7	5.6×10^8
XPS/XPMMA/neat (80/20)	10 wt%	32.7	33 ± 1	1.7×10^8	5.4×10^9
XPS/XPMMA					
100/0 + 0.5 wt% TRGO	7 wt%	26.3	41 ± 1	7.0×10^7	1.9×10^9
0/100 + 0.5 wt% TRGO	10 wt%	6.3	190 ± 14	7.0×10^9	4.4×10^{10}
90/10 + 0.5 wt% TRGO	8 wt%	28.8	37 ± 1	6.3×10^8	1.8×10^{10}
80/20 + 0.5 wt% TRGO	10 wt%	25.1	43 ± 2	1.8×10^8	4.4×10^9

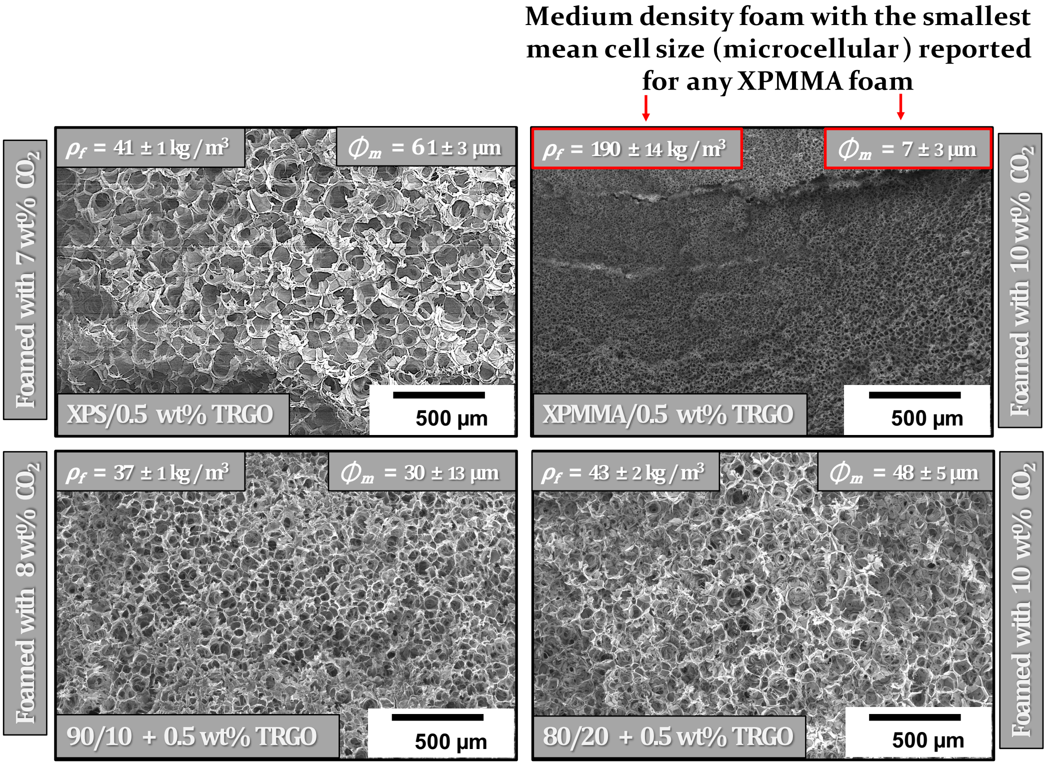
Medium density foam with the smallest mean cell size (microcellular) reported for any XPMMA foam

Figure 5.54: Cell morphology of filled XPS/XPMMA nanocomposite foams prepared using the maximum dissolvable CO_2 possible and at a filler load rate of 0.5 wt%, respectively.

Furthermore, at a TRGO filler concentration of 0.5 wt%, the ϕ_m of XPMMA/neat foam was decreased remarkably by 63 % from 19 µm to 7 µm. The *VER* also decreased by approximately 76 % from 27.1 to 6.3 and that, by definition, categorises the XPMMA/0.5 wt% TRGO nanocomposite foams as

---

[79] Maxim dissolvable amount of CO_2 in the respective polymer matrix.

microcellular medium-density foams. There are unfortunately no data in the literature to compare these results with.

5.8.2 Conclusion on XPS nanocomposite foams

- XPS/XPMMA nanocomposite foams have been successfully prepared using TRGO as a cell-nucleating agent. By definition, medium-density microcellular foams (7 µm) were generated.
- Nucleation densities of up to 10^{10} cells/cm^3 were achieved with 90/10 + 0.5 wt% TRGO nanocomposite foam.
- An attempt to dissolve the maximum quantity of CO_2 into the melt led to an increase of the open-cell content of the foams.

6 Summary and outlook

6.1 Summary

This aim of this comparative study is to prepare microcellular low-density nanocomposite foams. In order to realise the set goal, nanocomposite foams of PS, PMMA and PS/PMMA blends were nucleated with the following nucleating agents: thermally-reduced graphite oxide (TRGO), carbon black (CB) and talc (benchmark nucleating agent) at filler concentration of 0.025 wt% to 1 wt%. These foams were processed with batch-foaming (pressure induced method) and foam extrusion technologies.

At first, BET surface area experiments were used to characterise the fillers and the results showed TRGO to have the highest specific surface area of 600 m^2/g, followed by CB (122 m^2/g) and then talc (17 m^2/g). The fillers were dispersed with an optimum screw configuration designated as *MS-C* in a melt-blending process. The morphology of the nanocomposites examined under a transmission electron microscope indicated that the fillers were well distributed and adequately dispersed in the respective matrices. Tiny agglomerates of CB nanoparticles, which were observed in PMMA owing to hydrophobic interaction between the CB and PMMA, were dispersed in a second melt-blending process. A sea-island morphology was observed for the blend ratios (PS/PMMA (90/10 and 80/20) prepared in this study. An increase of the PMMA content from 10 wt% to 20 wt% led to an increase of the droplet number density by a factor of two. Based on the number of particles per μm^2 estimated for TRGO fillers in the respective nanocomposites, it can be said that TRGO particles exhibited more pronounced affinity with PS than with PMMA.
Analysis of the dynamic shear viscoelastic properties of the nanocomposites specifically by means of a van-Gurp-Palmen-plot revealed that nanocomposites filled with TRGO particles behaved more like elastic solids, while nanocomposites embedded with CB and talc particles displayed a more viscous character, similar to the unfilled systems (neat matrices). These characteristics were observed even at a filler concentration of 1 wt%. It was also observed that particle number densities contributed more to changes in the viscoelastic properties of PS than the droplet number of the dispersed phase (PMMA) in the blends.

Analysis of the tensile test results of the rigid nanocomposites suggested that the fillers used in this study were non-reinforcing. Additional examination of the microstructures of the nanocomposites disclosed the weak interfacial interaction between the fillers and the matrices. A “pull out” effect, which was particularly observed for CB particles, further confirmed this.

CO_2 sorption and desorption studies disclosed that PMMA absorbed twice (19 wt%) as much gas as PS (9 wt%) owing to the bonding of its carbonyl oxygen to CO_2. Higher diffusion coefficients (D_d) were observed for PMMA nanocomposites in comparison to PS nanocomposites. The amount of CO_2 absorbed by PS increased as a result of blending with PMMA from 9 wt% to 12 wt%.

The foams processed via pressure-induced batch foaming all exhibited homogenous closed cell (95 %) structures with cell size distributions that could be described as Gaussian. PS batch foams, which were seen to have volume expansion ratios of 7 to 13 (low-density), had at best a mean cell size of 20 µm, while PS batch foams displaying a VER of 4 to 10 (medium-density) produced mean cell sizes of 13 µm. The maximum cell densities observed for PS batch foams were approximately 10^9 cells/cm^3. Based on the analysis of the PS batch foam study results, relationships between the VER and the cell wall (t_{cw}) and equivalent strut ($t_{s.eq}$) thickness were established and they are given below:

$VER \downarrow = \ t_{cw} \nearrow$; a decrease of VER led to a slight decrease of the cell wall thickness.

$VER \downarrow = \ t_{s.eq} \nearrow$; a decrease of VER caused the equivalent strut thickness to decrease slightly as well.

In PMMA nanocomposite batch foams, VER between 7 and 10 were realised and cell densities of up to 10^{10} cells/cm^3 were achieved as well. At a filler load rate of 1 wt%, a medium-density PMMA foam with a mean cell size of 9 µm was accomplished with TRGO as nucleating agent. With respect to the relationship between VER, t_{cw} and $t_{s.eq}$, a contrasting scenario to PS foams was observed as follows: $VER \downarrow = \ t_{cw} \searrow$); $VER \downarrow = \ t_{s.eq} \searrow$.

Higher VER (10 -16) were achieved with PS/PMMA blend nanocomposites batch foams (90/10 and 80/20) in comparison to PS and PMMA batch foams. By nucleating the 90/10 blend with 1 wt% of TRGO particles, microcellular (10 µm) low-density foams (110 kg/m^3) were achieved. Cell densities and nucleation densities of the order 10^9 cells/cm^3 were accomplished.

The relationships established between the VER, t_{cw} and $t_{s.eq}$, for the medium and low-density foams generated in this thesis are summarized in Table 6.1.

Table 6.1: Influence of volume expansion ratio on cell wall and equivalent strut thickness for batch foams.

	PS foams		**PMMA foams**		**PS/PMMA blend foams**	
Low-density	$VER \downarrow$	$t_{cw} \nearrow; t_{s.eq} \nearrow$	$VER \downarrow$	$t_{cw} \searrow; t_{s.eq} \searrow$	$VER \downarrow$	$t_{cw} \nearrow; t_{s.eq} \nearrow$
Medium-density	$VER \downarrow$	$t_{cw} \nearrow; t_{s.eq} \nearrow$	$VER \downarrow$	$t_{cw} \searrow; t_{s.eq} \searrow$	$VER \downarrow$	$t_{cw} \nearrow; t_{s.eq} \nearrow$

The results from the expansion ratio studies of XPS foam with variable amount of CO_2 indicated that metering CO_2 in high amount (e.g. 7 wt%) does not translate to higher VER. A CO_2 content of 4 wt% was found to be the optimum amount for PS. Addition of ethanol as a co-blowing agent further increased the VER of the XPS foams by exerting supplementary plasticising power. This combination of physical blowing agent enabled the processing of the foams at relatively low temperatures.

The XPS foams prepared with talc, CB and TRGO displayed uniform cell homogeneities throughout. An average cell size of 25 µm and density of 60 kg/m^3 (VER = 18) were achieved for XPS nucleated with 1 wt% TRGO. This constitutes, to date, the smallest cell size ever reported in the literature for any low-density XPS nanocomposite foam. In addition, cell densities of 10^9 cells/cm^3 were accomplished with the aforementioned XPS/TRGO foams. Based on the analysis of the XPS foam properties, an interesting relationship between the cell size, cell wall and equivalent strut thickness for low-density XPS foams having similar densities was established (i.e. comparing two different XPS foams with similar densities but different mean cell sizes):

- When $\phi_{m1} - \phi_{m2} \geq 60$ µm, then $t_{cw1} > t_{cw2}$ and $t_{s.eqv\,1} > t_{s.eqv\,2}$
- When $\phi_{m1} - \phi_{m2} < 60$ µm, then $t_{cw1} \equiv t_{cw2}$ and $t_{s.eqv\,1} \equiv t_{s.eqv\,2}$

The relationship between the *VER*, t_{cw} and $t_{s.eqv}$ defined for PS low-density batch foams was also found to be valid for low-density XPS foams.

At a filler load rate of 1 wt%, a thermal conductivity (λ_{foam}) of 31 mW/mK was achieved with XPS/TRGO foams. This result is 8 % and 3 % better (i.e. lower) than XPS/neat and Styrodur® C, respectively.

Medium density XPMMA foams (*VER* = 6.2) characterised by a mean cell size of 7 µm were produced with as little as 0.5 wt% of TRGO fillers.
Extruded XPS/XPMMA foams prepared from blends (90/10 and 80/20) were characterised by very high *VER* of between 27 and 36 and cell densities of 10^9 cells/cm^3.

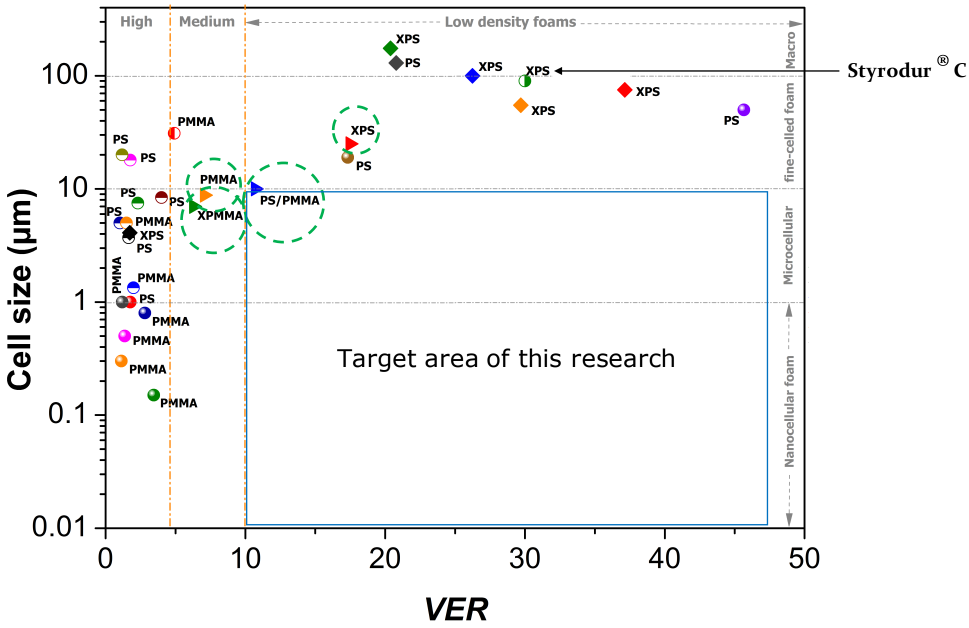

Figure 6.1: Comparing the results of the nanocomposite foams produced in this thesis work with the results of batch and extruded PS, PMMA and PS/PMMA blend nanocomposite foams found[80] in the literature [13,14,202–205,45,46,50,54,71,87,110,127].

Finally, the significance of the results obtained in all comparative foam studies is again shown in Figure 6.1. The foams generated in this work are highlighted with wedged circles. It can be seen that the target set for this thesis was met. Considering the cell sizes and foam densities that were achieved in this comparative study, TRGO was the most effective cell nucleating agent in comparison to talc and carbon black.

---

[80] The survey only considered articles where the densities and corresponding cell sizes were stated. No published articles were found in the literature on extruded PMMA (XPMMA) foams that fulfilled such criteria.

6.2 Outlook

Due to the benefits and multi-functionalities of polymeric foams in many facets of life, a shift in the use of microcellular to nanocellular foams is being witnessed, especially in the building and construction industry. The foam studies undertaken in this thesis were based on homopolymers of PS and PMMA as well as PS/PMMA blends, and commendable foam results were achieved, especially where thermally-reduced graphite oxide (TRGO) acted as the cell-nucleating agent. In light of this, the following is recommended for future works:

- Blend ratios other than 90/10 and 80/20, which may result in other interesting morphologies, should be explored to investigate their influence on foam cell size and density.
- Apart from using polymer blends, co-polymers containing acyl methacrylate block should also be investigated due to their high CO_2 retention capacity that might translate to the realisation of nanocellular low-density foams.
- One of the limitations of this study was the availability of TRGO which served as the most effective nucleating agent in all foam investigations conducted within the scope of this work. Therefore, new or advanced synthetic routes to making these fillers in sufficient quantities should be studied.
- A combination of ethanol with CO_2 was shown to be very effective in delivering foams with high volume expansion ratios. Therefore, it is recommended that new or different combination of blowing agents be explored.
- The majority of studies on polymeric foams have conducted thermal conductivity measurements at ambient temperatures. It will be more meaningful to conduct such measurements at low temperatures (e.g. less than 5 °C), similar to what is experienced in the winter period.

7 References

[1] Lee S. T. Foam Extrusion: Principles and Practice. Florida: CRC Press LLC; 2000.

[2] Sorrentino L, Aurilia M, Iannace S. Polymeric Foams from High Performance Thermoplastics. Adv Polym Technol 2011;30:234–43.

[3] Martini JE, Waldman FA, Suh NP. “The Production and Analysis of Microcellular Thermoplastic Foams”. SPE ANTEC Tech. Pap., vol. 43, 1982, p. 674–6.

[4] Yeh SK, Huang CH, Su CC, Cheng KC, Chuang TH, Guo WJ, et al. Effect of dispersion method and process variables on the properties of supercritical CO_2 foamed polystyrene/graphite nanocomposite foam. Polym Eng Sci 2013;53:2061–72.

[5] Lee Y, Wang K. Effects of clay dispersion on the foam morphology of LDPE/clay nanocomposites. J Appl Polym Sci 2007;103:2129–34.

[6] Zeng C, Hossieny N, Zhang C, Wang B. Synthesis and processing of PMMA carbon nanotube nanocomposite foams. Polymer 2010;51:655–64.

[7] Antunes M, Gedler G, Velasco JI. Multifunctional nanocomposite foams based on polypropylene with carbon nanofillers. J Cell Plast 2013.

[8] Costeux S. CO_2-blown Nanocellular foams. J Appl Polym Sci 2014;131:41293.

[9] Ji G, Wang J, Zhai W, Lin D, Zheng W. Tensile properties of microcellular poly(lactic acid) foams blown by compressed CO_2. J Cell Plast 2013;49:101–17.

[10] Chen L, Goren BK, Ozisik R, Schadler LS. Controlling bubble density in MWNT/polymer nanocomposite foams by MWNT surface modification. Compos Sci Technol 2012;72:190–6.

[11] Urbanczyk L, Calberg C, Detrembleur C, Jérôme C, Alexandre M. Batch foaming of SAN/clay nanocomposites with $scCO_2$: A very tunable way of controlling the cellular morphology. Polymer 2010;51:3520–31.

[12] Daigneault LE, Gendron R. Blends of CO_2 and 2-Ethyl Hexanol as Replacement Foaming Agents for Extruded Polystyrene. J Cell Plast 2001;37:262–72.

[13] Gendron R. Foaming Polystyrene with a Mixture of CO_2 and Ethanol. J Cell Plast 2006;42:127–38.

[14] Zhang C, Zhu B, Lee LJ. Extrusion foaming of polystyrene/carbon particles using carbon dioxide and water as co-blowing agents. Polymer 2011;2:1847–55.

[15] Han X, Koelling KW, Tomasko DL, Lee LJ. Effect of die temperature on the morphology of microcellular foams. Polym Eng Sci 2003;43:1206–20.

[16] Lee PC, Kaewmesri W, Wang J, Park CB, Pumchusak J, Folland R, et al. Effect of die geometry on foaming behaviors of high-melt-strength polypropylene with CO_2. J Appl Polym Sci 2008;109:3122–32.

[17] Consultants I. THE EUROPEAN MARKET FOR THERMAL INSULATION PRODUCTS. 2017.

[18] Strong AB. Plastics: Materials and Processing. New Jersey: Pearson Prentice Hall; 2005.

[19] Wang G, Zhao J, Wang G, Mark LH, Park CB, Zhao G. Low-density and structure-tunable microcellular PMMA foams with improved thermal-insulation and compressive mechanical properties. Eur Polym J 2017;95:382–93.

[20] Nelson M, Borkman R. Ab initio calculations on CO_2 binding to carbonyl groups. J Phys Chem A 1998;102:7860–3.

[21] Chen L, Rende D, Schadler LS, Ozisik R. Polymer nanocomposite foams. J Mater Chem A 2013;1:3837–50.

[22] Glicksman LR, Torpey M, Marge A. Means to improve the Thermal Conductivity of Foam Insulation. J Cell Plast 1992;28:571–83.

[23] Vo C V., Paquet AN. An Evaluation of the Thermal Conductivity of Extruded Polystyrene Foam Blown with HFC-134a or HCFC-142b. J Cell Plast 2004;40:205–28.

[24] Gong P, Buahom P, Tran M-P, Saniei M, Park CB, Pötschke P. Heat transfer in microcellular Polystyrene/Multi-Walled carbon nanotube nanocomposite foams. Carbon 2015;93:819–29.

[25] Modesti M, Lorenzetti A, Besco S. Influence of nanofillers on thermal insulating properties of polyurethane nanocomposites foams. Polym Eng Sci 2007;47:1351–8.

[26] Jarfelt U, Ramnäs O. Thermal conductivity of polyurethane foam - best performance. 10th Int Symp Dist Heat Cool 2006;Sektion 6a:1–11.

[27] Tran M-P, Gong P, Detrembleur C, Thomassin J-M, Buahom P, Saniei M, et al. Reducing Thermal Conductivity of Polymeric Foams with High Volume Expansion Made From Polystyrene/Expanded Graphite. SPE ANTEC Indianapolis 2016:1870–81.

[28] Forest C, Chaumont P, Cassagnau P, Swoboda B, Sonntag P. Generation of nanocellular foams from ABS terpolymers. Eur Polym J 2015;65:209–20.

[29] Sundarram SS, Li W. On Thermal Conductivity of Micro- and Nanocellular Polymer Foams. Polym Eng Sci 2013;53:1901–9.

[30] Costeux S, Zhu L. Low density thermoplastic nanofoams nucleated by nanoparticles. Polymer 2013;54:2785–95.

[31] Notario B, Pinto J, Solorzano E, de Saja JA, Dumon M, Rodríguez-Pérez MA. Experimental validation of the Knudsen effect in nanocellular polymeric foams. Polymer 2014;56:57–67.

[32] Liu S, Duvigneau J, Vancso GJ. Nanocellular polymer foams as promising high performance thermal insulation materials. Eur Polym J 2015;65:33–45.

[33] Greenspec. Insulation materials and their thermal properties n.d. http://www.greenspec.co.uk.

[34] Baetens R, Jelle BP, Gustavsen A. Aerogel insulation for building applications : A state-of-the-art review. Energy Build 2011;43:761–9.

[35] Trade of Industrial Insulation: Polystyrene, Phenolic Foam & Polyisocyanurate Foam. 2014.

[36] Kingspan. OPTIM-R Next generation insulation solution product information. n.d.

[37] Evonik. CALOSTAT Technical information 1404 ®.

[38] BASF. SLENTITE - The high performace insulation material from customized climate management.

[39] Aspen-aerogels. Ultra-thin-Spaceloft Datasheet.

[40] Kingspan. Xratherm-SR/CW High performance PF Wall Insulation Board product information.

[41] Kingspan. Xtratherm Thin-R-XT/CW High Performance PIR Wall Insulation Board product information.

[42] BASF. Styrodur Technical Data - Application Recommendations Dimensioning Aids.

[43] BASF. “Styropor Technical information”.

[44] Kaewmesri W, Lee PC, Park CB, Pumchusak J. Effects of CO_2 and Talc Contents on Foaming Behavior of Recyclable High-melt-strength PP. J Cell Plast 2006;42:405–28.

[45] Janani H, Famili MHN. Investigation of a strategy for well controlled inducement of microcellular and nanocellular morphologies in polymers. Polym Eng Sci 2010;50:1558–70.

[46] Li C, Yang G, Deng H, Wang K, Zhang Q, Chen F, Fu Q. The preparation and properties of polystyrene/functionalized graphene nanocomposite foams using supercritical carbon dioxide. Polym Int 2013;62:1077–84.

[47] Reglero Ruiz JA, Saiz-Arroyo C, Dumon M, Rodríguez-Perez MA, Gonzalez L. Production, cellular structure and thermal conductivity of microcellular (methyl methacrylate)-(butyl acrylate)-(methyl methacrylate) triblock copolymers. Polym Int 2011;60:146–52.

[48] Chang Y-W, Lee D, Bae S-Y. Preparation of polyethylene-octene elastomer/clay nanocomposite and microcellular foam processed in supercritical carbon dioxide. Polym Int 2006;55:184–9.

[49] Lee K, Chang Y-W, Kim SW. Ethylene-propylene-diene terpolymer/halloysite nanocomposites: Thermal, mechanical properties, and foam processing. J Appl Polym Sci 2014;131.

[50] Yang J, Huang L, Zhang Y, Chen F, Zhong M. Mesoporous silica particles grafted with polystyrene brushes as a nucleation agent for polystyrene supercritical carbon dioxide foaming. J Appl Polym Sci 2013;130:4308–17.

[51] Antonio J, Ruiz R, Cloutet E, Dumon M. Investigation of the Nanocellular Foaming of Polystyrene in Supercritical CO_2 by Adding a CO_2 Philic Perfluorinated Block Copolymer. J Appl Polym Sci 2012;126:38–45.

[52] Zhai W, Leung SN, Wang L, Naguib HE, Park CB. Preparation of Microcellular Poly(ethylene-co-octene) Rubber Foam with Supercritical Carbon Dioxide. J Appl Polym Sci 2010;116:1994-2004.

[53] Ruiz JAR, Viot P, Dumon M. Microcellular foaming of polymethylmethacrylate in a batch supercritical CO_2 process: Effect of microstructure on compression behavior. J Appl Polym Sci 2010;118:320–31.

[54] Ruiz JAR, Marc-Tallon J, Pedros M, Dumon M. Two-step microcellular foaming of amorphous polymers in supercritical CO_2. J Supercrit Fluids 2011;57:87–94.

[55] Corre Y-M, Maazouz A, Duchet J, Reignier J. Batch foaming of chain extended PLA with supercritical CO_2: Influence of the rheological properties and the process parameters on the cellular structure. J Supercrit Fluids 2011;58:177–88.

[56] Goren K, Chen L, Schadler LS, Ozisik R. Influence of nanoparticle surface chemistry and size on supercritical carbon dioxide processed nanocomposite foam morphology. J Supercrit Fluids 2010;51:420–7.

[57] Zhang H, Yan Q, Zheng W, He Z, Yu Z. Tough Graphene - Polymer Microcellular Foams for Electromagnetic Interference Shielding. Appl Mater Interfaces 2011;3:918–24.

[58] Yeh S-K, Liu Y-C, Wu W-Z, Chang K-C, Guo W-J, Wang S-F. Thermoplastic polyurethane/clay nanocomposite foam made by batch foaming. J Cell Plast 2013;49:119–30.

[59] Costeux S, Khan I, Bunker SP, Jeon HK. Experimental study and modeling of nanofoams formation from single phase acrylic copolymers. J Cell Plast 2015;51:197-221.

[60] Pinto J, Reglero-Ruiz JA, Dumon M, Rodriguez-Perez MA. Temperature influence and CO_2 transport in foaming processes of poly(methyl methacrylate)–block copolymer nanocellular and microcellular foams. J Supercrit Fluids 2014;94:198–205.

[61] Guo H, Kumar V. Some thermodynamic and kinetic low-temperature properties of the PC-CO_2 system and morphological characteristics of solid-state PC nanofoams produced with liquid CO_2. Polymer 2015;56:46–56.

[62] Ruckdäschel H. Micro- and nanostructured polymer blends – Processing, properties and foaming behaviour. Univ Bayreuth 2008:242–70.

[63] Costeux S, Bunker SP. Homogenous nanocellular foams from styrenic-acrylic polymer blends. J Mater Res 2013;28:2351–65.

[64] Khorasani MM, Ghaffarian SR, Babaie A, Mohammadi N. Foaming Behavior and Cellular Structure of Microcellular HDPE Nanocomposites Prepared by a High Temperature Process. J Cell Plast 2010;46:173–90.

[65] Ma Z, Zhang G, Yang Q, Shi X, Shi A. Fabrication of microcellular polycarbonate foams with unimodal or bimodal cell-size distributions using supercritical carbon dioxide as a blowing agent. J Cell Plast 2013;50:55–79.

[66] Lee YH. HDPE-Clay Nanocomposite Foams Blown with Supercritical CO_2. J Cell Plast 2005;41:487–502.

[67] Hossieny NJ, Barzegari MR, Nofar M, Mahmood SH, Park CB. Crystallization of hard segment domains with the presence of butane for microcellular thermoplastic polyurethane foams. Polymer 2014;55:651–62.

[68] Ito Y, Yamashita M, Okamoto M. Foam Processing and Cellular Structure of Polycarbonate-Based Nanocomposites. Macromol Mater Eng 2006;291:773–83.

[69] Reglero JA, Viot P, Dumon M. Foaming of amorphous polymers and blends in supercritical CO_2: Solubility versus block copolymers addition. J Cell Plast 2011;47:535–48.

[70] Tran MP, Detrembleur C, Alexandre M, Jerome C, Thomassin JM. The influence of foam morphology of multi-walled carbon nanotubes/poly(methyl methacrylate) nanocomposites on electrical conductivity. Polymer 2013;54:3261–70.

[71] Bao J-B, Liu T, Zhao L, Hu G-H, Miao X, Li X. Oriented foaming of polystyrene with supercritical carbon dioxide for toughening. Polymer 2012;53:5982–93.

[72] Chen L, Schadler LS, Ozisik R. An experimental and theoretical investigation of the compressive properties of multi-walled carbon nanotube/poly(methyl methacrylate) nanocomposite foams. Polymer 2011;52:2899–909.

[73] Miller D, Chatchaisucha P, Kumar V. Microcellular and nanocellular solid-state polyetherimide (PEI) foams using sub-critical carbon dioxide I. Processing and structure. Polymer 2009;50:5576–84.

[74] Weller JE, Kumar V. Solid-state microcellular polycarbonate foams. II. The effect of cell size on tensile properties. Polym Eng Sci 2010;50:2170–2175.

[75] Costeux S, Khan I, Bunker SP, Jeon HK. Experimental study and modeling of nanofoams formation from single phase acrylic copolymers. J Cell Plast 2015;51:197–221.

[76] Goel SK, Beckman EJ. Generation of microcellular polymeric foams using supercritical carbon

dioxide. I: Effect of Pressure and Temperature on Nucleation. Poly Eng Sci 1994;34:1137–47.

[77] Satish K, Eric J, Goel SK, Beckman EJ. Generation of Microcellular Polymeric foams using Supercritical Carbon Dioxide. II: Cell Growth and Skin Formation. Polym Eng Sci 1994;34:1148–56.

[78] Naguib H, Park C, Reichelt N. Fundamental foaming mechanisms governing the volume expansion of extruded polypropylene foams. J Appl Polym Sci 2004;91:2662–8.

[79] Naguib HE, Park CB, Lee PC. Effect of Talc Content on the Volume Expansion Ratio of Extruded PP Foamss. J Celluzlar Plast 2004;39:499–511.

[80] Rizvi A, Tabatabaei A, Barzegari MR, Mahmood SH, Park CB. In situ fibrillation of CO_2-philic polymers: Sustainable route to polymer foams in a continuous process. Polymer 2013;54:4645–52.

[81] Julien J-M, Bénézet J-C, Lafranche E, Quantin J-C, Bergeret A, Lacrampe M-F, Krawczak P. Development of poly(lactic acid) cellular materials: Physical and morphological characterizations. Polymer 2012;53:5885–95.

[82] Zhang C, Zhu B, Lee LJ. Extrusion foaming of polystyrene/carbon particles using carbon dioxide and water as co-blowing agents. Polymer 2011;52:1847–55.

[83] Okolieocha C, Koppl T, Kerling S, Tolle FJ, Fathi A, Mülhaupt R, Altstädt V. Influence of graphene on the cell morphology and mechanical properties of extruded polystyrene foam. J Cell Plast 2015;51:413–26.

[84] Larsen Å, Neldin C. Physical extruder foaming of poly(lactic acid)-processing and foam properties. Polym Eng Sci 2013;53:941–949.

[85] Chaudhary AK, Jayaraman K. Extrusion of linear polypropylene-clay nanocomposite foams. Polym Eng Sci 2011;51:1749–56.

[86] Mihai M, Huneault MA, Favis BD. Rheology and extrusion foaming of chain-branched poly(lactic acid). Polym Eng Sci 2010;50:629–42.

[87] Yeh S-K, Yang J, Chiou N-R, Daniel T, Lee LJ. Introducing water as a coblowing agent in the carbon dioxide extrusion foaming process for polystyrene thermal insulation foams. Polym Eng Sci 2010;50:1577–84.

[88] Spitael P, Macosko CW. Strain hardening in polypropylenes and its role in extrusion foaming. Polym Eng Sci 2004;44:2090–100.

[89] Ayoub A, Rizvi SSH. Reactive Supercritical Fluid Extrusion for Development of Moisture Resistant Starch-Based Foams. J Appl Polym Sci 2011;120:2242–50.

[90] Costeux S, Foether D. Continuous Extrusion of Nanocellular Foam. SPE ANTEC Tech Pap 2015;100:1–6.

[91] Xin ZX, Zhang ZX, Pal K, Kim K-J, Kang DJ, Kim JK, et al. Microcellular Structure of PP/Waste Rubber Powder Blends with Supercritical CO_2 by Foam Extrusion Process. J Cell Plast 2009;45:499–514.

[92] Szegda D, Duangphet S, Song J, Tarverdi K. Extrusion foaming of PHBV. J Cell Plast 2014;50:145–62.

[93] Liu W, Wang X, Li H, Du Z, Zhang C. Study on rheological and extrusion foaming behaviors of chain-extended poly (lactic acid)/clay nanocomposites. J Cell Plast 2013;49:535–54.

[94] Michaeli W, Westermann K, Sitz S. Extrusion of physically foamed rubber profiles. J Cell Plast 2011;47:483–95.

[95] Rizvi GM, Park CB, Guo G. Strategies for Processing Wood Plastic Composites with Chemical Blowing Agents. J Cell Plast 2008;44:125–37.

[96] Tejeda EH. Morphology and Mechanical Properties of Foamed Polyethylene-Polypropylene Blends. J Cell Plast 2005;41:417–35.

[97] Xu Z. Effects of Formulations and Processing Parameters on Foam Morphologies in the Direct Extrusion Foaming of Polypropylene using a Single-screw Extruder. J Cell Plast 2005;41:169–85.

[98] Ranade A, Hiltner A, Baer E, Bland DG. Structure-Property Relationships in Coextruded Foam/Film Microlayers. J Cell Plast 2004;40:497–507.

[99] Kim Y, Park CB, Chen P, Thompson RB. Origins of the failure of classical nucleation theory for nanocellular polymer foams. Soft Matter 2011;7:7351–8.

[100] Jung PU. Development of Innovative Gas- Assisted Foam Injection Molding Technology. 2013.

[101] Oxtoby DW. Nucleation of first-order phase transitions. Acc Chem Res 1998;31:91–7.

[102] Xu X, Cristancho DE, Costeux S, Wang Z-G. Bubble nucleation in polymer–CO_2 mixtures. Soft Matter 2013;9:9675–83.

[103] Park CB, Cheung LK, Song SW. The Effect of Talc on Cell Nucleation in Extrusion Foam Processing of Polypropylene with CO_2 and Isopentane. Cell Polym 1998;17:221–51.

[104] Ibeh CC, Bubacz M. Current Trends in Nanocomposite Foams. J Cell Plast 2008;44:493–515.

[105] Cuppoletti J. Nanocomposites and Polymers with Analytical Methods. 2011.

[106] Keshtkar M, Nofar M, Park CB, Carreau PJ. Extruded PLA/clay nanocomposite foams blown with supercritical CO_2. Polymer 2014;55:4077–90.

[107] Chan E, Leung SN, Khan MO, Naguib HE, Dawson F, Adinkrah V. Novel Thermally Conductive Thermoplastic/Ceramic Composite Foams. Macromol Mater Eng 2012;297:1014–20.

[108] Costa JC, Oliveira M, Machado AV, Lanceros-Méndez S, Botelho G. Effect of antistatic additives on mechanical and electrical properties of polyethylene foams. J Appl Polym Sci 2009;112:1595–600.

[109] Suh KW, Park CP, Maurer MJ, Tusim MH, De Genova R, Broos R, Sophiea DP. Lightweight cellular plastics. Adv Mater 2000;12:1779–89.

[110] Guo Z, Yang J, Wingert MJ, Tomasko DL, Lee LJ, Daniel T. Comparison of Carbon Nanofibers and Activated Carbon on Carbon Dioxide Foaming of Polystyrene. J Cell Plast 2008;44:453–68.

[111] Scherzer D, Hahn K, Alicke G, Turznik G, Dietzen F-J. Foam panel having a reduced thermal conductivity. EP000778309B1, 2002.

[112] Breindel RM, Loh RR, Rynd JP, Delaviz Y, Polasky ME. Thermoplastic Foams and Method of Forming them using Nano-Graphite. US 2011/0064938 A1, 2011.

[113] Gordon-Duffy J. Infrared Attenuated Polymeric Foam Insulation with Flame Retardant Performance. US 2012/0074347 A1, 2012.

[114] Delaviz Y, Breindel RM, Weekly MZ. Extruded Polystyrene Foam containing Propylene

Carbonate, Ethylene Carbonate or Butylene Carbonate as a Process Aids. US 2011/0144221 A1, 2011.

[115] Vo CV, Fox RT. Assessment of hydrofluoropropenes as insulating blowing agents for extruded polystyrene foams. J Cell Plast 2013;49:423–38.

[116] Jacobs C, Dey SK. Inert Gases as Alternative Blowing Agents for Extruded Low-Density Polystyrene Foam. J Cell Plast 1995;31:38–47.

[117] Miller LM, Cisar TE, Breindel RM, Weekley MZ. Process for producing extruded foam products having polystyrene blends with high levels of CO_2 as blowing agent. US 6,268,046 B1, 2001.

[118] Lee K-M, Lee EK, Kim SG, Park CB, Naguib HE. Bi-cellular Foam Structure of Polystyrene from Extrusion Foaming Process. J Cell Plast 2009;45:539–53.

[119] Dondero M, Carella J, Borrajo J. (CO_2 + 2-Propanol) Mixture as a Foaming Agent for Polystyrene: A simple Thermodynamic Model for the High VLE-Phase Diagrams Taking into Account Foam Vitrification. J Appl Polym Sci 2007;104:2663–71.

[120] Kan V, Hubert JJ. Process for producing a thermoplastic foam using water and ether. EP000937741B1, 2004.

[121] Handa YP. Expanded and Extruded Biodegradable and Reduced Emission Foams made with Methyl Formate-based Blowing agent. WO 2008/076755 A1, 2008.

[122] Handa YP, Francis GA, Castner GC, Zafar M. Reduced-VOC and Non-VOC Blowing Agents for making Expanded and Extruded Thermoplastic Foams. US 2013/0011648, 2013.

[123] Hayashi T, Kobayashi O, Fukuzawa J, Fujiwara H. Extruded Styrene Resin Foams and Methods for Producing the same. US 6,696,504 B1, 2004.

[124] Michael LM, Breindel RM, Weekley MZ, Cisar TE, Prince KJ. Extruded Foam Product with 134A and Alcohol Blowing Agent. US 6,350,789 B1, 2002.

[125] Paquet AN, Suh KW. Carbon Black-Containing Bimodal Foam Structures and Process for Making. 5,210,105, 1993.

[126] Mihai M, Huneault MA, Favis BD. Foaming of Polystyrene/Thermoplastic Starch Blends. J Cell Plast 2007;43:215–36.

[127] Zhang C, Zhu B, Li D, Lee LJ. Extruded polystyrene foams with bimodal cell morphology. Polymer 2012;53:2435–42.

[128] Weber H, Grave I De, Röhrl E. Foamed Plastics. Ulmann's Encycl 2012;15:540–70.

[129] Patel B, Delaviz Y, Breindel R, Weekly, Mitchell Z, Loh R, Choudhary, Manoj K. Cell Size Enlargers for Polystyrene Foams. WO 2007/149538 A1, 2006.

[130] Kurte-Jardin M. Method and device for producing thermoplastics foam panels, panel manufactured using same method and device and panel use. EP 2 397 303 A1, 2011.

[131] Jung YC, Sahoo NG, Cho JW. Polymeric nanocomposites of polyurethane block copolymers and functionalized multi-walled carbon nanotubes as crosslinkers. Macromol Rapid Commun 2006;27:126–31.

[132] Yan D-X, Dai K, Xiang Z-D, Li Z-M, Ji X, Zhang W-Q. Electrical conductivity and major mechanical and thermal properties of carbon nanotube-filled polyurethane foams. J Appl Polym Sci 2011;120:3014–9.

[133] Motlagh GH, Hrymak AN, Thompson MR. Improved through-plane electrical conductivity in a carbon-filled thermoplastic via foaming. Polym Eng Sci 2008;48:687–96.

[134] Shi L, Li Z, Xie B, Wang J, Tian C, Yang M. Flame retardancy of different-sized expandable graphite particles for high-density rigid polyurethane foams. Polym Int 2006;871:862–71.

[135] Bian X-C, Tang J-H, Li Z-M, Lu Z-Y, Lu A. Dependence of flame-retardant properties on density of expandable graphite filled rigid polyurethane foam. J Appl Polym Sci 2007;104:3347–55.

[136] Wang LL, Tay BK, See KY, Sun Z, Tan LK, Lua D. Electromagnetic interference shielding effectiveness of carbon-based materials prepared by screen printing. Carbon N Y 2009;47:1905–10.

[137] Thomassin JM, Pagnoulle C, Bednarz L, Huynen I, Jerome R, Detrembleur C. Foams of polycaprolactone/MWNT nanocomposites for efficient EMI reduction. J Mater Chem 2008;18:792–6.

[138] Eswaraiah V, Sankaranarayanan V, Ramaprabhu S. Functionalized Graphene-PVDF Foam Composites for EMI Shielding. Macromol Mater Eng 2011;296:894–8.

[139] Chen X, Wu H, Luo Z, Yang B, Guo S, Yu J. Synergistic effects of expandable graphite with magnesium hydroxide on the flame retardancy and thermal properties of polypropylene. Polym Eng Sci 2007;47:1756–60.

[140] Li Y, Zou J, Zhou S, Chen Y, Zou H, Liang M, Luo W. Effect of expandable graphite particle size on the flame retardant, mechanical, and thermal properties of water-blown semi-rigid polyurethane foam. J Appl Polym Sci 2014;131:39885.

[141] Meng X-Y, Ye L, Zhang X-G, Tang P-M, Tang J-H, Ji X, Li Z-M. Effects of expandable graphite and ammonium polyphosphate on the flame-retardant and mechanical properties of rigid polyurethane foams. J Appl Polym Sci 2009;114:853–63.

[142] Wang C-Q, Ge F-Y, Sun J, Cai Z-S. Effects of expandable graphite and dimethyl methylphosphonate on mechanical, thermal, and flame-retardant properties of flexible polyurethane foams. J Appl Polym Sci 2013;130:916–26.

[143] Chen L, Blizard K, Straff R, Wang X. Effect of Filler Size on Cell Nucleation During Foaming Process. J Cell Plast 2002;38:139–48.

[144] Ramesh NS, Lee ST. Do nanoparticles really assist in nucleation of fine cells in polyolefin foams? Cell Polym 2005;24:269–77.

[145] Fletcher NH. Size Effect in Heterogeneous Nucleation. J Chem Phys 1958;29:572–6.

[146] Chen L, Ozisik R, Schadler LS. The influence of carbon nanotube aspect ratio on the foam morphology of MWNT/PMMA nanocomposite foams. Polymer 2010;51:2368–75.

[147] Leung SN, Park CB, Li H. Effects of Nucleating Agents' Shapes and Interfacial Properties on Cell Nucleation. J Cell Plast 2010;46:441–60.

[148] McClurg RB. Design criteria for ideal foam nucleating agents. Chem Eng Sci 2004;59:5779–86.

[149] Zhang X-M, Li H, Chen W-X, Feng L-F. Rheological properties and morphological evolutions of polypropylene/ethylene-butene copolymer blends. Polym Eng Sci 2012;52:1740–8.

[150] Parameswaranpillai J, Thomas S, Grohens Y. Polymer Blends: State of the Art, New

Challenges, and Opportunities. Charact. Polym. Blends Miscibility, Morphol. interfaces, 2015, p. 1–5.

[151] Sadiku-Agboola O, Sadiku ER, Adegbola AT, Biotidara OF. Rheological Properties of Polymers: Structure and Morphology of Molten Polymer Blends. Mater Sci Appl 2011;2011:30–41.

[152] Ruckdäschel H, Rausch J, Sandler JKW, Altstaedt V. Foaming of Miscible and Immiscible Polymer Blends. Symp. FF - Process. Prop. Relations Compos. Mater., vol. 997, 2011.

[153] Harrats C, Thomas A, Groeninckx G. Micro- and Nanostructured Multiphase Polymer Blend Systems. Phase Morphology and Interfaces. 2006.

[154] Pinto J, Rodriguez-perez MA, De Saja J, Dumon M, Garcia R, Dietz C. Relationship between the Nano-structured morphology of PMMA/MAM Blends and the Nanocellulat structure of FOams produced from these materials. Soc. Plast. Eng. Foam. 2011 Conf. Iselin, NJ, 2011.

[155] Gutmann P. Organische Flüssigkeiten als Treibmittel für Blendsysteme aus amorphen Thermoplasten. 2011.

[156] Han X, Shen J, Huang H, Tomasko DL, Lee LJ. CO_2 foaming based on polystyrene/poly(methyl methacrylate) blend and nanoclay. Polym Eng Sci 2007;47:103–11.

[157] Sorrentino L, Cafiero L, Iannace S. Control of Micro- and Nanocellular Structures in CO_2 Foamed PES/PEN Blends. Polym Eng Sci 2015:1281–9.

[158] Rachtanapun P, Selke SEM, Matuana LM. Relationship between cell morphology and impact strength of microcellular foamed high-density polyethylene/polypropylene blends. Polym Eng Sci 2004;44:1551–60.

[159] Wang X, Liu W, Li H, Du Z, Zhang C. Role of maleic- anhydride-grafted- polypropylene in supercritical CO_2 foaming of poly (lactic acid) and its effect on cellular morphology. J Cell Plast 2016;52:37–56.

[160] Ruiz JAR, Pedros M, Tallon J-M, Dumon M. Micro and nano cellular amorphous polymers (PMMA, PS) in supercritical CO_2 assisted by nanostructured CO_2-philic block copolymers – One step foaming process. J Supercrit Fluids 2011;58:168–76.

[161] Ozone Secretariat. Handbook for the Montreal Protocol on Substances that Deplete the Ozone Layer. 1991.

[162] Leung SNS. Mechanism of Cell Nucleation, Growth and Coarsening in Plastic Foamsing: Theory, Simulation and Experiment. 2009.

[163] Nalawade SP, Picchioni F, Janssen LPBM. Supercritical carbon dioxide as a green solvent for processing polymer melts: Processing aspects and applications. Prog Polym Sci 2006;31:19–43.

[164] Ahmadzai A, Behravesh AH, Sarabi MT, Shahi P. Visualization of foaming phenomena in thermoplastic injection molding process. J Cell Plast 2014;50:279–300.

[165] Sauceau M, Fages J, Common A, Nikitine C, Rodier E. New challenges in polymer foaming: A review of extrusion processes assisted by supercritical carbon dioxide. Prog Polym Sci 2011;36:749–66.

[166] Garcia-Leiner M, Lesser AJ. CO_2-assisted polymer processing: A new alternative for intractable polymers. J Appl Polym Sci 2004;93:1501–11.

[167] Xu Z-M, Jiang X-L, Liu T, Hu G-H, Zhao L, Zhu Z-N, Yuan W-K. Foaming of polypropylene

with supercritical carbon dioxide. J Supercrit Fluids 2007;41:299–310.

[168] Ding J, Ma W, Song F, Zhong Q. Foaming of polypropylene with supercritical carbon dioxide: An experimental and theoretical study on a new process. J Appl Polym Sci 2013;130:2877–85.

[169] Yang Q. Janus particles: Fabrication, design and distribution in block copolymers. University of Groningen, 2016.

[170] Savage PE, Gopalan S, Mizan TI, Martino CJ, Brock EE. Reactions at Supercritical Conditions : Applications and Fundamentals. AIChE J 1995;41:1723–78.

[171] Bao D, Liao X, He G, Huang E, Yang Q, Li G. Effects of enhanced compatibility by transesterification on the cell morphology of poly(lactic acid)/ polycarbonate blends using supercritical carbon dioxide. J Cell Plast 2015;51:349–72.

[172] Muth O, Hirth T, Vogel H. Investigation of sorption and diffusion of supercritical carbon dioxide into poly(vinyl chloride). J Supercrit Fluids 2001;19:299–306.

[173] Hu D, Chen J, Sun S, Liu T, Zhao L. Solubility and Diffusivity of CO_2 in Isotactic Polypropylene/Nanomontmorillonite Composites in Melt and Solid States. Ind Eng Chem Res 2014;53:2673–83.

[174] Mohebbi A, Mighri F, Ajji A, Rodrigue D. Current Issues and Challenges in Polypropylene Foaming : A Review. Cell Polym 2015;34:299–338.

[175] Nofar M, Majithiya K, Kuboki T, Park CB. The foamability of low-melt-strength linear polypropylene with nanoclay and coupling agent. J Cell Plast 2012;48:271–87.

[176] Liao R, Yu W, Zhou C. Rheological control in foaming polymeric materials: I. Amorphous polymers. Polymer 2010;51:568–80.

[177] Liao R, Yu W, Zhou C. Rheological control in foaming polymeric materials: II. Semi-crystalline polymers. Polymer 2010;51:6334–45.

[178] Huang H-X, Wang J-K. Improving polypropylene microcellular foaming through blending and the addition of nano-calcium carbonate. J Appl Polym Sci 2007;106:505–13.

[179] Huang H-X, Wang J-K, Sun X-H. Improving of Cell Structure of Microcellular Foams Based on Polypropylene/High-density Polyethylene Blends. J Cell Plast 2008;44:69–85.

[180] Stefan T, Friedrich C. Van Gurp-Palmen-plot: A way to characterize polydispersity of linear polymers. Rheol Acta 2001;40:322–8.

[181] Dalsin SJ. Bottlebrush Polymers: Synthesis, Rheology, and Self-Assembly. 2015.

[182] Miao Hu MS. Rheological responses of polymer materials with different architectures. 2011.

[183] Hao X. Rheological and thermo-mechanical properties of PLA-based miscible blends and composites. 2016.

[184] Pan Y, Schubert DW, Ryu JE, Wujick E, Liu C, Shen C, et al. Dynamic oscillatory rheological properties of polystyrene/poly(methyl methacrylate) blends and their composites in the presence of carbon black. Eng Sci 2018;1:86–94.

[185] Kashi S. Graphene Nanoplatelet-based Nanocomposites : Electromagnetic Interference Shielding Properties Doctor of Philosophy. 2017.

[186] Gotsis AD, Zeevenhoven BLF, Hogt AH. The effect of long chain branching on the processability of polypropylene in thermoforming. Polym Eng Sci 2004;44:973–82.

[187] Nam GJ, Yoo JH, Lee JW. Effect of long-chain branches of polypropylene on rheological

properties and foam-extrusion performances. J Appl Polym Sci 2005;96:1793–800.

[188] Xu H, Fang H, Bai J, Zhang Y, Wang Z. Preparation and Characterization of High-Melt-Strength Polylactide with Long-Chain Branched Structure through γ-Radiation-Induced Chemical Reactions. Ind Eng Chem Res 2014;53:1150–9.

[189] Ono K, Ogita H, Okamoto K, Yamaguchi M. Processability and mechanical properties for binary blends of PP and LLDPE produced by metallocene catalyst. J Appl Polym Sci 2009;113:3368–75.

[190] Lim L-T, Auras R, Rubino M. Processing technologies for poly(lactic acid). Prog Polym Sci 2008;33:820–52.

[191] Laguna-gutierrez E, Lopez-gil A, Saiz-arroyo C, Hooghten R Van, Moldenaers P, Rodriguez-perez MA. Extensional rheology, cellular structure, mechanical behavior relationships in HMS PP / montmorillonite foams with similar densities. J Polym Res 2016;23:1–16.

[192] Lee R. Know Your Options for Foaming Sheet. Plast Technol 2015. www.ptonline.com.

[193] Baird DG. The role of extensional rheology in polymer processing. Korea-Australia Rheol J 1999;11:305–11.

[194] Lang M. Evaluierung des Schäumverhaltens eines mittels Kern-Schale-Teilchen zähmodifizierten, rezyklierbaren amorphen Polymers. Universität Bayreuth, 2014.

[195] Bernnat A. Polymer melt rheology and the rheotens test. 2001.

[196] Swartjes F.H.M. A method for the evaluation of 3D viscoelastic flows A method for the evaluation of 3D viscoelastic flows. 1998.

[197] Xu X, Park CB, Xu D, Pop-Iliev R. Effects of die geometry on cell nucleation of PS foams blown with CO_2. Polym Eng Sci 2003;43:1378–90.

[198] Kumar V, Weller J. Production of Microcellular Polycarbonate Using Carbon Dioxide for Bubble Nucleation. J Eng Ind 1994;116:413–20.

[199] Pinto J, Solorzano E, Rodriguez-Perez MA, De Saja J. Characterization of the cellular structure based on user-interactive image analysis procedures. J Cell Plast 2013;49:555–75.

[200] Liu P, Liu D, Zou H, Fan P, Xu W. Structure and properties of closed-cell foam prepared from irradiation crosslinked silicone rubber. J Appl Polym Sci 2009;113:3590–5.

[201] Saiz-Arroyo C, Rodríguez-Pérez MA, Tirado J, López-Gil A, De Saja J. Structure-property relationships of medium-density polypropylene foams. Polym Int 2013;62:1324–33.

[202] Ngo TT Van, Duchet-Rumeau J, Whittaker AK, Gerard J-F. Processing of nanocomposite foams in supercritical carbon dioxide. Part I: Effect of surfactant. Polymer 2010;51:3436–44.

[203] Chiu F-C, Lai S-M, Wong C-M, Hui Chang C. Properties of calcium carbonate filled and unfilled polystyrene foams prepared using supercritical carbon dioxide. J Appl Polym Sci 2006;102:2276–84.

[204] Spitael P, Macosko CW, McClurg RB. Block Copolymer Micelles for Nucleation of Microcellular Thermoplastic Foams. Macromolecules 2004;37:6874–82.

[205] Shen J. Nanoscaled Reinforcement of Polystyrene Foams using Carbon Nanofibers. J Cell Plast 2006;42:105–26.

[206] Gendron R, Moulinie P. Foaming Poly(methyl methacrylate) with an Equilibrium Mixture of Carbon Dioxide and Isopropanol. J Cell Plast 2004;40:111–30.

[207] Hummers WS, Offeman RE. Preparation of Graphitic Oxide. J Am Chem Soc 1958;80:1339.

[208] Johannes F. Bindemittelfreie Graphen-Dispersionen aus Graphit und Graphitoxid für Katalyse und Polymer-Nanokomposite. 2013.

[209] Abraham J, Sharika T, George SC, Thomas S. Rheological Percolation in Thermoplastic Polymer Nanocomposites. Rheol Open Access 2017;1:1–15.

[210] Pötschke P, Abdel-Goad M, Pegel S, Jehnichen D, Mark JE, Zhou D. Comparisons Among Electrical and Rheological Properties of Melt-Mixed Composites Containing Various Carbon Nanostructures. J Macromol Sci Part A 2009:12–9.

[211] Liu H, Han C, Dong L. Study of the Biodegradable Poly(e-caprolactone)/Clay Nanocomposite Foams. J Appl Polym Sci 2009;115.

[212] Ariff ZM, Zakaria Z, Tay LH, Lee SY. Effect of Foaming Temperature and Rubber Grades on Properties of Natural Rubber Foams. J Appl Polym Sci 2007;47:2531–8.

[213] Judith Martín-de L, Bernardo V, Rodríguez-pérez MÁ. Low Density Nanocellular Polymers Based on PMMA Produced by Gas Dissolution Foaming : Fabrication and Cellular Structure Characterization. Polymers 2016;8:1–16.

[214] Wong A, Mark LH, Hasan MM, Park CB. The synergy of supercritical CO_2 and supercritical N2 in foaming of polystyrene for cell nucleation. J Supercrit Fluids 2014;90:35–43.

[215] Ruckdäschel H, Rausch J, Sandler JKW, Altstädt V, Schmalz H. Correlation of the Melt Rheological Properties with the Foaming Behavior of Immiscible Blends of Poly (2,6-dimethyl-1,4-phenylene ether) and Poly(styrene-co-acrylonitrile). Polym Eng Sci 2008;48:2111-125.

8 Publications and conference contributions

8.1 Publications

C. Okolieocha, D. Raps K. Subramaniam, V. Altstädt
Microcellular to Nanocellular Polymer foams: Progress (2004-2015) and future directions- A Review.
European Polymer Journal 2015, 73, 500-519.

C. Okolieocha, F. Beckert, M. Herling, J. Breu, R. Mülhaupt, V. Altstädt
Preparation of microcellular low-density PMMA nanocomposite Influence of different fillers on the mechanical, rheological and cell.
Composite Science and Technology, 2015, 118, 108-116.

H. Yin, B. Dittrich, M. Farooq, S. Kerling, K. A. Wartig, D. Hofmann, C. Huth, **C. Okolieocha**, V. Altstädt, A. Schönhals, B. Schartel
Carbon-based Nanofillers/Poly(butylene terephthalate): Thermal, Electrical and Rheological properties.
Journal of Polymer Research, 2015, 22, 1-13.

C. Okolieocha, T. Köppl, S. Kerling, F. J. Tölle, A. Fathi, R. Mülhaupt, V. Altstädt
Influence of graphene on the cell morphology and mechanical properties of extruded polystyrene foams.
Journal of Cellular Plastics, 2015, 51, 413-426.

8.2 Conference contributions

C. Okolieocha, T. Köppl, S. Kerling, F. J. Tölle, R. Mülhaupt, V. Altstädt:
Potential of Carbon-Based Nanoparticles (CNT, CB, Graphene) to increase the Nucleation Density of Extruded Polystyrene Foam, 29th Annual Meeting of the Polymer Processing Society (PPS29), Conference Proceedings, Nürnberg, Deutschland (2013).

C. Okolieocha, T. Köppl, S. Kerling, V. Altstädt:
Influence of Carbon-Based Nanoparticles on the Thermal Conductivity of Extruded Polystyrene Foams, Blowing Agents and Foaming Processes 2013, Conference Proceedings, iSmithers Rapra Publishing, ISBN 978-1-909030-42-8, Mainz, Deutschland (2013).

C. Okolieocha, C. Keilholz, T. Köppl, S. Kerling, F. J. Tölle, R. Mülhaupt, V. Altstädt:
Graphene as a multi- functional nanofiller for the reduction of thermal conductivity of extruded polystyrene foam (XPS), 11th International Conference on Foam Materials & Technology (FOAMS 2013), Conference Proceedings, Seattle/WA, USA (2013).

V. Altstädt, **C. Okolieocha**, T. Köppl, F. J. Tölle, R. Mülhaupt:
Graphene for Polymer Foams, Polymer Foam 2013 Conference Proceedings, Hamburg, Deutschland.

9 Curriculum vitae

Personal Data

Name:	Chimezie Okolieocha
Date/Place of birth:	17.01.1985, Lagos
Civil stand:	Married with a child
Address:	Burggartenstrasse 28, CH-4103 Bottmingen Basel-Landschaft, Switzerland
Nationality:	Nigerian/German

Academic qualifications

1990 – 1995	Command Children School Mile II, Lagos
1996 – 2002	Federal Government College Odogbolu, Ogun state
2002 – 2007	Federal University of Technology Owerri (Bachelor: Polymer & Textile Engineering)
2008 – 2011	Martin-Luther-Universität Halle-Wittenberg (Master: Applied Polymer Science)

Promotion

2019	Title: Microcellular low-density nanocomposite foams nucleated by carbon-based nanofillers -processing, properties and foaming behaviour

Work experience

2012 – 2015	Scientific staff member, Lehrstuhl für Polymere Werkstoffe, Universität Bayreuth
2016 – 2017	Autokabel Management GmbH Hausen im Wiesental, Deutschland
Since 2017	Endress + Hauser Flowtec AG Reinach, Basel, Schweiz